

ABSTRACT

Title of Document: MODELING L-BAND MICROWAVE
EMISSION FROM SOIL-VEGETATION
SYSTEM

Alicia T. Joseph, PhD, 2011

Directed By: Professor, Eric Kasischke, Geography

During a field campaign covering the 2002 corn growing season, a dual polarized tower mounted L-band (1.4 GHz) radiometer (LRAD) provided brightness temperature (T_B) measurements at preset intervals, incidence and azimuth angles. These radiometer measurements were supported by an extensive characterization of land surface variables including soil moisture, soil temperature, vegetation biomass, and surface roughness. From May 22, 2002 to August 30, 2002 a range of vegetation water content (W) of 0.0 to 4.3 kg m⁻², ten days of radiometer and ground measurements were available. Using this data set, the effects of corn vegetation on surface emissions are investigated by means of a semi-empirical radiative transfer model. The impact of roughness on the surface emission is quantified using T_B measurements over bare soil conditions. Subsequently, the estimated roughness parameters, ground measurements and horizontally (H)-polarized T_B are employed to invert the H-polarized transmissivity (γ_h) for the monitored corn growing season.

MODELING L-BAND MICROWAVE EMISSION FROM SOIL-VEGETATION
SYSTEM

By

Alicia T. Joseph

Dissertation submitted to the Faculty of the Graduate School of the
University of Maryland, College Park, in partial fulfilment
of the requirements for the degree of
Doctor of Philosophy
2011

Advisory Committee:
Professor Eric Kasischke, Chair
Dr. Shunlin Liang
Dr. Guoqing Sun
Dr. Peter Hildebrand
Dr. Kaye Brubaker

© Copyright by
Alicia T. Joseph
2011

Foreword

A portion of the material presented in this dissertation (Chapter 3) has appeared in a published journal article with multiple co-authors. The Dissertation Committee has reviewed Ms. Joseph's role in this research and has determined that she made substantial contributions to this jointly-authored research.

Dedication

I would like to dedicate this dissertation to several groups of people who have supported and encouraged me through various stages in this journey. The completion of this dissertation is dedicated to Avis Phipps, Albert Joseph, Susan Charles and Lillian Bullen. Thanks to Angela Joseph-Phipps, Philson Lewis, Charles Phipps, Laurel Charles and Winston Charles for their support throughout my life. Thanks to the Hille family who have taken me in as their own. Karl F. Hille, thank you for your love and encouragement.

Acknowledgements

I would like to acknowledge my dissertation committee for their dedication and support; they have served as wonderful role models and have encouraged me on this long journey. I would especially like to thank Dr. Thomas Jackson and Dr. Ruth DeFries who served on my committee, but were unable to serve on my dissertation committee due to schedule conflicts and relocation. Additionally, I would like to thank my colleagues and mentors, Peggy O'Neill, Bhaskar Choudhury and Christa Peters-Lidard at NASA Goddard space Flight Center for their continuous support, advice and encouragement. I also must acknowledge my colleagues at the Tor Vergata University in Rome (Dr. Paolo Ferrazzoli) and ITC in the Netherland (Dr. Rogier van der Velde) for sharing their expertise and use of their vegetation scattering model and data sets. I would also like to thank the staff and faculty at the Department of Geography at the University of Maryland for the supportive environment that was provided through this process.

My parents and grandparents instilled in me the importance of education and gently guided me along that path. My mom was my teacher during my early years of elementary school and continued to serve as a role model throughout my academic career. My stepfather made going to school fun even on the days when I had difficulty waking up early to get to class. To the Hille family, in the several years that I have known you, your friendship and support has been invaluable. I would especially like to thank Karl F. Hille, Herb Hille and Victoria Boucher-Hille for your unconditional love and patience. To Mother Retie Bynoe, thank you for your uplifting words of encouragement

and guidance and for always reminding me to put God first. To my friends and family, thank you for supporting and “putting up” with me throughout this entire journey.

Table of Contents

Foreword	ii
Dedication	iii
Acknowledgements	iv
Table of Contents	vi
List of symbols	viii
List of abbreviations	xiii
1 Introduction	1
1.1 Background.....	1
1.2 Research goals and objectives	4
1.3 Research questions	5
2 Background.....	7
2.1 Emission from soil	7
2.2 Vegetation effects on emission	8
2.3 Semi-empirical emission modeling	11
2.4 Physically based emission modeling	13
2.5 Tor Vergata model	17
2.6 Electromagnetic representation of the canopy	17
2.7 Electromagnetic representation of the soil	20
2.8 Integrating the effects of individual scatterers	22
2.9 Backscatter and emissivity calculation	23
2.10 Study sites	25
2.11 1981 BARC experiments	26
2.12 2002 OPE ³ campaign	31
3 Angular dependence of the soil roughness effect on microwave emission.....	39
3.1 Introduction	40
3.2 Theoretical background	43
3.3 The OPE ³ experiment	48
3.4 Results	58
3.5 Concluding remarks.....	70
4 H polarized L-band microwave emission during the corn growth cycle.	73
4.1 Introduction	73
4.2 From incidental to continuous measurements	76
4.3 τ - ω model application and parameter estimations	84
4.4 Results	89
4.5 Discussion	106
4.6 Conclusions	109
5 Modeling L-band emission during a corn growing season	113
5.1 Introduction	113
5.2 Parameterization of the Tor Vergata model	115
5.3 Dielectric mixing models	120
5.4 Impact of mixing model.....	129
5.5 Impact of corn on L-band emission.....	133
5.6 Summary and conclusions	138
6 Summary and conclusions	141
6.1 Research questions and outline	141
6.2 Angular dependence of the soil roughness effects on microwave emission.....	142
6.3 Horizontal polarized L-band microwave emission.....	143
6.4 Model investigation of morphological effects on L-band emission	144

6.5	Future work.....	145
	References.....	148

List of symbols

Greek

Symbol	Name	Units
α	Albedo	-
β	Bowen ratio	-
γ	Attenuation by the canopy	-
γ_d	Density of dry soil	kg m^{-3}
γ_p	Psychrometric constant	kPa K^{-1}
Δ	Slope of the saturated vapor pressure curve	kPa K^{-1}
ε	Electric permittivity	F m^{-1}
ε_0	Electric permittivity of free space	F m^{-1}
ε_r	Relative permittivity or dielectric constant	-
κ_{dry}	Thermal conductivity under dry soil moisture conditions	$\text{W m}^{-1} \text{K}^{-1}$
κ_e	Extinction coefficient	m^{-1}
κ_h	Thermal conductivity	$\text{W m}^{-1} \text{K}^{-1}$
κ_{h_2o}	Thermal conductivity of water	$\text{W m}^{-1} \text{K}^{-1}$
κ_{ice}	Thermal conductivity of ice	$\text{W m}^{-1} \text{K}^{-1}$
κ_o	Thermal conductivity of soil particles other than quartz	$\text{W m}^{-1} \text{K}^{-1}$
κ_{qtz}	Thermal conductivity of quartz	$\text{W m}^{-1} \text{K}^{-1}$
κ_{sat}	Thermal conductivity under saturated soil moisture conditions	$\text{W m}^{-1} \text{K}^{-1}$
λ	Wavelength	m
λ_v	heat of vaporization	J kg^{-1}
μ	Magnetic permeability	N A^{-2}
μ_0	Magnetic permeability of free space	N A^{-2}
θ	Soil moisture content	$\text{m}^3 \text{m}^{-3}$
θ_c	Critical soil moisture content below which transpiration is reduced due to soil moisture stress	$\text{m}^3 \text{m}^{-3}$
$\theta_{(i)}$	Moisture content in the i^{th} soil layer	$\text{m}^3 \text{m}^{-3}$
θ_i	Incidence angle	degrees
θ_{ice}	Frozen soil moisture content	$\text{m}^3 \text{m}^{-3}$
θ_{lig}	Liquid soil moisture content	$\text{m}^3 \text{m}^{-3}$
θ_s	Saturated soil moisture content	$\text{m}^3 \text{m}^{-3}$
θ_w	Soil moisture content at wilting point below which soil plants cannot take up soil water	$\text{m}^3 \text{m}^{-3}$

ρ	correlation	-
ρ_{air}	Air density	kg m ⁻³
σ	scattering cross section of a target	m ² m ⁻²
σ_v	Scattering cross section of the vegetation	m ⁻¹
σ_s	Stefan-Boltzmann constant	W m ⁻² K ⁻⁴
σ^o	backscattering coefficient	m ² m ⁻² or dB
σ_{surf}^o	Surface scattering	m ² m ⁻² or dB
σ_s^o	Soil surface scattering contribution	m ² m ⁻² or dB
$\sigma_{s\leftrightarrow v}^o$	Scattering contribution from the soil-vegetation pathways	m ² m ⁻² or dB
σ_v^o	Vegetation scattering contribution	m ² m ⁻² or dB
σ_b^2	Mean squared difference between two samples caused by an inherent bias due to differences in the climatology of the two samples	-
σ_s^2	Mean squared difference between two samples caused by difference in the spatial resolution of the two samples	-
σ_t^2	Mean total squared difference between two samples	-
σ_u^2	Mean squared difference between two samples caused by uncertainties in the two samples	-
ψ	Soil water potential	m
ψ_s	Saturated soil water potential	m

Roman

Symbol	Name	Units
a_0	Soil texture dependent parameters for converting the dielectric constant measured by an impedance probe (Delta-T theta probe) into soil moisture	-
a_1		-
A	Empirical crop parameter for the cloud model	-
A_0	Area illuminated by a radar beam	m^2
A_e	Effective area of the antenna	m^2
b_c	Empirical parameter of the Campbell soil hydraulic model	-
b_{clim}	Systematic bias in soil moisture data sets due to a difference in climatology between the two samples	$m^3 m^{-3}$
B	Empirical crop parameter for the cloud model	-
c_p	Specific heat capacity of moist air	$kJ kg^{-1} K^{-1}$
C	Differential water capacity	m^{-1}
C_h	Surface exchange coefficient for heat	-
C_q	Surface exchange coefficient for moisture	-
C_s	Soil thermal heat capacity	$J m^{-3} K^{-1}$
C_{soil}	Thermal heat capacity of air	$J m^{-3} K^{-1}$
C_w	Thermal heat capacity of water	$J m^{-3} K^{-1}$
cmc	Moisture content on the leaves of the canopy	$kg m^{-2}$
cmc_{max}	Maximum moisture content on the leaves of the canopy	$kg m^{-2}$
D	Soil water diffusivity	$m^2 s^{-1}$
D_b	Soil moisture deficit in the soil column	$m^3 m^{-3}$
D_s	Saturated soil water diffusivity	$m^2 s^{-1}$
e	Vapor pressure	kPa
e_s	Surface emissivity	-
E_c	Evaporation of rain intercepted by vegetation	$W m^{-2}$
E_{dir}	Soil evaporation	$W m^{-2}$
E_t	Evaporation through the stomata of vegetation	$W m^{-2}$
E_p	Potential evaporation	$W m^{-2}$
\mathbf{E}	Electric field vector	$V m^{-1}$
f_{air}	Volume fraction air within the soil matrix	-
f_c	Fractional vegetation cover	-
f_{soil}	Volume fraction soil within the soil matrix	-
f_w	Volume fraction water within the soil matrix	-
f_{pq}	Kirchhoff field coefficients utilized with the IEM model	-
F_{pq}	Complementary field coefficients utilized with the IEM model	-

fx	Empirical parameter affecting the soil evaporation reduction under soil moisture stress conditions	-
f_{root}	Fraction of the root zone represented by the i^{th} layer	-
G_0	Soil heat flux at the surface	W m^{-2}
G_{10}	Soil heat flux at a 0.10 m soil depth	W m^{-2}
G_t	Power gain of the transmitting antenna	-
h	Canopy height	m
h_s	Empirical parameter describing the optimal transpiration conditions with respect to the air humidity	-
H	Sensible heat flux	W m^{-2}
\mathbf{H}	Magnetic field vector	A m^{-1}
I_{max}	Maximum infiltration capacity	m s^{-1}
k	Wave number	m^{-1}
K	Hydraulic conductivity	m s^{-1}
K_e	Kersten number	-
K_{ref}	Empirical parameter for Noah runoff simulations	m s^{-1}
K_s	Saturated hydraulic conductivity	m s^{-1}
kdt	Empirical parameter for Noah runoff simulations	-
kdt_{ref}	Empirical parameter for Noah runoff simulations	-
l	Correlation length	m
L^{\downarrow}	Longwave incoming radiation	W m^{-2}
LAI	Leaf Area Index	$\text{m}^2 \text{m}^{-2}$
λE	Latent heat flux	W m^{-2}
n	Number of samples	#
n_{root}	Number of root zone layer within the Noah model	#
P	Rain intensity	m s^{-1}
P_a	Air pressure	kPa
P_t	Power transmitted by an antenna	W
P_r	Power received by an antenna	W
q	Actual specific humidity	kg kg^{-1}
q_s	Saturated specific humidity	kg kg^{-1}
qtz	Volume fraction quartz	-
R	Distance between the target and antenna	m
$R_{c,\text{min}}$	Minimum stomatal resistance	s m^{-1}
$R_{c,\text{hum}}$	Factor increasing the stomatal resistance in case of a sub-optimal air humidity for transpiration	-
$R_{c,\text{rad}}$	Factor increasing the stomatal resistance in	-

	case of a sub-optimal radiative conditions for transpiration	
$R_{c,soil}$	Factor increasing the stomatal resistance in case of soil moisture stress on transpiration	-
$R_{c,temp}$	Factor increasing the stomatal resistance in case of a sub-optimal air temperature for transpiration	-
R_{gl}	Parameter characterized the light-use efficiency of a canopy	$W m^{-2}$
R_n	Net radiation	$W m^{-2}$
R_p	p -polarized Fresnel reflectivity	-
R_{surf}	Surface runoff	$m s^{-1}$
s	Root mean square of surface height variations	m
S	Water sinks and source to the soil column	$m s^{-1}$
S^\downarrow	Shortwave incoming radiation	$W m^{-2}$
t	Time step	s
T_{air}	Air temperature	K
T_{opt}	Optimum temperature for transpiration	K
$T_{p air}$	Potential air temperature	K
$T_{s(i)}$	Soil temperature in the i^{th} soil layer	K
T_{skin}	Skin temperature	K
u	Wind speed	$m s^{-1}$
V_1	vegetation descriptor 1 used within the cloud model	-
V_2	vegetation descriptor 2 used within the cloud model	-
W	Vegetation water content	$kg m^{-2}$
x	Horizontal displacement	m
z	Surface height	m
z_{0m}	Aerodynamic roughness length for momentum transport	m
z_{0h}	Aerodynamic roughness length for heat transport	m

List of abbreviations

ACF	Autocorrelation length Function
ACM	Atmospheric Circulation Models
ALSIS	Atmospheric and Land-Surface Interaction Scheme
ASCAT	Advanced Scatterometer
ARS	Agricultural Research Service
ASAR	Advanced Synthetic Aperture Radar
BARC	Beltsville Agriculture Research Center
BREB	Bowen Ratio Energy Balance
BST	Beijing Standard Time
CAMP	CEOP Asia-Australia Monsoon Project
CAS	Chinese Academy of Sciences
CDF	Cumulative Distribution Function
CEOP	Coordinated Enhanced Observing Period
EC	Eddy Correlation
ENVISAT	Environmental Satellite
ERS	European Remote Sensing satellite
ESA	European Space Agency
GAME	GEWEX Asian Monsoon Experiment
GEWEX	Global Energy and Water cycle Experiment
GM	Global Monitoring mode
GMES	Global Monitoring for Environment and Security
GSFC	Goddard Space Flight Center
GWU	George Washington University
ITP	Institute for Tibetan Plateau Research
JAXA	Japan Aerospace Exploration Agency
KNMI	Koninklijk Nederlands Meteorologisch Instituut
LSM	Land Surface Model
LAI	Leaf Area Index
MM5	Meso-scale Model version 5
MOST	Ministry of Science and Technology
NASA	National Aeronautics and Space Administration
NCAR	National Center for Atmospheric Research
NCEP	National Centers for Environmental Prediction
NDVI	Normalized Difference Vegetation Index
OPE ³	Optimizing Production Inputs for Economic and Environmental Enhancements
OSU	Oregon State University
PALSAR	Phased Array type L-band SAR
PDF	Probability Density Function
PSU	Penn State University
PTF	PedoTransfer Function
RMSD	Root Mean Squared Differences
SAR	Synthetic Aperture Radar
SHF	Soil Hydraulic Function
SHM	Soil Hydraulic Model
SHP	Soil Hydraulic Parameters
SMAP	Soil Moisture Active/Passive mission
SMOS	Soil Moisture and Ocean Salinity mission
SSD	Sum of Squared Differences

STL	Soil Thermal Layer
STP	Soil Thermal Properties
SWB	Simple Water Balance model
TM	Thematic Mapper
USA	United States of America
USDA	United States Department of Agriculture
VIC	Variable Infiltration Capacity model
WS	Wide Swath mode

1 Introduction

1.1 Background

One of the challenges for policy makers is to protect society from the socio-economic consequences of environmental disasters resulting from floods and droughts, where being able to predict and respond quickly to potential threats is an important management tool. Floods and droughts are both directly a result of extreme weather conditions. While floods are local phenomena and typically affect small areas for relatively short periods, they often have significant and long lasting impacts on people living in the affected areas. Droughts are regional phenomena affecting large areas for relatively long periods. While farmers and hydro-electrical power plants are directly affected by droughts, the increase in the prices of food and electricity affect a broader segment of society.

Numerical Weather Prediction (NWP) models operated by national weather services are used to forecast the extreme weather conditions that result in droughts and floods. However, the reliability of these models is strongly influenced by the uncertainty in the soil moisture conditions. Various investigations have shown through a proper soil moisture initialization, the timing and severity of extreme events, such as floods (United States 1993, Bosilovich and Sun 1999) and extreme droughts (Europe 2003, Ferranti and Viterbo 2006) can be predicted more accurately, which would give governmental agencies more time to respond to potential treats.

Observations acquired by spaceborne passive microwave instruments have shown sensitivity to variations in soil moisture (Bindlish et al. 2003, Wen et al. 2003 and Owe et al. 2001). Based on this characteristic of passive microwave instruments, satellite missions have been and are being proposed to space agencies for monitoring soil

Introduction

moisture on a global scale [e.g. Soil Moisture and Ocean Salinity (SMOS) mission, Aquarius and Soil Moisture Active Passive (SMAP)]. Utilization of accurate soil moisture products derived from these satellite observations within hydrological and weather forecasting models would greatly improve predictions having applications in various research fields, such as flood forecast, drought monitoring and agriculture.

However, among the challenges in retrieving soil moisture from spatially distributed passive microwave observations (brightness temperature, T_B) is the requirement to account for the effects of vegetation. For large scale soil moisture retrieval applications, correcting for the vegetation effects is based on the semi-empirical radiative transfer approach (Mo et al. 1982), which accounts for the: 1) attenuation of the microwave surface emission, 2) emission by vegetation and 3) vegetation emission scattered to surface reflected by the soil. Attenuation of the soil surface emission and emission by vegetation are accounted for through formulation of the transmissivity coefficient (γ), while scattering of surface emission within the canopy is parameterized by the single scattering albedo (ω). Based on a detailed parameterization of the vegetation morphology, physically-based scattering models are able to provide an accurate characterization of γ and ω . However, the implementation of such complex scattering models is rather cumbersome because the required parameterization is difficult to implement through integration of ground measurements and remote sensing techniques. Therefore, for large scale soil moisture retrieval applications, the ω is assumed to be a time-invariant constant depending only on the vegetation morphology, while γ is,

typically, implemented as a time dependent variable affected by the vegetation morphology as well as the density of the vegetation (e.g. biomass). For the retrieval of soil moisture, γ is an important variable describing the vegetation effects, because spatial as well as temporal variations in vegetation cover affect this parameter.

For the determination of γ in large scale soil moisture retrieval applications, two different approaches can be adopted: 1) employing multiple T_B observations acquired during a time step, or 2) adopting of the ancillary data approach. Because the required ancillary data for global soil moisture retrieval applications may not be available at that scale, many studies have investigated the direct retrieval of γ from multi-channel microwave observations (e.g. Bindlish et al. 2003, Wen et al. 2003, and Owe et al. 2001).

However, γ could be polarization dependent, because the emitted radiation is differently attenuated and scattered as the orientation of the elements in the canopy layer changes relative to the direction of the polarization (Wigneron et al. 2004; Parde et al. 2003). In addition, the γ is frequency (or wavelength) dependent, because the surface emission is differently attenuated as the dimension of the elements in the canopy layer changes relative to the wavelength (Jackson and O'Neill 1990; Van de Griend and Wigneron 2004).

Therefore, single channel retrieval algorithms, which use the ancillary data approach, are considered as the most robust solution. The ancillary data approach is based upon the formulation of γ as a function of the vegetation water content and an empirical constant, the b parameter. Experimental investigations have shown that the empirical constant is

specific for each crop type and may depend on the morphology of the vegetation cover. However, within soil moisture retrieval algorithms operational on a global scale the empirical constant is, typically, implemented as a single time-invariant parameter. Temporal variations in the empirical constant may, therefore, affect the determination of the appropriate γ and the retrieval of soil moisture.

1.2 Research goals and objectives

The goal of this research is to improve the quantification of the transmissivity coefficient for soil moisture retrieval from satellite microwave radiometers on global scales. To achieve this goal, the objective of this research is to quantify uncertainties in the empirical constant induced by temporal variations in the vegetation cover. The proposed methodology to address this objective will consist of two parts:

Using ground based radiometer data sets; the variability in the empirical constants over specific agricultural vegetation covers (e.g. corn and soybeans) will be quantified using the semi-empirical, ancillary data approach;

Physically-based scattering models will be employed to simulate the transmissivity coefficient based on input of vegetation morphology. From the simulated transmissivity values the empirical constants will be derived.

1.3 Research questions

In carrying out this research, the following questions were addressed:

1. What is the variability of the empirical constant derived from radiometer observations using the semi-empirical ancillary data approach?
2. What is the variability of the empirical constant obtained through simulations with a physically based model using vegetation morphology parameterizations collected over the corn growth cycle?
3. What is the influence of these uncertainties in the empirical constant on the retrieval of the soil moisture?
4. Is it possible to develop a methodology to account for possible seasonal variations in the empirical constant?

Through determination of the variability in the empirical constant derived from the radiometer observations and theoretical simulations, the uncertainty in the soil moisture retrievals imposed by the empirical constant can be determined. Moreover, using the physically-based scattering model, empirical constants can be derived for vegetation type, for which no ground based radiometer data sets are available. The results from this research will provide an improved understanding of the behavior of the empirical constant in relation to the vegetation morphology. This improved knowledge about the behavior of the empirical constant can then be used for implementation within global soil

Introduction

moisture retrieval algorithms. Moreover, quantification of the soil moisture retrieval uncertainty induced by the empirical constant can be utilized for the assimilation of soil moisture products into hydrological and weather prediction models resulting in more accurate forecasts.

This dissertation is composed of 6 chapters including this introduction. Chapter 2 is a background of L-band emission modeling, the Tor Vergata model, and a brief description of the study sites used in the analysis of this dissertation. Further details on the study sites are included in chapters 3 through 5. Presented in chapter 3 is the entire journal publication “L band brightness temperature observations over a corn canopy during the entire growth cycle”, which appeared in the Sensors journal in 2010. Chapter 4 is based on the journal article “Soil moisture retrieval during a corn growth cycle using L-band (1.6 GHz) radar observation”, which is currently in review for publication in the Remote Sensing of Environment journal. Chapter 5 is based on the journal article “Modeling L-band emission during the corn growth cycle using a discrete medium scattering model”, which is to be submitted to the IEEE Transactions on Geoscience and Remote Sensing. Chapter 6 is the summary and conclusions.

2 Background

2.1 Emission from soil

The surface emissivity is typically described in terms of the surface reflectivity. This is convenient because the microwave reflectivity under smooth surface conditions can theoretically be derived from Maxwell's equations (the Fresnel reflectivity). Fresnel reflectivity (R_0^p) for Horizontal (H) and Vertical (V) polarizations for smooth soil surface is given as follows,

$$R_0^H = \left| \frac{\cos \theta - \sqrt{\varepsilon - \sin^2 \theta}}{\cos \theta + \sqrt{\varepsilon - \sin^2 \theta}} \right| \quad (2.1)$$

$$R_0^V = \left| \frac{\varepsilon \cos \theta - \sqrt{\varepsilon - \sin^2 \theta}}{\varepsilon \cos \theta + \sqrt{\varepsilon - \sin^2 \theta}} \right| \quad (2.2)$$

where, θ is the incidence angle (degrees), and ε is the soil dielectric constant calculated here using dielectric mixing model by Dobson et al. (1985) as a function of the soil moisture content and soil textural properties.

In the real world, however, soil surfaces are rough. This roughness increases the surface per unit area contributing to the microwave emission and this decreases the surface reflectivity. Moreover, the roughness causes part of the radiation emitted in a particular polarization to be scattered within the soil surface and transmitted to the antenna in the other polarization, often referred to as polarization mixing. Wang and Choudhury (1981) developed a semi-empirical model that takes these two effects of soil surface roughness into account. In its most general form this model is written as,

$$R_s^p = [(1-Q)R_0^p + QR_0^q] \exp(-h_r \cos^{N_R} \theta) \quad (2.3)$$

where, h_r quantifies the increase in emission as the surface roughness (or surface area) increases, N_R describes the angular dependence of h_r , Q is the polarization mixing parameter and R_0 is the Fresnel reflectivity defined for the H and V polarization.

A much debated part in this formulation is the angular dependence of the roughness effect. Originally, Wang and Choudhury (1981) took N_R equal to 2.0, while others (e.g. Wang et al. 1983, Wegmüller and Mätzer 1999) suggested that lower values are more appropriate. Recently, Escorihuela et al. (2007) found that N_R also attains different values for the H and V polarization.

For this study, two implementations are used; Firstly, $Q \neq 0$ is adopted and fixed values for N_R are used (Chapter 2). Secondly, $Q=0$ is utilized while various N_R values are evaluated, recognizing that both the H and V polarized R_0 vary with the incidence and the assumption $Q=0$ can be compensated by N_{RH} (Chapter 3).

2.2 Vegetation effects on emission

The effect of vegetation on microwave emission includes both absorption and scattering. The absorbing properties of vegetation attenuate the soil surface emission. At the same time, the absorption is also equivalent to the emission by the canopy itself when Kirchhoff's Law is applicable and the soil-vegetation system is in a thermodynamic equilibrium. Apart from these zeroth order mechanisms, radiation emitted by crops may also be scattered within the canopy. Figure 2-1 illustrates these sources of microwave

emission. Typically, the transmissivity (γ) quantifies the absorbing properties of a canopy, whereas the single scattering albedo (ω) is used within semi-empirical models to account for the effects of scattering by vegetation.

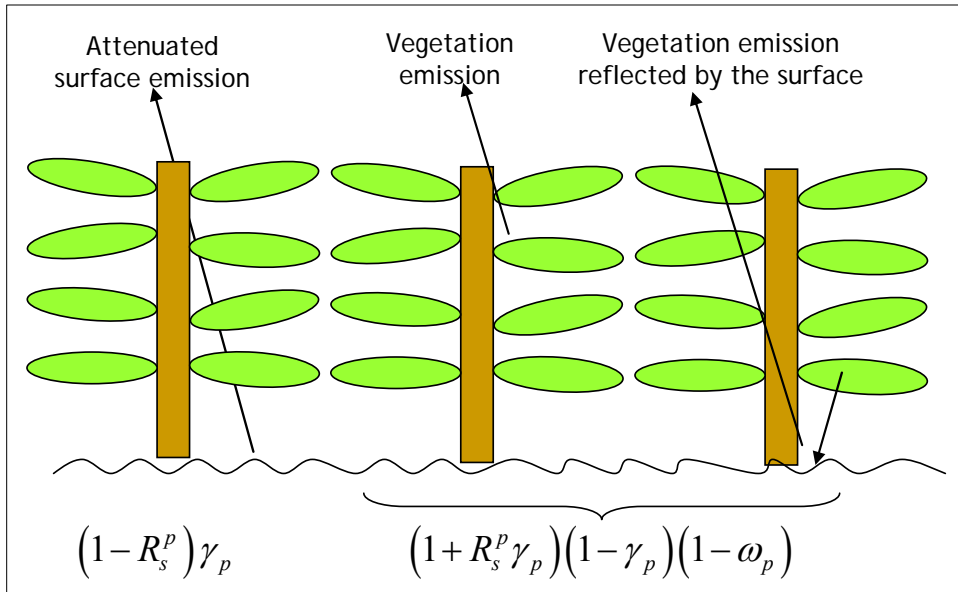


Figure 2-1: Effects of vegetation on microwave emission from the soil-vegetation system.

The amount of radiation scattered within the canopy and can be computed as,

$$\omega_p = \frac{\kappa_s^p}{\kappa_s^p + \kappa_a^p} \quad (2.4)$$

where, κ_s and κ_a are the scattering and absorption coefficients, respectively and p is the H and V polarization.

These scattering and absorption coefficients can be obtained through application of the discrete medium approach (examples are given in section 2.4), in which individual

Background

components of the vegetation layer (leaves and stems) are represented by elliptical and/or cylindrical dielectric scatterers. Alternatively, ω is assumed to be negligible or a variable dependent on the growth stage, which can be determined from controlled experiments where all other variables (e.g. soil moisture, temperature of emitting layer, surface roughness and transmissivity) are measured.

The γ describes the amount of soil emission passing through the vegetation layer. The one-way γ through the canopy layer can be formulated as,

$$\gamma_p = \exp\left[\frac{-\tau_p}{\cos\theta}\right] \quad (2.5)$$

where, τ is the optical depth or canopy opacity and p is the H and V polarization, which can be calculated using,

$$\tau_p = k_{ep} h_v \quad (2.6)$$

With

$$k_{ep} = \frac{4\pi}{\lambda} n_o \text{Im}(f_{pp}) \quad (2.7)$$

where, h_v is the canopy height, k_{ep} is a polarization dependent extinction coefficient, n_o is the number of phytoelements per unit volume, λ is the wavelength and $\text{Im}(f_{pp})$ is the imaginary part of the scattering matrix.

Within the SMOS soil moisture retrieval algorithm, the τ is calculated as an empirical linear function of the Leaf Area Index (LAI) as these products are derived from satellite observations at a global scale. A more traditional formulation originates from Kirdyashev et al. (1979) whom related τ to the dry biomass and its imaginary part of the dielectric constant. Jackson et al. (1982) simplified this relationship by taking τ equal to the product of the W and an empirical parameter, b , that depends on canopy structure and sensing configuration (e.g. frequency, polarization, incidence angle) as follows,

$$\tau_p = b \cdot W \quad (2.8)$$

Both b and ω are frequently included in retrieval algorithms as a single land cover specific value for entire growing season assigned based on a land cover map and existing databases. Summaries of research related to the value of these parameters for various crop types can be found in Jackson and Schmugge (1991) and Van de Griend and Wigneron (2004a, b).

2.3 Semi-empirical emission modeling

Mo et al. (1982) described a semi-empirical radiative transfer approach for microwave emission from a homogeneous soil-vegetation system, commonly known as the τ - ω model. Nowadays, most soil moisture retrievals algorithms (e.g. Bindlish et al. 2003, Wen et al. 2003, Owe et al. 2008) for passive microwaves are based on this model, including SMOS L2 soil moisture processor described in Wigneron et al. (2007).

Background

Assuming that the contribution from the atmosphere is negligible, the p polarized T_B is computed by the τ - ω model as,

$$T_B^p = (1 + R_s^p \gamma_p)(1 - \gamma_p)(1 - \omega_p)T_v + (1 - R_s^p)\gamma_p T_s \quad (2.9)$$

where, R_s is the soil surface reflectivity (= 1- soil surface emissivity, e_s) (-), γ is the transmissivity (-), ω is the single scattering albedo (-), T_s and T_c are respectively the soil and canopy temperatures (K), and sub- and superscript p indicates that the variable is representative for the H or V polarization.

As shown in Figure 2-1, the first term on the right hand side of Eq. (2.9) represents the microwave emission directly by vegetation and the radiation emitted by the vegetation reflected by the soil surface back towards the sensor. The second term quantifies the emission contribution from the soil, corrected for the energy absorbed by the vegetation layer.

The solution to this radiative transfer approach requires parameterization of the vegetation and soil surface layer radiative transfer properties as presented in the previous two sections. Additionally, temperatures of the vegetation and the emitting soil surface layer are needed. However, when assuming the vegetation and soil surface are in thermal equilibrium with each other, T_s and T_v can be considered equal. This condition occurs typically near dawn. The required temperature is then considered representative for the emitting layer. In this dissertation, applications of the τ - ω model are presented in Chapters 3 and 4. Details on the utilized parameterizations are given therein.

2.4 Physically based emission modeling

The semi-empirical τ - ω model uses an effective parameterization to represent the electromagnetic properties of vegetation, while in fact a canopy consists of several types of scatterers (e.g. leaves, stems) with specific dielectric and geometric properties. Discrete medium scattering models are able to include the effects of the dielectric and geometric state of individual plant components in emission and backscatter simulations. From this physical viewpoint the emission from vegetation covered soil can be represented as,

$$e_p(\theta) = 1 - W_p(\theta) \quad (2.10)$$

where, e is the emissivity and W is the scattering albedo.

The scattering albedo, $W_p(\theta)$, can be decomposed into a specular (*spec*) and a diffuse (*dif*) component, according to,

$$W_p(\theta) = W_p^{spec}(\theta) + W_p^{dif}(\theta) \quad (2.11)$$

The specular component represents the radiation reflected specularly from the ground attenuated by the canopy formulated as,

$$W_p^{spec}(\theta) = |R_p(\theta)|^2 \exp[-4 \operatorname{Im}(\kappa_p) d] \quad (2.12)$$

Background

where, R is the surface reflectivity, κ is the propagated constant, d is the height of the canopy, and \mathbf{Im} is the imaginary part of the propagated constant.

The diffuse component of the scattering albedo represents the scattering within the canopy and requires integration of the scattering coefficients over the hemisphere above the soil surface,

$$W_p^{dif}(\theta) = \frac{1}{4\pi \cos^2 \theta} \int [\sigma_{hp}^o(\bar{o}, \bar{i}) + \sigma_{vp}^o(\bar{o}, \bar{i})] \cos(\theta_s) d\Omega_s \quad (2.13)$$

where, $d\Omega_s = \sin(\theta_s) d\theta_s d\varphi$, \mathbf{o} is the unit vector in the observation direction, \mathbf{i} is the unit vector in the incident direction.

The scattering cross section can be computed using a scattering approach formulation in the following general form,

$$\sigma_{pq}^o(\bar{o}, \bar{i}) = \sigma_{pq,s}^o(\bar{o}, \bar{i}) + \sigma_{pq,dr}^o(\bar{o}, \bar{i}) + \sigma_{pq,r}^o(\bar{o}, \bar{i}) + \sigma_{pq,d}^o(\bar{o}, \bar{i}) \quad (2.14)$$

where, $\sigma_{pq,s}^o$ is the soil scattering component, $\sigma_{pq,d}^o$ is the direct scattering component, $\sigma_{pq,dr}^o$ is the direct-reflected scattering component and $\sigma_{pq,r}^o$ is the reflected scattering contribution.

The scattering mechanisms described in Eq. 2.14 are illustrated in Figure 2-2. The computation of these scattering contributions requires the formulation of the scattering amplitudes ($f_{pq}(\mathbf{o}, \mathbf{i})$) and the propagation constants. Within physically based models, these scattering amplitudes and propagation constants are determined based on the dielectric

properties, size and orientation of a specific type of scatterer represented by a predefined shape. For example, thin dielectric disks are commonly used to model leaves whereby typically the Rayleigh-Gans approximation (Eom and Fung 1984) is invoked for the low frequency domain and the Physical Optics approximation (Le Vine et al. 1983) for the high frequency domain. Further, cylinders are often used for stems through application of the infinite length approximation (Seker and Schneider 1988).

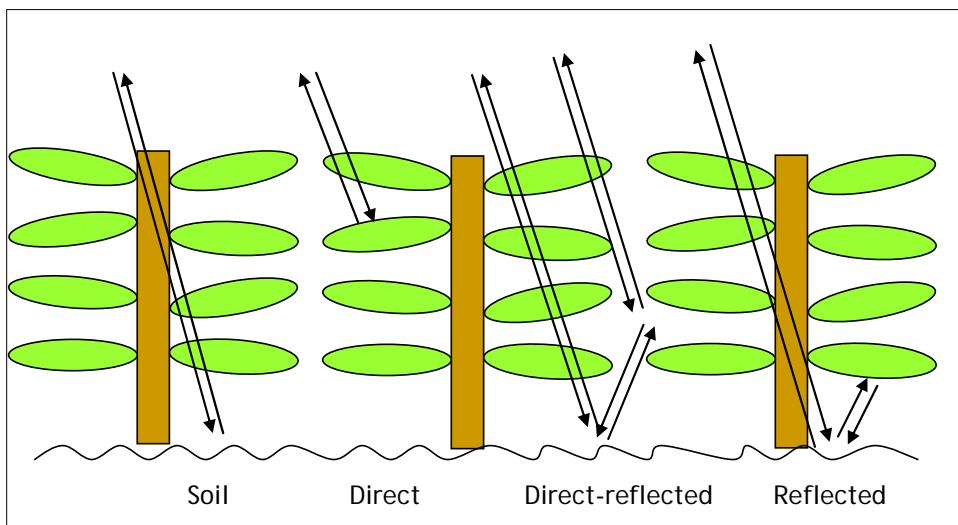


Figure 2-2: Scattering mechanisms described by Eq. 2.14.

After the electromagnetic properties of the individual scatterers with the canopy are quantified, their combined effect should be integrated over the entire vegetation layer. Then, the computation of the emissivity or backscatter coefficient with a discrete medium approach can either be based on the *wave theory* (e.g. Chauhan et al. 1991, Chauhan et al. 1994, Saatchi et al. 1994) or on the *radiative transfer theory* or *transport theory* (e.g. Ulaby et al. 1990, Karam et al. 1992, Ferrazzoli and Guerriero 1996 and Karam, 1997).

Background

In the application of the wave theory presented by Chauhan et al. (1994), a mean electric field is defined using Green's functions, which is solved using the *Foldy-Lax approximation*. This approximation assumes the incident field on each particle is approximately the same as the average field. A consequence of Foldy-Lax approximation is that solutions are only valid for media with weakly fluctuating permittivities (or dielectric constants), which limits its application to remote sensing observations acquired at long wavelengths with respect to the dimensions of the scatterers. The distorted Born approximation is, then, used to compute the backscattered field from the scatterers within the discrete medium describing the canopy layer. The *distorted Born approximation* applies fluctuations of the dimension, orientation and location to the mean electric field based on probability density functions, which is valid when the scatterers have a small albedo. For agricultural canopies, this assumption may hold up to frequencies of 10 GHz.

Physical scattering models that make use of the radiative transfer theory (e.g. Ferrazzoli and Guerriero 1996) focus on describing the transport of microwave radiation through the canopy layer. Scattering and absorption characteristics of elements within the canopy layer (e.g. trunks, leaves and branches) are defined through the scattering and extinction cross section. Different algorithms can be used to compute the bistatic scattering coefficients from these scattering and transmissivity matrices. Ulaby et al. (1990, MIMICS) uses a first order approximation, Karam et al. (1992) extended the solution to a second order approximation and Bracaglia et al. (1995) employed the Matrix Doubling algorithm. The advantage of the Matrix Doubling algorithm is that through its

application multiple scattering between different vegetation layers are taken into account.

For this dissertation the model described in Bracaglia et al. (1995) is applied to determine theoretically the effects of changes in the vegetation morphology throughout the growth cycle. Hereafter, this discrete medium scattering model is referred to as the Tor Vergata model and a brief description is given in section 2.5.

2.5 Tor Vergata model

The Tor Vergata model (Bracaglia et al. 1995) is a discrete medium scattering modeling method that adopts a radiative transfer approach. The model represents the generic architecture of agricultural crops as thin dielectric discs for the foliage and cylinders for the stems as shown in Figure 2-3. The electromagnetic behavior of discs is simulated using the Rayleigh-Gans approximation (e.g. Eom and Fung 1984) for frequencies lower than 5.0 GHz and the infinite length approximation is utilized for the cylinders (Seker and Schneider 1988). Further, the scattering by the soil surface is simulated using Integral Equation Method (IEM, Fung et al. 1992) surface scattering model.

2.6 Electromagnetic representation of the canopy

Calculation of the scattering and absorption by a canopy requires a characterization of the physical dimensions, orientation and permittivity of the scatterers within the discrete

Background

medium. The leaf coverage is parameterized by the leaf area index (LAI), leaf thickness and disc radius, whereby the LAI and leaf thickness are inputted and a fixed disc radius of 3.5 cm is used. Then, the number of discs within the medium is obtained by dividing the LAI by the disc's surface area. The stem radius and length define its dimensions and the number of stems is used to quantify the density of the scattering medium.

The Eulerian angles (α , β , γ) describe the *orientation* of the scatterers according to schematization in Figure 2-4. In the Tor Vergata model the minimum and maximum position can be defined, over which the scattering amplitude functions are averaged with an interval of 1.0 degree.

Further, the Tor Vergata model calculated the *permittivity of the vegetation layer* using either the method developed by Mätzler (1994) or the one by Ulaby and El-Rayes (1987). Both approaches compute the permittivity as a function of the fresh and dry biomass. The simulations presented in this dissertation are only performed using Mätzler's approach.

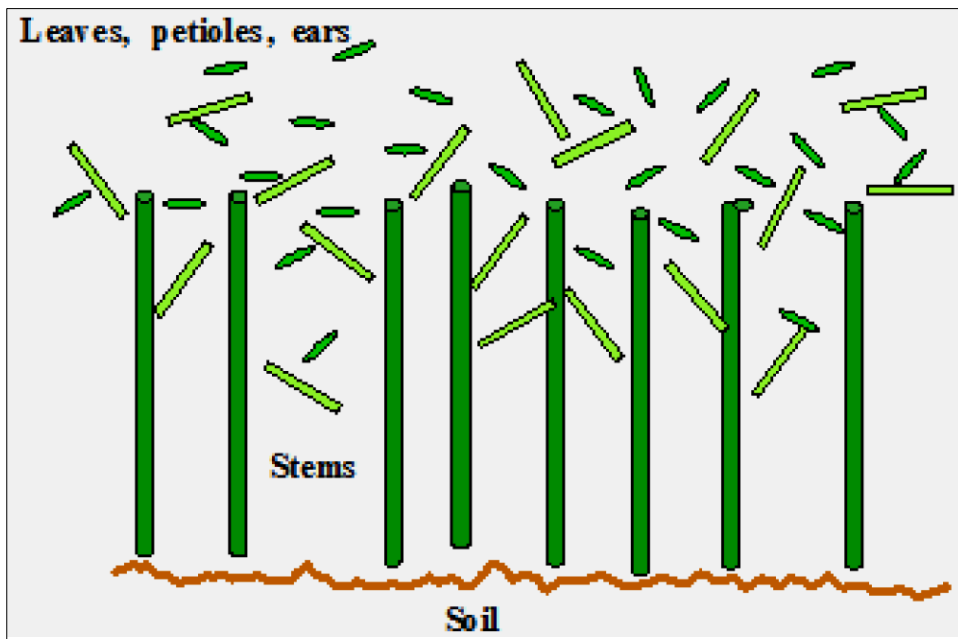


Figure 2-3: Schematization of the canopy architecture presented by the Tor Vergata model (adopted from Della Vecchia 2006).

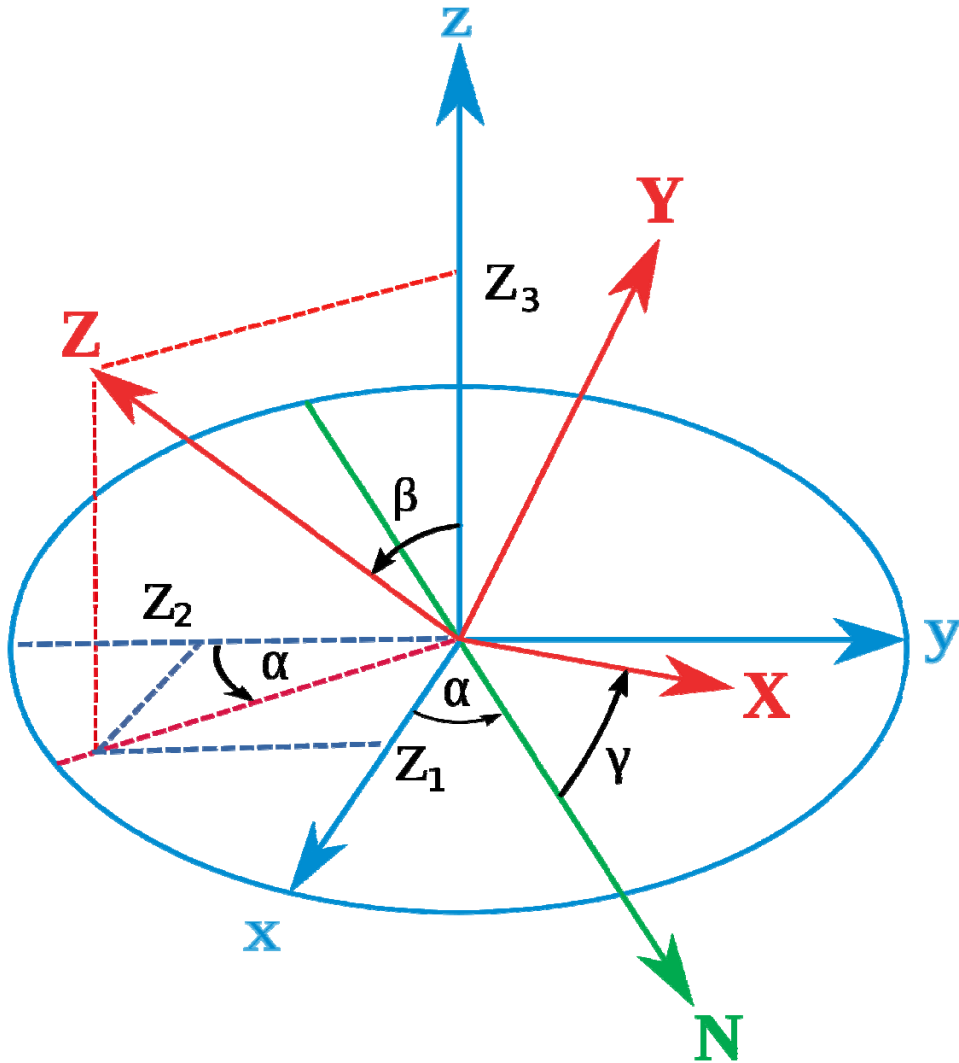


Figure 2-4: Eulerian angles (α , β , γ) used to define the orientation of scatterers with a medium.

2.7 Electromagnetic representation of the soil

As the IEM surface scattering model is utilized, the Tor Vergata model requires similar soil variables to compute the surface scattering contribution. This parameterization defined the surface geometry and the soil permittivity.

Within the IEM the *surface geometry* is based on a stochastic representation of the surface height variations. This characterization consists of three parameters, namely the root mean square height (s), autocorrelation length (l) and autocorrelation function (ACF). The parameters, s and l , are input to the model, while the ACF is typically fixed as being either a Gaussian or an Exponential function. The Tor Vergata model simulations presented in this dissertation are performed using only the Exponential ACF's because this shape has been found to be most appropriate for smooth agricultural surfaces (e.g. Oh et al. 1992, Davidson et al. 2000).

The *soil permittivity* can be calculated by the Tor Vergata model using the semi-empirical dielectric mixing model developed by Dobson et al. (1985) and also the generalized refractive dielectric mixing model by Mironov et al. (2009) has been included in the Tor Vergata modeling system. For many years, Dobson's mixing model has been one of "the standards" for obtaining the soil permittivity as a function of moisture content and texture. Recent enhanced validations showed, however, that the permittivities obtained with Dobson's model tend to overestimate the measurements. The permittivity model described in Mironov et al. (2009) makes an explicit distinction between the electromagnetic properties of bound and free water. This added complexity allows the Mironov model to produce more accurate estimates of the soil permittivity. Both mixing models are considered for the simulations presented in this dissertation.

2.8 Integrating the effects of individual scatterers

Via the Rayleigh-Gans approximation for foliage and the infinite length approximation for stems, the Tor Vergata model determines the scattering and absorption (or transmission) matrices of individual scatterers with the discrete medium. Then, the multiple scattering interactions among the scatterers within the medium are considered through application of the Matrix Doubling algorithm described in Eom and Fung (1984).

For the Matrix Doubling, the entire canopy is subdivided into layers with thickness Δz . Then, the scattering and absorption matrices of a single layer for downward travelling radiation (see left panel Figure 2-5) can be defined as,

$$\mathbf{S} = \mathbf{M}^{-1} \boldsymbol{\kappa}_e \mathbf{P}(\mu_s, -\mu_i, \varphi_s - \varphi_i) \Delta z \quad (2.15a)$$

$$\mathbf{T} = \mathbf{M}^{-1} \boldsymbol{\kappa}_e \mathbf{P}(-\mu_t, -\mu_i, \varphi_t - \varphi_i) \Delta z \quad (2.15b)$$

where, \mathbf{S} is the scattering matrix, \mathbf{T} is the transmission matrix, \mathbf{M} is the diagonal matrix of directional cosine, $\boldsymbol{\kappa}_e$ is the extinction matrix, \mathbf{P} is the phase matrix, μ is cosine of the angle between z -axis and wave, φ is the angle between the wave and x -axis and subscripts i , s , and t indicate the incident, scattered and transmitted energy.

Hence, for upward travelling radiation (see right panel of Figure 2-5) the scattering and transmission matrices are formulated as,

$$\mathbf{S}^* = \mathbf{M}^{-1} \boldsymbol{\kappa}_e \mathbf{P}(-\mu_s, \mu_i, \varphi_s - \varphi_i) \Delta z \quad (2.16a)$$

$$\mathbf{T}^* = \mathbf{M}^{-1} \boldsymbol{\kappa}_e \mathbf{P}(\mu_i, -\mu_i, \varphi_i - \varphi_i) \Delta z \quad (2.16b)$$

Through the combination of the scattering and transmission matrices for downward and upward travelling radiation of two layers with thickness Δz , the \mathbf{S} , \mathbf{T} , \mathbf{S}^* and \mathbf{T}^* can be computed for a layer of thickness $2\Delta z$ as follows,

$$\mathbf{S} = \mathbf{S}_1 + \mathbf{T}_1^* \mathbf{S}_2 (\mathbf{I} - \mathbf{S}_1^* \mathbf{S}_2)^{-1} \mathbf{T}_1 \quad (2.17a)$$

$$\mathbf{T} = \mathbf{T}_2 (\mathbf{I} - \mathbf{S}_1^* \mathbf{S}_2)^{-1} \mathbf{T}_1 \quad (2.17b)$$

$$\mathbf{S}^* = \mathbf{S}_1^* + \mathbf{T}_1 \mathbf{S}_2^* (\mathbf{I} - \mathbf{S}_1 \mathbf{S}_2^*)^{-1} \mathbf{T}_1^* \quad (2.17c)$$

$$\mathbf{T}^* = \mathbf{T}_2^* (\mathbf{I} - \mathbf{S}_1 \mathbf{S}_2^*)^{-1} \mathbf{T}_1^* \quad (2.17d)$$

where, \mathbf{I} is the identity matrix.

In case the two layers have identical properties the equations 2.17(a)-2.17(d) represent the doubling of the matrices. This process can be repeated to obtain the phase matrices of a medium with any thickness. Figure 2-6 visualizes this principle of matrix doubling.

2.9 Backscatter and emissivity calculation

Once the scattering and transmission matrices have been integrated over the entire vegetation layer, the total scattering matrix (\mathbf{S}_T) can be calculated using,

$$\mathbf{S}_T = \mathbf{S}_v + \mathbf{T}_v^* \mathbf{S}_g (\mathbf{I} - \mathbf{S}_v^* \mathbf{S}_g) \mathbf{T}_v \quad (2.18)$$

where, subscripts v and g indicates that the property is defined for the vegetation layer or the soil surface, respectively.

Background

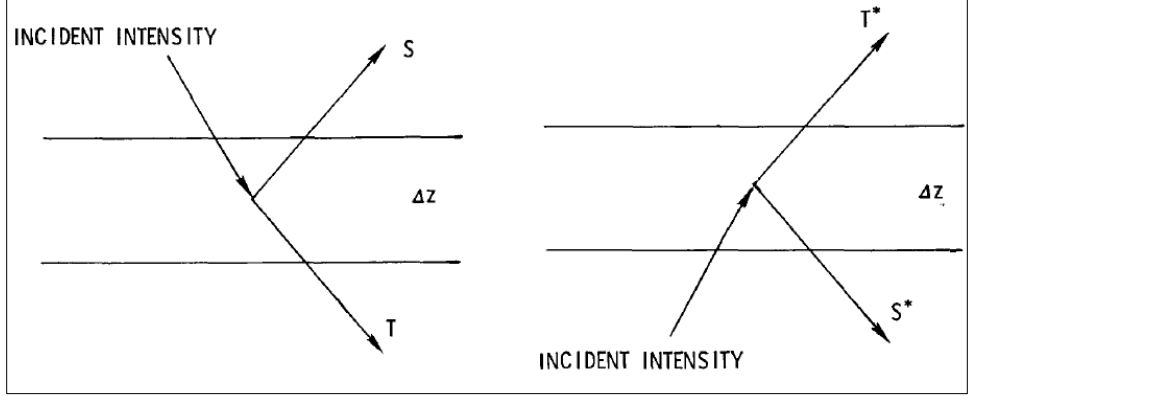


Figure 2-5: Scattering and transmission matrices for downward (left) and upward (right) travelling radiation (adopted from Eom and Fung 1984).

In Equation 2.18, the first term on the right-hand side represents the direct vegetation term, while the second term includes the soil scattering contribution attenuated by the canopy and scattering along the soil-vegetation pathways. From the k th row and l th column element of the p, q polarized Stokes parameter in S_T the bistatic scattering coefficient $\sigma_{pq}^o(\theta_k, \theta_{sl}, \varphi_s - \varphi)$ can be obtained using,

$$\sigma_{pq}^o(\theta_{sk}, \theta_l, \varphi_s - \varphi) = \frac{4\pi}{\Delta\theta} \cot\theta \left[S_T(\theta_{sk}, \theta_l, \varphi_s - \varphi) \right]_{pq} \quad (2.19)$$

Via integrating the bistatic scattering coefficient over the upper half space, the total reflectivity (or albedo) of microwave radiation in the hemisphere is obtained. Since the reflectivity is complementary to the emissivity, its computation is as follows,

$$e_p(\theta) = 1 - \frac{1}{4\pi} \int_0^{2\pi} \int_0^{\frac{\pi}{2}} \sum_{p=1}^2 \frac{\sigma_{pq}^o(\theta, \theta_s, \varphi_s)}{\cos\theta} \sin\theta_s d\theta_s d\varphi_s \quad (2.20)$$

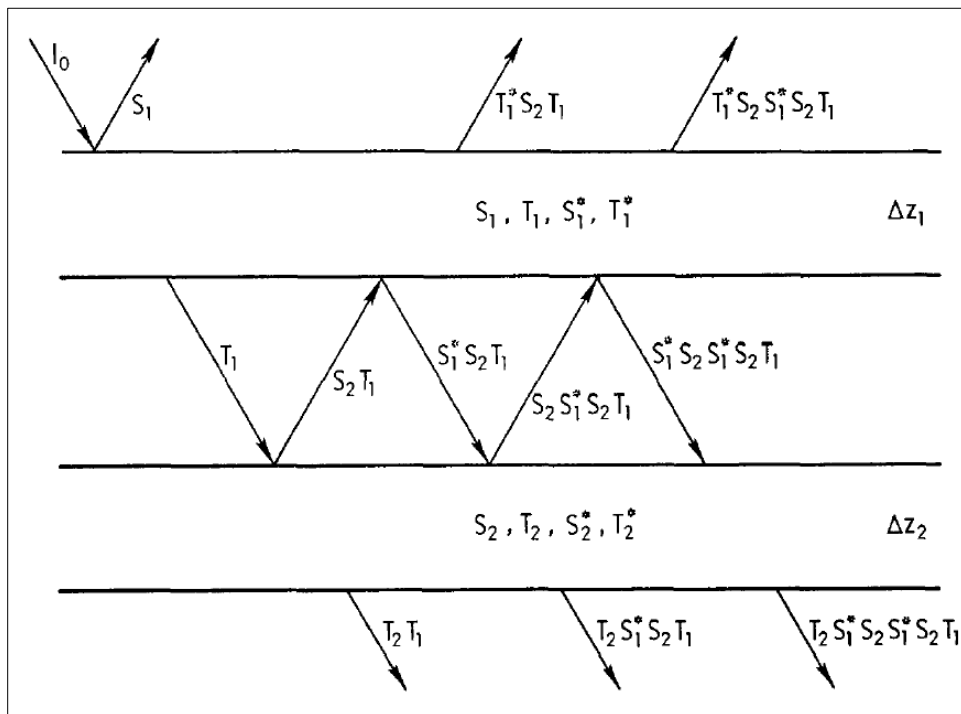


Figure 2-6: Combination scattering and transmission matrices for a multi-layered medium (adopted from Eom and Fung 1984).

2.10 Study sites

Two L-band radiometer data sets were used for the research presented in this dissertation.

The main data set under investigation was obtained by an automated dual polarized L-band radiometer, called LRAD. Its measurements were collected as a part of a field campaign that covered the 2002 corn growth cycle in Beltsville, Maryland. This campaign took place at the USDA Hydrology and Remote Sensing Laboratory's (HRSL)

Background

research site; commonly referred to as the OPE^{31*} site (Gish et al., 2003). Henceforth, this campaign is referred to as the ‘2002 OPE³ campaign’.

Further, the L-band radiometer data sets collected in 1981 over bare fields at the USDA’s Beltsville Agricultural Research Center (BARC) were utilized. During the experiments at the BARC facility in 1981, the L-band T_B were measured over different rough surfaces. As such, analysis presented in Chapter 3 using the BARC data set are included to present a more complete analysis of the angular dependence of the roughness effect on microwave emission.

Both data sets are further described in the text below.

2.11 1981 BARC experiments

General description

The 1981 BARC experiments took place during the months July to September in 1981. The main objective of this campaign was to investigate the impact of the soil type on the radiometric response; the two test sites selected for the analysis of this dissertation addresses this objective. The first site has a soil type named Elinsboro sandy loam with 67% sand, 19% silt and 14 % clay. The soil type at the second site is referred to as Mattapex silty loam that consists of 32% sand, 43% silt and 25% clay.

At both sites radiometric measurements were made over vegetated as well as bare soil plots each of about 20 by 20 meters in size. The vegetation types included in the experiment were grass, winter wheat, alfalfa, soybean and corn. Further, the radiometric

¹ OPE³ ~ Optimizing Production Inputs for Economic and Environmental Enhancements

measurements over bare soils were conducted over a very smooth plot at the Elinsboro site, and at the Mattapex site a smooth and a rough surface were prepared. A root mean squared height (s) of 0.21 was measured at the Elinsboro site and at the Mattapex bare plots s values of 0.73 and 2.45 were measured.

Radiometric measurements

For the 1981 BARC experiments, three radiometers were deployed each mounted on the same mobile tower and operating at frequencies of 1.4, 5.0, and 10.7 GHz, respectively. The antennas of the radiometers all have comparable 3-dB beamwidth of about 13° and the radiometers are of the Dicke-type with two internal calibration targets. The hot calibration target has a temperature of 310 K and the cold calibration target is maintained at a temperature of 77 K using liquid nitrogen.

An absolute calibration of the radiometers is obtained against three external targets with known T_B 's, which include the cold sky (~ 5 K), a calm water surface and a blackbody (emissivity = 1.0) formed by a layer of Eccosorb slabs with an ambient temperature. Both sky and Eccosorb calibrations were performed at least once during each measurements day. The calm water surface calibration was made twice throughout the entire measurements period. The results from the calibrations of the radiometers are shown in Figure 2-7. Linear regression functions fitted through the data points have a coefficient of determination larger than 0.99, and the accuracy of the radiometer is estimated at about ± 3 K.

Background

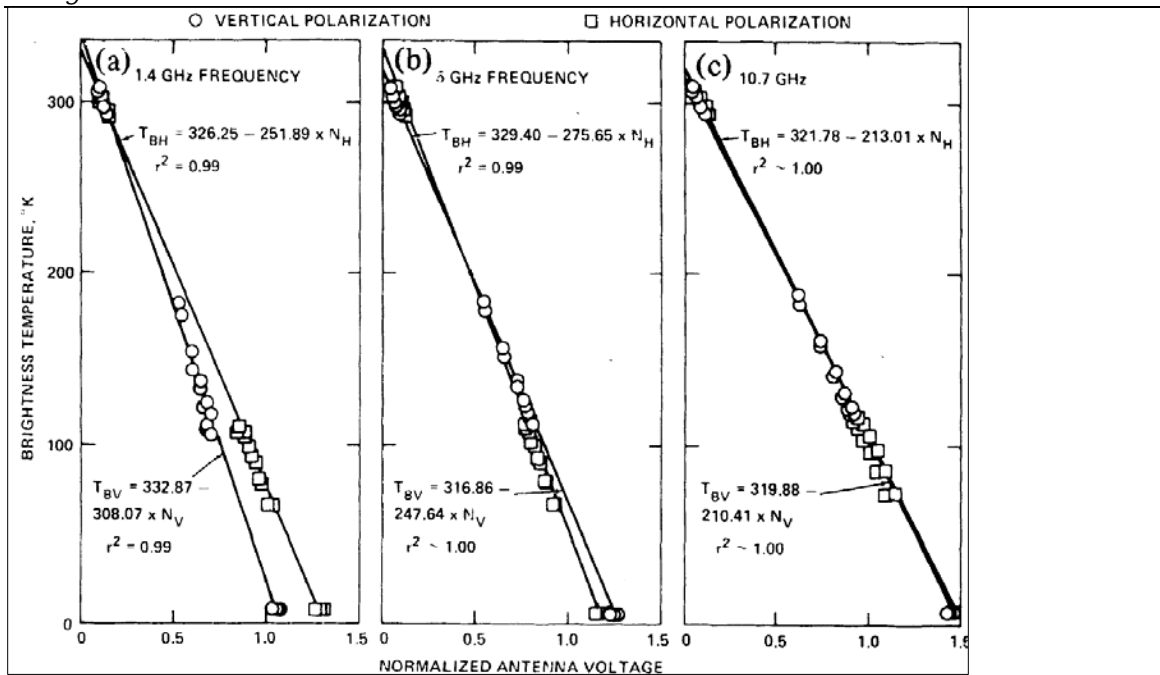


Figure 2-7: The results from calibration of the microwave radiometers (a) 1.4 GHz, (b) 5 GHz and (c) 10.7 GHz operated during the 1981 BARC experiments (adopted from Wang et al. 1983).

The field operations consisted of radiometric measurements collected from incidence angles varying from 10° to 70° with an interval step of 10° . The majority of the measurement days (12 in total) at the Mattapex bare soil plots took place in Mid-August, while the bare soil measurements at the Elinsboro site (in total 23 days) were conducted from Mid-July till the end of September.

In this dissertation, research is presented using only the L-band radiometer data set collected over bare soils.

Ground truth

In support of the radiometric measurements, a ground truth characterization took place which included *in-situ* measurements of vegetation, surface roughness, soil moisture and temperature. A gravimetric sampling technique was used for measuring the soil moisture content over depths of 0.0-0.5 cm, 0.0-2.5 cm, 2.5-5.0 cm and 5.0-10.0 cm. Concurrent to each sequence of radiometric observations, two soil samples were taken close to the footprints. Further, the soil temperatures were measured by Omega-platinum resistance thermometers at depths of 0.25, 1.25, 2.50, 7.50 and 15.00 cm.

These ground measurements were used for the radiative transfer modeling described in Chapter 3.

Background

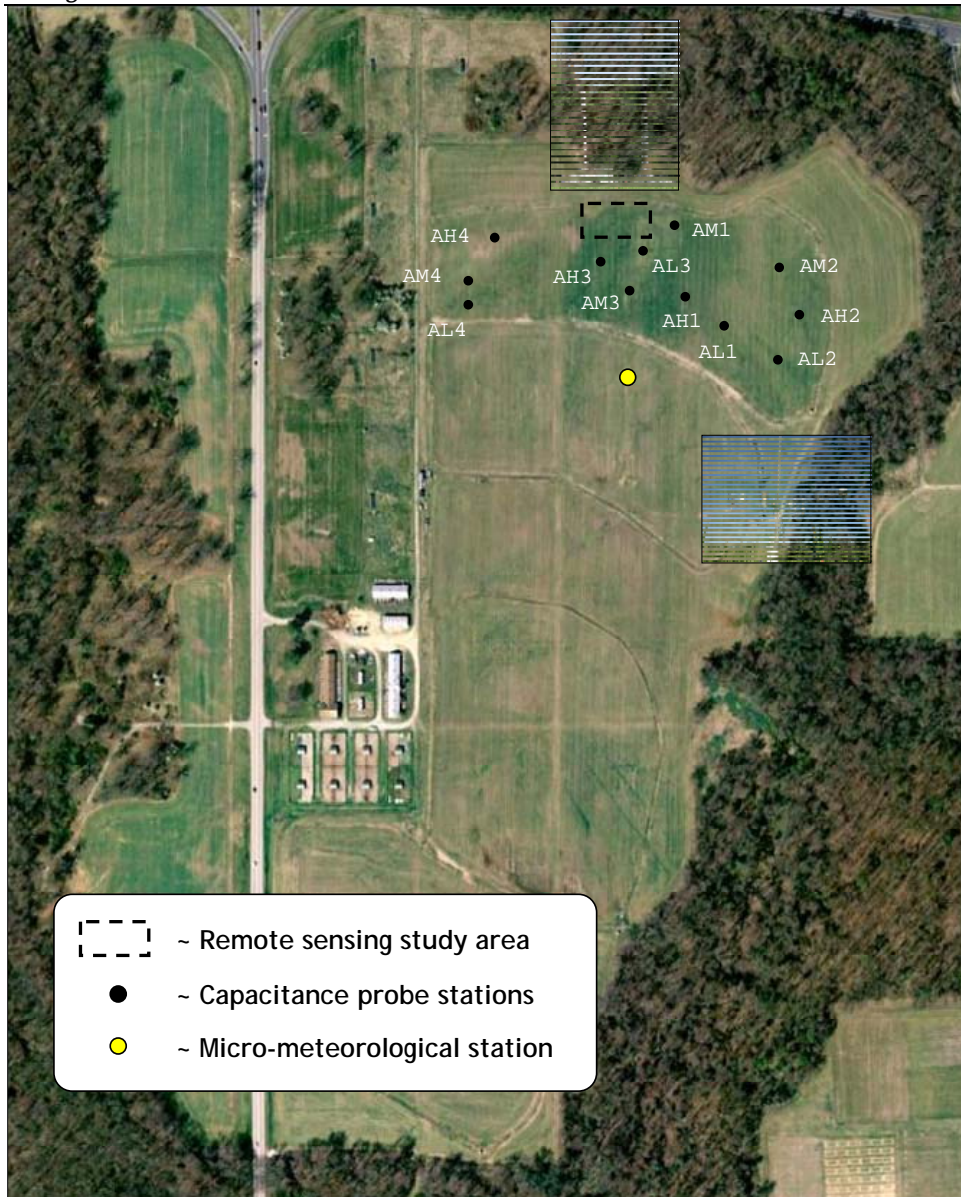


Figure 2-8: Experimental setup during the 2002 remote sensing campaign at the OPE3 site.

2.12 2002 OPE³ campaign

Site description

The field at the Beltsville Agricultural Research Center (BARC) referred to as the Optimizing Production Inputs for Economic and Environment Enhancement (OPE³) site (Gish et al., 2003) was the focal point of a microwave remote sensing campaign in 2002. This research facility is located about 5 kilometers east from Beltsville (Maryland, USA) at an elevation of 40 meters above mean sea level and includes four watersheds each with an area of 4 hectares. Climate in this region is dominated by mild winters and hot (and humid) summers. The annual rainfall amounts on average 990 mm.

In 2002, the microwave instruments were placed in the most northern part of the OPE³ site, in which the soil texture is classified as sandy loam with 23.5% silt, 60.3% sand, 16.1% clay and a bulk density of 1.25 g cm⁻³. Non-automated measurements of soil moisture, temperature and vegetation biomass were taken manually directly around the periphery of the scatterometer/ radiometer footprints and are hereafter referred to as *labor intensive measurements*. Automated meteorological and soil moisture stations are available within a short distance. An outline of this experimental setup is given in Figure 2-8. Further information on the OPE³ project can be found at <http://hydrolab.arsusda.gov/ope3> (verified December 6th, 2010).

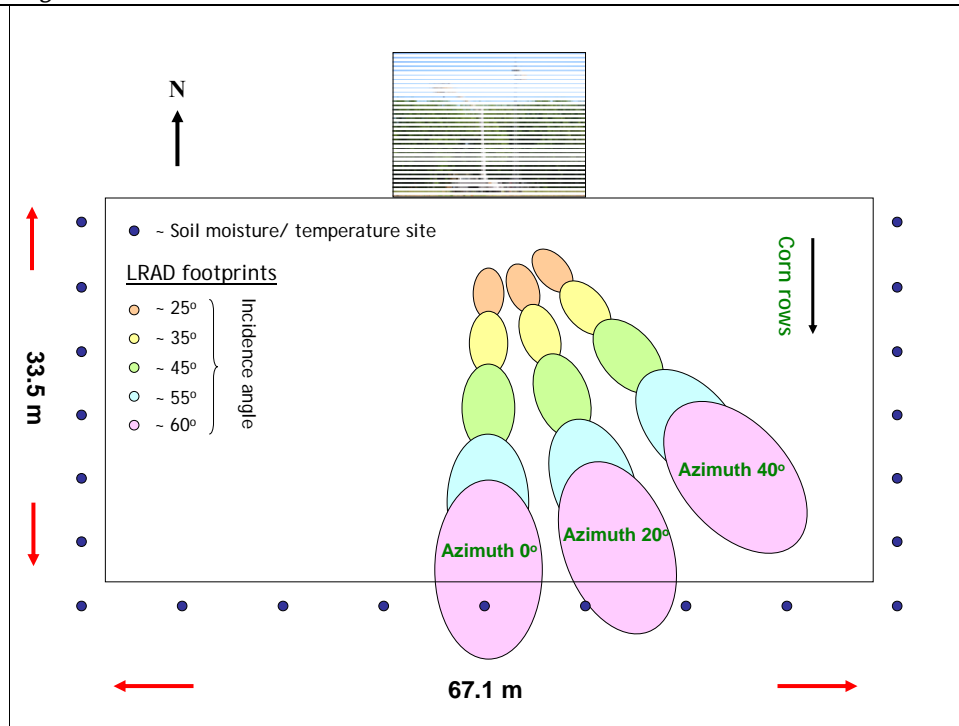


Figure 2-9: Diagram of the LRAD footprints.

L-band radiometer (LRAD) data

The L-band radiometer (LRAD) is a dual-polarized passive sensor operating at 1.4 GHz and a 3-dB half power beam width of about 12°. Calibration of the T_B measurements is obtained by pointing the antenna towards two reference targets with known temperatures. A microwave absorber with an ambient temperature monitored by the system itself was taken as a hot target and the sky with an assumed L-band T_B of 5 K (3 K cosmic background radiation and 2 K atmospheric contribution) was adopted as a cold target. Then, assuming the system has a linear response, the T_B is calculated by,

$$T_B^P = A \cdot U_p + B \quad (2.21)$$

where, T_B^p is the p polarized (either horizontal (H) or vertical (V)) brightness temperature (K), U_p is the p polarized LRAD measurement (Volt), and A and B are two calibration constants (K/Volt and K, resp.) that are obtained from the two reference measurements following,

$$A = \frac{T_B^{abs} - T_B^{sky}}{U_{abs} - U_{sky}} \quad (2.22)$$

$$B = T_B^{sky} - \frac{T_B^{abs} - T_B^{sky}}{U_{abs} - U_{sky}} U_{sky} \quad (2.23)$$

where, U is the LRAD measurement of the reference target (Volt) and sub-/superscripts abs and sky are used to refer to either the microwave absorber or the sky target.

For the field campaign in 2002, LRAD was mounted on an 18-m portable tower, and was programmed to take measurements every hour at five incidence angles (25° , 35° , 45° , 55° , and 60°) and at three azimuth angles. As illustrated in Figure 2-9, the azimuth angles were parallel to corn rows, and respectively 20° and 40° across the row direction. Before and after each sequence, LRAD collected measurements from the microwave absorber target and the sky.

As both pre- and post-calibration parameters are uncertain, the two sky and absorber voltages as well as the two absorber temperatures are averaged to derive the calibration constants, A and B . The A values derived using the reference target measurements varied for the H-polarization from 304.5 to 678.7 K/Volt throughout the campaign. Given LRAD recorded its measurements at a resolution of $1.0 \cdot 10^{-3}$ Volt, the T_B were monitored

Background

with a radiometric resolution varying from 0.304 to 0.678 K. The overall accuracy of the calibrated H polarized T_B is estimated to be better than 2 K. As some issues related to calibration of the V polarization remain, these measurements are not included in the analysis presented here.

Despite intermittent failures of the scanning mechanism of LRAD's automated hourly data collection system, over 700 sequences were completed of which many were consecutive. The focus of this investigation lies, therefore, on the analysis of diurnal T_B cycles collected during five periods with significant variations in vegetation cover. In addition, three shorter measurement episodes over virtually bare soil conditions are used to evaluate the impact of soil surface roughness. The start and end of each episode with continuous hourly LRAD data are listed in Table 2-1 for both the vegetated and bare soil conditions.

The corn biomass was measured using a destructive approach based on cutting all (about 12) plants within a 1 m² area and recording the weights of fresh and over-dried biomass. Figure 2-10 shows the measurements of the total water content (W), and fresh and dry biomass as well as the water content of individual plant constituents (e.g. leaves, stems and cobs) over time. As observed, the W at peak biomass is about 5.1 kg m⁻² and a maximum canopy height of 2.2 m was measured.

Table 2-1: Episodes with sequence of hourly LRAD measurements collected during the 2002 OPE³ remote sensing campaign.

	<i>Start</i> <i>date, time</i>	<i>End</i> <i>date, time</i>	<i>SM range</i> $\text{m}^3 \text{m}^{-3}$	<i>W</i> kg m^{-2}	<i>N</i> #
<i>bare soil</i>	21 May, 22 ^{h00}	22 May, 13 ^{h00}	0.20-0.21	0.03	16
<i>bare soil</i>	23 May, 21 ^{h00}	24 May, 6 ^{h00}	0.19-0.18	0.04	10
<i>bare soil</i>	29 May, 15 ^{h00}	30 May, 4 ^{h00}	0.17-0.16	0.09	14
<i>vegetation</i>	8 June, 8 ^{h00}	10 June, 13 ^{h00}	0.22-0.18	0.3	54
<i>vegetation</i>	24 June, 15 ^{h00}	27 June, 14 ^{h00}	0.14-0.11	1.0	72
<i>vegetation</i>	2 July, 16 ^{h00}	4 July, 21 ^{h00}	0.09-0.06	4.2	54
<i>vegetation</i>	20 August, 20 ^{h00}	23 August, 10 ^{h00}	0.02-0.01	2.7	63
<i>vegetation</i>	29 August, 0 ^{h00}	3 Sept., 14 ^{h00}	0.28-0.23	2.1	75

Top 0.06-m soil moisture and soil temperatures at depths of 0.03- and 0.07-m were measured at twenty-one locations around the footprints shown in Figure 2-9. Portable impedance probes (Delta-T Theta-probe, Type: ML2x) were used to measure soil moisture and the soil temperatures were obtained using Extech Instruments digital stem thermometers. From the start till the end of the campaign, one temperature and two impedance probe readings were taken per location each time the radar/radiometer collected data, which was typically around 8:00, 10:00, 12:00 and 14:00 hours. Additionally, soil temperatures were recorded during week days at nominal times of 8:00 and 14:00 hours. Moreover, the canopy temperature was monitored from July 3 using an Omega handheld infrared thermometer.

Further, soil samples were taken coincident to the first radar/radiometer acquisitions of a measurement day for a gravimetric determination of the volumetric soil moisture (θ_v), which was used to establish a site specific calibration for the impedance probe readings. Details about this calibration procedure are available in Joseph et al. (2010b). The Root

Background

Mean Squared Difference (RMSD) between the gravimetric and calibrated impedance probe θ_v is found to be $0.024 \text{ m}^3 \text{ m}^{-3}$.

Complementary to this extensive ground sampling, the OPE³ site is equipped permanently with several automated instruments. Specifically of interest to this study is the soil moisture network that consists of 48 stations (12 in each watershed). The stations include either 3 or 6 capacitance soil moisture probes (EnviroSCAN, SENTEK Pty Ltd., South Australia) depending on the infiltration rate, which are installed at depths of 0.1, 0.3, 0.8 m or at depth of 0.1, 0.3, 0.5, 1.2, 1.5 and 1.8 m, respectively. The EnviroSCAN probes observe the moisture content in a soil volume with a radius of 0.1 m from sensor's center and at the OPE³ site their readings are recorded every 10 minutes. The location of stations in the northern watershed is shown in Figure 2-8. The location of the other stations and additional details can be found in De Lannoy et al. (2006).

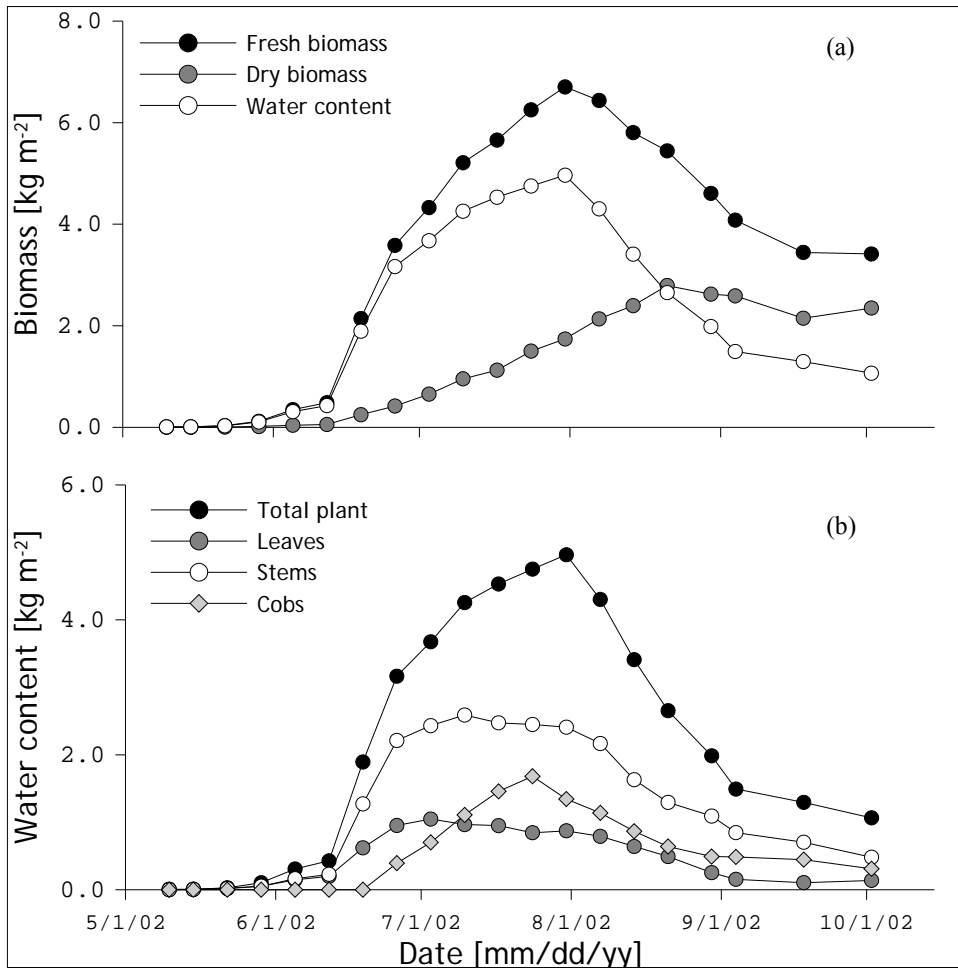


Figure 2-10: Measurements of a) total water content, and fresh and dry biomass and b) water content of individual plant components during the 2002 OPE³ campaign.

Further, located about 100 m from the radiometer footprints is a micro-meteorological station, which provides a detailed surface energy balance characterization (Crow et al. 2008). At this station, two Apogee Instruments Incorporated precision infrared radiometers (type: IRTS-P3) are mounted at height of 4.5 m above ground level pointing towards the east and west at a view angle of 45° . This type of radiometer measures the radiative temperature with an accuracy of 0.15°C over the $6.5 - 14\ \mu\text{m}$ spectral range

Background

using a Field Of View (FOV) of 18.4° . The area observed is, thus, 7.35 m^2 at ground level and 1.93 m^2 at the maximum corn height of 2.2 m. In addition, Type-T thermocouples installed at depths of 0.02 and 0.06 m monitor the soil temperature at six locations about 10 meters from the station. The thermocouples as well as the infrared radiometers recorded data every 30 minutes.

3 Angular dependence of the soil roughness effect on microwave emission

This chapter is based on:

Joseph, A.T., van der Velde, R., O'Neill, P.E., Choudhury, B.J., Lang, R.H., Kim, E.J., Gish, T., (2010), "L band brightness temperature observations over a corn canopy during the entire growth cycle", *Sensors*, **10**, pp. 6980-7001.

Abstract: During a field campaign covering the 2002 corn growing season, a dual polarized tower mounted L-band (1.4 GHz) radiometer (LRAD) provided brightness temperature (T_B) measurements at preset intervals, incidence and azimuth angles. These radiometer measurements were supported by an extensive characterization of land surface variables including soil moisture, soil temperature, vegetation biomass, and surface roughness. During the period from May 22, 2002 to August 30, 2002 a range of vegetation water content (W) of 0.0 to 4.3 kg m⁻², ten days of radiometer and ground measurements were available. Using this data set, the effects of corn vegetation on surface emissions are investigated by means of a semi-empirical radiative transfer model. Additionally, the impact of roughness on the surface emission is quantified using T_B measurements over bare soil conditions. Subsequently, the estimated roughness parameters, ground measurements and horizontally (H)-polarized T_B are employed to invert the H-polarized transmissivity (γ_h) for the monitored corn growing season.

Keywords: Field campaign, L-band radiometry, vegetation effects, surface roughness

3.1 Introduction

Low frequency passive microwave observations have been intensively studied for their potential of retrieving soil moisture [e.g. Jackson (1993), Wigneron et al. (2007), and Owe et al. (2008)]. Studies have demonstrated that when an appropriate characterization of vegetation, soil surface roughness and dielectric properties are applied, soil moisture can be retrieved fairly accurate from the brightness temperatures (T_B 's) measured by microwave radiometers [e.g. Saleh et al. (2009), Panciera et al. (2009)]. As a result, the Soil Moisture and Ocean Salinity (SMOS [Kerr et al. (2001)]) mission is the first of three L-band radiometers designed for global soil moisture monitoring purposes to be launched. In the near future, the Aquarius and Soil Moisture Active Passive (SMAP [Entekhabi et al. (2004)]) missions will follow; their expected launch dates are in spring 2010 and in 2013, respectively. With this increased availability of low frequency spaceborne radiometer observations, new opportunities arise for monitoring soil moisture globally.

However, among the challenges in retrieving soil moisture from T_B measurements is to account for soil surface roughness and vegetation effects. Most retrieval approaches utilize similar radiative transfer equations [3.8-3.10]. These methods estimate the vegetation transmissivity (γ) using either multiple channel microwave data or ancillary data. Because the required ancillary data for global soil moisture retrieval applications may not be available at that scale, direct retrieval of the γ is preferred. However, the γ is polarization as well as wavelength (or frequency) dependent because the emitted

radiation is differently attenuated as the orientation of the elements in the canopy layer changes relative to the wavelength and the direction of the polarization [e.g. Jackson and O'Neill (1990), Wigneron et al. (2004), Van de Griend and Wigneron (2004)]

Therefore, large scale soil moisture monitoring studies [e.g. Drusch et al. (2004), Cashion et al. (2005), and Bindlish et al. (2008)] frequently adopt an ancillary data approach to determine the γ , which has been extensively described in the scientific literature [e.g. Jackson and Schmugge (1991), Schmugge and Jackson (1992)]. This characterization of the γ requires knowledge of the vegetation water content (W), and a crop-specific and frequency dependent empirical parameter b (elaborated below). The Normalized Difference Vegetation Index (NDVI) and related indices have been suggested as a surrogate for W in large-scale studies [e.g. Bindlish et al. (2003), Jackson et al. (2004)]. Then, the empirical parameter b should be implemented as a land cover specific parameter assigned based on a classification map.

Selection of the appropriate parameterization for a specific land cover relies, however, often on parameter sets derived from T_B measurements collected during past intensive field campaigns [e.g. Van de Griend and Wigneron (2004), Jackson and Schmugge (1991)]. By default, the validity of those parameterizations is restricted to the conditions for which they have been derived. Many of the past field campaigns covered, for example, a part of the growth cycle of agricultural crops. Therefore, the development of the γ and b parameter throughout the growth cycle is not fully understood.

This paper contributes to this understanding by analyzing the L-band H-polarized T_B 's measured throughout the complete 2002 corn (*Zea mays* L.) growth cycle. The utilized data set has been collected at one of the fields of the Beltsville Agricultural Research Center (BARC) by an automated tower mounted L-band (1.4 GHz) radiometer (called LRAD) starting from May 22 till the beginning of September. These radiometer measurements are supported by a detailed land surface characterization, which took place about once every week and included measurements of the vegetation biomass, soil moisture and soil temperature. Despite mechanical difficulties with scanning system of LRAD produced gaps in the data record, a total of ten days distributed over the growing season of both radiometer and ground measurements are available covering a W range from 0.0 to 4.3 kg m⁻².

The objective of this investigation is to evaluate the variations in the γ and the empirical parameter b over the monitored corn growth cycle. To this aim, first, the impact of the surface roughness on the surface emission is quantified using the LRAD T_B 's over bare soil conditions and an older data set collected at the BARC facility. Subsequently, the γ (and b parameter) are inverted from individual T_B measurements using the estimated roughness parameterization, and measured soil moisture and soil temperature. In addition, an analysis is presented of the sensitivity of the derived b parameters for uncertainties in the LRAD T_B and the assigned single scattering albedo (ω).

3.2 Theoretical background

The starting point for the computation of microwave emission from vegetated surfaces is the semi-empirical radiative transfer approach by Mo et al. (1982), which is based on the assumption that at L-band attenuation is more dominant than scattering,

$$T_B^p = (1 + R_s^p \gamma_p) (1 - \gamma_p) (1 - \omega_p) T_v + (1 - R_s^p) \gamma_p T_s \quad (3.1)$$

where, T_B^p is the polarized brightness temperature, R_s^p is the soil surface reflectivity (= 1- emissivity), γ_p is the transmissivity of vegetation, ω_p is the single scattering albedo, T_s and T_v are the soil and canopy temperatures, respectively, and superscript and subscript p indicates polarization.

The first term on the right hand side of Eq. (3.1) represents the microwave emission directly by vegetation and the radiation emitted by the vegetation reflected by the soil surface back towards the sensor. The second term quantifies the emission contribution from the soil, corrected for the energy absorbed by the vegetation layer.

The solution to the radiative transfer equation requires parameterization of the vegetation and soil surface layer radiative transfer properties. Further, temperatures of the vegetation and soil surface layer are required. However, when assuming the vegetation and soil surface are in thermal equilibrium with each other, T_s and T_v can be considered equal; this condition occurs typically near dawn. The required temperature is then considered representative for the emitting layer.

Emission from soil

The solution to the radiative transfer equation requires parameterization of the vegetation and soil surface layer radiative transfer properties. Further, temperatures of the vegetation and soil surface layer are required. However, when assuming the vegetation and soil surface are in thermal equilibrium with each other, T_s and T_v can be considered equal; this condition occurs typically near dawn. The required temperature is then considered representative for the emitting layer.

The surface emissivity is typically described in terms of the surface reflectivity. This is convenient because the microwave reflectivity under smooth surface conditions can be theoretically derived from Maxwell's equations (the Fresnel reflectivity). Fresnel reflectivity (R^p) for H- and V-polarizations for smooth soil surface are given as follows,

$$R^H(\theta) = \left| \frac{\cos \theta - (\epsilon_r - \sin^2 \theta)^{\frac{1}{2}}}{\cos \theta + (\epsilon_r - \sin^2 \theta)^{\frac{1}{2}}} \right|^2 \quad (3.2a)$$

$$R^V(\theta) = \left| \frac{\epsilon_r \cos \theta - (\epsilon_r - \sin^2 \theta)^{\frac{1}{2}}}{\epsilon_r \cos \theta + (\epsilon_r - \sin^2 \theta)^{\frac{1}{2}}} \right|^2 \quad (3.2b)$$

where, ϵ_r is the dielectric constant of soil, θ is the incidence angle.

In this study, the approach described by Wang and Choudhury (1981) has been adopted to account for the effect of surface roughness on the reflectivity. This approach involves

two parameters, where one parameter has an attenuating effect on the surface reflectivity and the other accounts for the depolarizing effect of the surface roughness,

$$R_s^p(\theta) = \left[(1-Q)R^p + QR^q \right] \exp(-h G(\theta)) \quad (3.3)$$

where, h is roughness parameter given by $4k^2\sigma^2$ with k as the wavenumber ($2\pi/\lambda$) and σ as the root mean square (*rms*) height of the surface height variations, Q is a polarization mixing factor, $G(\theta)$ is a function describing the view angle dependency of the h parameter and superscript q represents the polarization orthogonal to polarization p , which can be either horizontal (H) or vertical (V).

Originally, Wang and Choudhury (1981) took the function $G(\theta)$ equal to $\cos^2 \theta$. However, Wang et al. (1983) have found that the dependence of $\cos^2 \theta$ is much too strong and replaced it by $G(\theta) = 1.0$ for best fitting their data. The latter is initially adopted here.

Vegetation effects on soil surface emission

Within the radiative transfer approach, vegetation effects are characterized by two parameters: transmissivity (γ) and single scattering albedo (ω). The ω is a measure for the amount of radiation scattered within the canopy and can be computed as follows,

$$\omega_p = \frac{\kappa_s^p}{\kappa_s^p + \kappa_a^p} \quad (3.4)$$

where, κ_s^p and κ_a^p are the scattering and absorption coefficients, respectively.

These scattering and absorption coefficients can be obtained through application of the discrete medium approach (Lang and Sidhu 1983, Chauhan 1997, and O'Neill et al. 1996), in which individual components of the vegetation layer (leaves and stems) are represented by elliptical and/or cylindrical dielectric scatterers. Alternatively, the ω is assumed to be negligible or a variable dependent on the growth stage, which can be determined from controlled experiments where all other variables (e.g. soil moisture, temperature of emitting layer, surface roughness and transmissivity) are measured.

The transmissivity describes the amount of soil emission passing through the vegetation layer and is an important variable for quantification of the effect of vegetation on microwave emission. The one-way transmissivity through the canopy layer is formulated as,

$$\gamma_p = \exp\left(\frac{-\tau_p}{\cos \theta}\right) \quad (3.5)$$

where, τ_p is the polarization dependent optical depth [Wigneron et al. (2004)] or canopy opacity, which can be calculated using,

$$\tau_p = k_{ep} h_v \quad (3.6)$$

with

$$k_{ep} = \frac{4\pi}{\lambda} n_o \text{Im} \langle f_{pp} \rangle \quad (3.7)$$

where, h_v is the canopy height, k_{ep} is a polarization dependent extinction coefficient, n_o is the number of phytoelements per unit volume, λ is the wavelength and $\text{Im} \langle f_{pp} \rangle$ is the imaginary part of the polarization dependent scattering matrix.

Several studies [Wigneron et al. (2004), Van de Griend and Wigneron (2004), Jackson and Schmugge (1991)] have shown that τ_p can be related to the vegetation water content as,

$$\tau_p = b_p \cdot W \quad (3.8)$$

where, W is the vegetation water content and b_p is an empirical parameter varying with crop type, canopy structure, wavelength, and polarization [Wigneron et al. (2004)].

Eq. (3.8) for soil moisture retrieval requires information about vegetation class, W , and b_p parameters for different types of vegetation, and has been widely adopted and has been proposed as part of the soil moisture retrieval algorithms for current and future microwave radiometers [e.g. Njoku (1999), Kerr et al. (2006)].

3.3 The OPE³ experiment

Site description

The present study was conducted at Optimizing Production Inputs for Economic and Environmental Enhancement (OPE³) test site managed by the USDA-ARS (United States Department of Agriculture- Agricultural Research Service) [Gish et al. (2003)]. The site consists of four adjacent watersheds with similar surface and sub-surface soil and water flow characteristics and covers an area of 25 ha near Beltsville, Maryland (Figure 3-1). Each of the four watersheds is formed from sandy fluvial deposits and has a varying slope ranging from 1% to 4%. The soil textural properties are classified as sandy loam with 23.5% silt, 60.3% sand, 16.1% clay, and bulk density of 1.25 g cm⁻³. A detailed description of the research activities can be found at <http://hydrolab.arsusda.gov/ope3>. (Verified December 6, 2010).

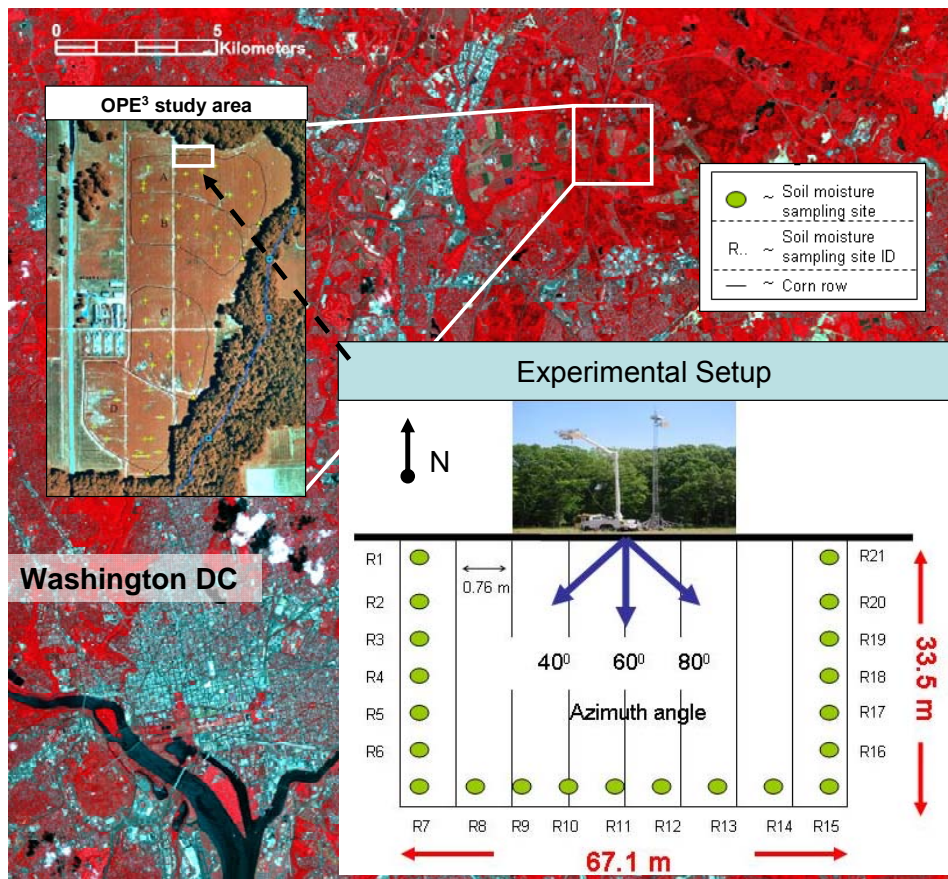


Figure 3-1: Location and schematization of the OPE³ remote sensing experimental setup in 2002.

Ground measurements

The in-situ measurement strategy was designed to provide ground information to supplement the radar and radiometer data acquisitions, and took place every Wednesday, rainy days excluded. In this paper, an analysis of the radiometer observations is presented. A description of the radar data set is given in Joseph et al. (2008).

During the field campaign (May 10 to October 2, 2002) representative soil moisture, soil temperature, vegetation biomass (wet and dry) and surface roughness measurements were taken around the radiometer footprints. Soil moisture and soil temperature

measurements were collected at twenty-one sites located at the edge of a 67.1 m x 33.5 m rectangular area depicted in Figure 3-1. Vegetation biomass and surface roughness measurements were taken around the study area at representative locations.

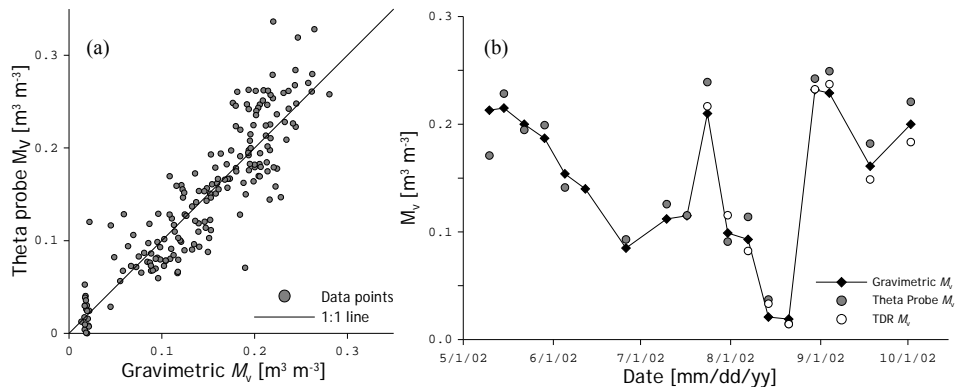


Figure 3-2: (a) Comparison of the calibrated theta probe soil moisture against the gravimetrically determined soil moisture content converted to volumetric values. (b) Volumetric soil moisture (M_v) as measured by the theta probe, TDR and determined through a gravimetric sampling technique plotted against time.

Soil moisture and Soil temperature

Soil moisture was measured using gravimetric, portable impedance probe (Delta-T theta probe²), and buried impedance probe (Time Domain Reflectometry (TDR)) techniques. Soil samples of the top 6-cm soil layer were collected at the beginning of each day in conjunction with the theta probe measurements primarily for calibration purposes. Theta probe measurements were collected typically at 8:00, 10:00, 12:00 and 14:00 hours (USA Eastern). The buried TDR probes were installed at locations R5, R11 and R18 (Figure 3-1) at various depths (5, 10 and 20 cm) and insertion angles (horizontal, vertical, and 45 degrees).

² The US Government does not endorse any specific brand of impedance probe for measuring soil moisture.

Relative dielectric constant (ϵ_r) measured by the theta probe were converted to volumetric soil moisture (M_v) values by fitting a linear regression function through the following relationship (figure 3-2a),

$$\sqrt{\epsilon_r} = a_0 + a_1 \cdot M_v \quad (3.9)$$

where, a_0 and a_1 are regression parameters.

While general soil texture-specific parameters are available [Miller and Gaskin (1996)], a site specific calibration was performed. To achieve this, soil moisture determined gravimetrically from the soil samples was converted to M_v and used with concurrent probe observations to fit for each site a specific a_0 and a_1 parameter. Comparison of the calibrated theta probe M_v values with the gravimetric M_v (see Figure 3-2a) gives a root mean squared error (RSME) of $0.024 \text{ m}^3 \text{ m}^{-3}$, which is comparable to calibration errors obtained with theta probe observations collected in several remote sensing campaigns [Cosh et al. (2005)]. In Figure 3-2b, the soil moisture observed by the three different measuring techniques are displayed as time series for comparison purposes. As shown in Figure 3-2b, the soil moisture values observed with the theta probe, gravimetric and TDR instruments are in agreement with each other, which justifies the use of each of their products.

Soil temperature measurements were taken manually at soil depths of 3- and 7-cm at each of the twenty-one sampling locations (annotated as R1 to R21 in Figure 3-1)

throughout the experiment using Extech Instruments digital stem thermometers³. On intensive sampling days the soil temperatures were measured at 8:00, 10:00, 12:00, 14:00 hours, and the measurements on other days were taken approximately every two days at 8:00 and 14:00 hours.

Although the study area was selected to minimize the possible effects of land surface heterogeneity, small surface height and soil texture variations could potentially influence the representativeness of the measured soil moisture and temperature for the radiometer footprints. These effects are studied by evaluating the spatial soil moisture and temperature variability measured around the footprints. In Figures 3-3a and 3-3b, averages of the gravimetric M_v and soil temperature measured during the entire campaign are plotted for each site. Figure 3-3a shows that the western boundary (site R1-R6) is consistently wetter than the eastern boundary (site R16-R21). The difference between the maximum and minimum average soil moisture values observed in the study area is $0.04 \text{ m}^3 \text{ m}^{-3}$ (with $0.17 \text{ m}^3 \text{ m}^{-3}$ at site R9 and $0.13 \text{ m}^3 \text{ m}^{-3}$ at site R20). However, compared to the uncertainties in soil moisture measurements in general, see for example theta probe calibration uncertainty of $0.024 \text{ m}^3 \text{ m}^{-3}$, this difference between the minimum and maximum averaged soil moisture is relatively small. We consider, therefore, the soil moisture variability around the radiometer footprint to be small and the mean of the twenty-one measurements representative for the radiometer footprint.

³ The US Government does not endorse any specific brand of digital thermometers.

Vegetation

Corn was planted on April 17, reached peak biomass around July 24 and was harvested on October 2. Vegetation biomass and morphology were quantified through destructive measurements applied to 1 m² area (approximately 12 plants) once every week at 8:00 am. The water content, fresh and dry biomasses were determined separately for the individual plant constituents, such as leaves stems and cobs (when present).

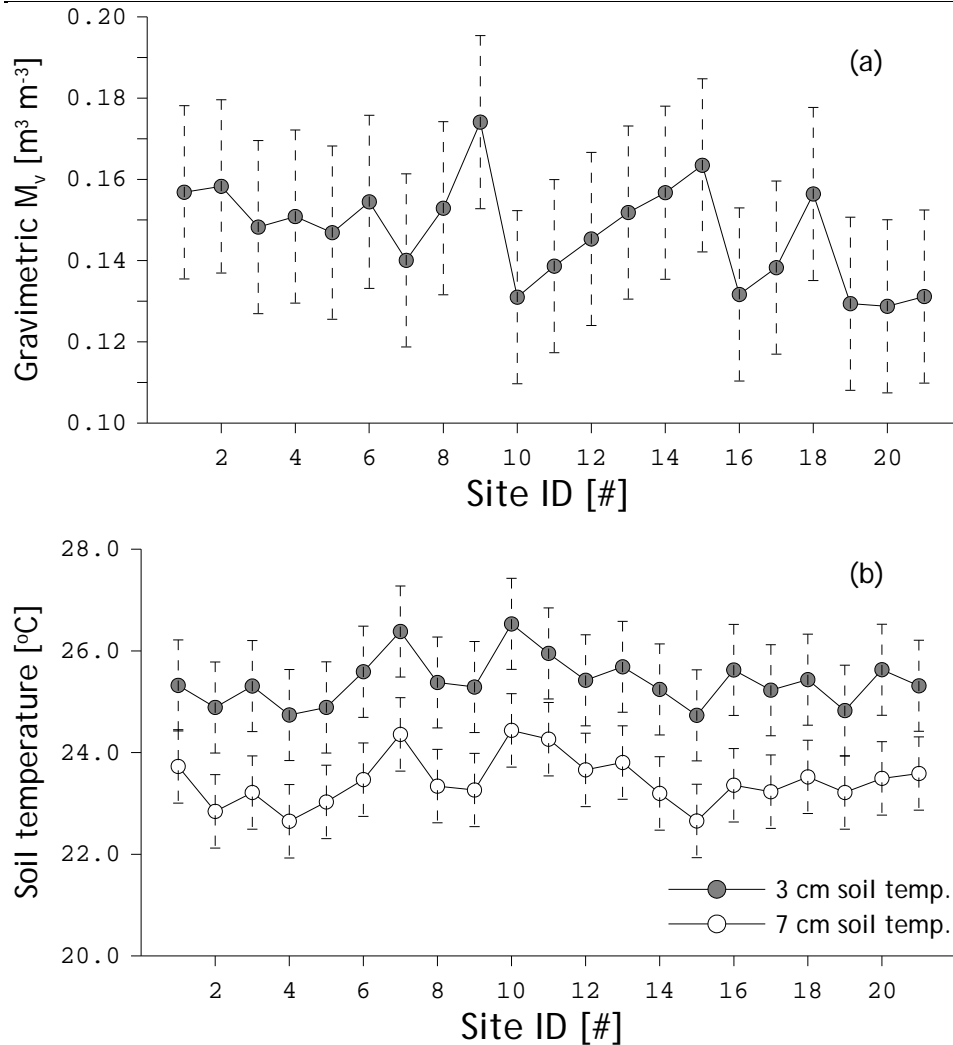


Figure 3-3: Averages of the gravimetric M_v (a) and soil temperature (b) measured during the entire campaign plotted for each sampling site separately. The site ID locations are shown in Figure 1 (R1 to R21). Error bars indicate the standard deviation in soil moisture or temperature measured throughout the campaign.

Figure 3-4a shows the development biomasses and water content of the total plant over time and Figure 3-4b illustrates the temporal evolution of the water content in individual plant components. It follows from Figure 3-4b that in the beginning of the corn growing season, the canopy was primarily made up of leaves and stems. In the middle of the growing season the stem contribution becomes more dominant and cobs' water content

increases to levels exceeding the leaf contribution. Near senescence, water content in the leaves is reduced further, whereas the contribution of the cobs to the total biomass remained constant.

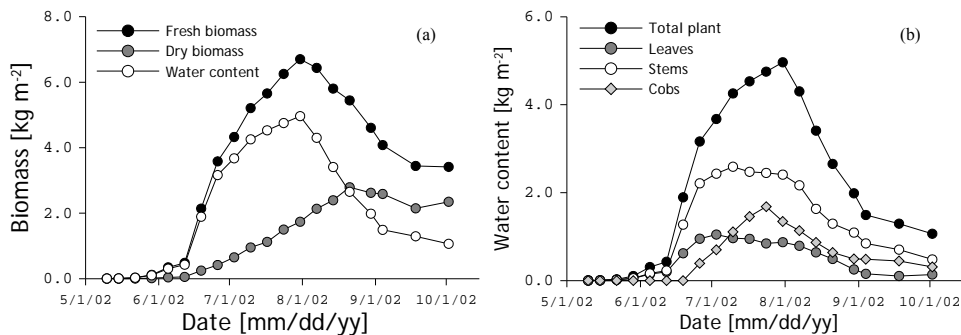


Figure 3-4 (a) Total plant water content, fresh and dry biomass plotted against time. (b) Water content in the leaves, stems and cobs plotted against time. The markers indicate the dates at which measurements were made.

Surface roughness

During the experiment surface roughness was characterized on May 25 using the grid board technique. A 2-meter long grid board was placed in the soil and photographs were taken with the soil surface in front. In total, ten surface height profiles were recorded. The surface height profile in these pictures was digitized at a 0.5-cm interval, from which two roughness parameters were derived: root the *rms* height and the correlation length (*L*). The averaged *rms* height and *L* for the ten observed surface roughness profiles were found to be 1.62 and 12.66 cm, respectively. Figure 3-5 shows an example of a photograph taken for this roughness characterization and lists the roughness parameters calculated from the digitized surface height profiles.

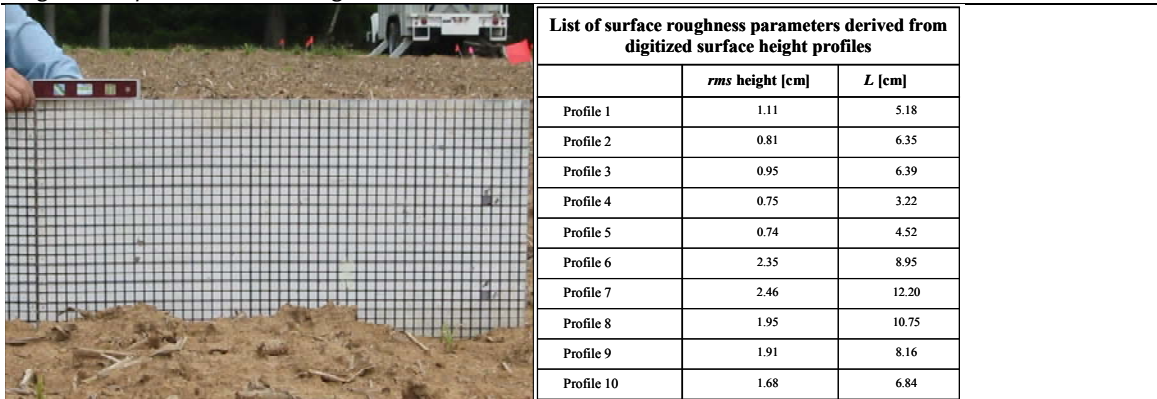


Figure 3-5: The left panel shows an example of a picture taken for surface roughness characterization and the right panel lists the derived surface roughness parameters.

Radiometer

The deployed radiometer was a dual-polarized (horizontal (H) and vertical (V)) L-band passive microwave sensor, called LRAD. The instrument was mounted on a portable 18 m tower and was designed to collect data automatically (for this experiment every hour) at five incidence angles (25, 35, 45, 55, and 60 degrees) and three azimuth angles over a range of 40 degrees. LRAD had a 3 dB beam width of approximately 12 degrees, which corresponds to footprints varying from 4.5 to 15.5 meters for the 25 to 60 degrees incidence angle range. Mechanical difficulties with the scanning system restricted the LRAD data collection, and produced considerable gaps in the season-long record. Nevertheless, ten days of complete record (ground measurements and radiometer observations) were available for the present analysis.

Each LRAD data run consisted of a pre-calibration, a measuring sequence, and a post-calibration. During each of the two calibration periods one microwave observation was acquired from a microwave absorber target of known temperature (hot target) and one

microwave observation was acquired of the sky (cold target), which has at L band an T_B of ~ 5 K (3 K cosmic background radiation and 2 K atmospheric contribution). These two so-called “hot” and “sky” target observations can be used to calibrate, through linear interpolation, the radiometer observations of the land surface using,

$$T_B^p = \frac{T_{hot} - T_{sky}}{U_{hot} - U_{sky}} U_p + T_{sky} - \frac{T_{hot} - T_{sky}}{U_{hot} - U_{sky}} U_{sky} \quad (3.10)$$

where T_B is the brightness temperature [K], T indicates the temperature [K] of the specified target and U represents the LRAD voltage observations [Volt] with subscripts *hot* and *sky* indicating the hot and *sky* target properties and superscript p pointing towards the polarization dependence of the brightness temperature, which is either horizontal (H) or vertical (V).

For processing the LRAD measurements to T_B 's the pre-calibration was used, while the post-calibration was only employed to detect anomalous values. The estimated uncertainty of the calibrated H-polarized T_B is about ± 1.0 K. While measurements were also collected for vertical polarization, there remain some unresolved issues with respect to the calibration of these measurements. Thus, vertical polarization measurements are not being presented at this time.

3.4 Results

Surface roughness parameter estimation based on H-polarized observations

Within the model of Wang and Choudhury (1981), the effects of the surface roughness is characterized by two variables: 1) modification of the reflectance (h parameter), and 2) redistribution of the H- and V-polarized emitted radiation (Q parameter). Since the data set under investigation currently includes only calibrated H-polarized T_B measurements, the Q parameter is omitted (i.e., $Q = 0$), which essentially reduces the surface emission algorithm to the one proposed by Choudhury et al. (1979). This formulation has been adopted previously in several other studies [i.e. Drusch et al. (2004), Bindlish et al. (2003)]. Based on this assumption, the h parameter can be estimated from H-polarized T_B 's measured over bare soil using,

$$\left[1 - \frac{T_B^H}{T_s} \right] = [R^H(\theta)] \exp(-h) \quad (3.11)$$

where, T_B^H is the H-polarized brightness temperature, T_s is the soil temperature, R^H is the H- polarized Fresnel reflectivity.

For the OPE³ campaign, the LRAD observations started on May 22, when corn crops had just emerged and the total fresh biomass was less than 0.04 kg m⁻². The T_B 's measured under these low biomass conditions (May 22) were used to estimate the h parameter. Unfortunately, due to mechanical difficulties with the LRAD scanning system, only microwave observations for viewing angles of 35, 45 and 60 degrees were

available for this part of the experiment. The twenty-one 3 cm surface temperature measurements taken around the radiometer footprint are averaged and are adopted as T_s .

The resulting h parameter values are given in Table 3-1.

Table 3-1: Surface parameters obtained through inversion of H-polarized TB observations acquired over bare soil conditions.

	<i>View angle</i>		
	<i>35 degrees</i>	<i>45 degrees</i>	<i>60 degrees</i>
<i>h</i>	0.300	0.238	0.172
<i>h·sec θ</i>	0.366	0.336	0.344

The derived h parameters fall within the range that has been reported previously. Wang et al. (1983)] reported a 0.00-0.53 h parameter range for surfaces with a *rms* height varying from 0.21 to 2.55 cm for a similar setting. Considering an averaged *rms* height of 1.62 cm was observed around the radiometer footprint, the h parameter values obtained from the LRAD observations appears reasonable.

An interesting observation is, however, the angular dependence of the h parameter. Over a view angle range from 35 to 60 degrees, the h parameter decreases from 0.300 to 0.172. A angular dependence is partly expected because when a radiometer observes the land surface at different angles surface roughness may have a different impact on the surface emission, while recognizing that Eq. (3.10) is also an approximation [Choudhury et al. (1979)]. However, the angular dependence of the h parameter could also be a result from the assumption of $Q = 0$. The Fresnel reflectivities for the H- and V-polarization are both a function of the incidence angle; excluding one of the two polarization components,

as is done by assuming $Q = 0$ in Eq.(3.3), induces an angular dependence of the h parameter.

Surface roughness parameter estimation based on dual-polarized T_B

The surface roughness parameter h from the present data set demonstrates an angular dependence that is equal to adopting $G(\theta) = \sec \theta$ (see Table 3-1). A limitation of the present data set is that only H-polarized T_B observations are available to some degree of confidence. Therefore, in order to retrieve the h parameter from these T_B values, Q was taken equal to zero, which might alter the angular dependency (mixing of polarization). To elaborate on these findings, dual polarized L-band (~1.4 GHz) radiometer data sets collected over bare soils within the general area of the present study [Wang et al. (1983)] are utilized to invert h and Q simultaneously.

The methodology used to retrieve the Q and h parameters has been adopted from Wang and Choudhury (1981), which is based upon the following two relationships,

$$X(\theta) = \frac{T_{NB}^V(\theta) - T_{NB}^H(\theta)}{1 - \frac{1}{2}[T_{NB}^V(\theta) + T_{NB}^H(\theta)]} = 2 \left[\frac{R^H(\theta) - R^V(\theta)}{R^H(\theta) + R^V(\theta)} \right] (1 - 2Q) \quad (3.11a)$$

$$Y(\theta) = 1 - \frac{1}{2}[T_{NB}^V(\theta) + T_{NB}^H(\theta)] = \frac{1}{2}[R^H(\theta) + R^V(\theta)] \exp(-hG(\theta)) \quad (3.11b)$$

where T_{NB}^p is the normalized brightness temperature for polarization p, according to T_B^p / T_s , $X(\theta)$ is the surface roughness coefficient for deriving the Q parameter, $Y(\theta)$ is

the surface roughness coefficient for deriving the h parameter, Eq. (3.11) and (3.12) can

be rewritten to give the Q and h explicitly resulting in,

$$Q = \left[1 - \frac{X(\theta)}{2[P(\theta)]} \right] / 2 \quad (3.13a)$$

$$P(\theta) = \left[\frac{R^H(\theta) - R^V(\theta)}{R^H(\theta) + R^V(\theta)} \right] \quad (3.13b)$$

with

$$h = - \frac{\ln \left[\frac{2Y(\theta)}{[R^H(\theta) + R^V(\theta)]} \right]}{G(\theta)} \quad (3.14)$$

The data set described in Wang et al. (1983) includes ground measurements of soil moisture and temperature observed at various depths: 0-0.5, 2.5-5.0, 5.0-10.0 cm for soil moisture and 1.25, 2.5, 7.5 and 15.0 cm for soil temperature. In addition, dual-polarized T_B observations were collected at view angles of 10, 20, 30, 40, 50, 60 and 70 degrees. These measurements have been collected over soil surfaces with different roughness characteristics. For this investigation, a smooth and a rough surface are included in the analysis with a measured *rms* height of 0.73 and 2.45 cm, respectively. Because the present data set includes radiometer observations for an incidence angle range between 35 and 60 degrees, only the T_B measured over the 20 to 60 degrees incidence angle range are utilized from the Wang et al. (1983).

Angular dependence of roughness effects

The extensiveness of the radiometer and ground measurements permits all unknowns in Eq. (3.13) and (3.14) to be derived, and allows the computation of surface roughness parameters Q and h . In analogy with the previous roughness computations, the soil moisture content integrated over 0-5.0 cm has been used to compute the relative dielectric constant and the soil temperature at 2.5 cm has been used to derive the normalized brightness temperature. The resulting h parameters are plotted as a function of the incidence angle for the rough and smooth bare soil surface in Figures 3-7a and 3-7b respectively, whereas the computed Q values are shown as a function of the incidence angle for both the rough and smooth surface in Figure 3-7c. The h -parameters shown in Figure 3-7a and 3-7b have been computed assuming three different $G(\theta)$ relationships, which are: $\cos^2 \theta$, $\cos \theta$, and $G(\theta) = 1.0$.

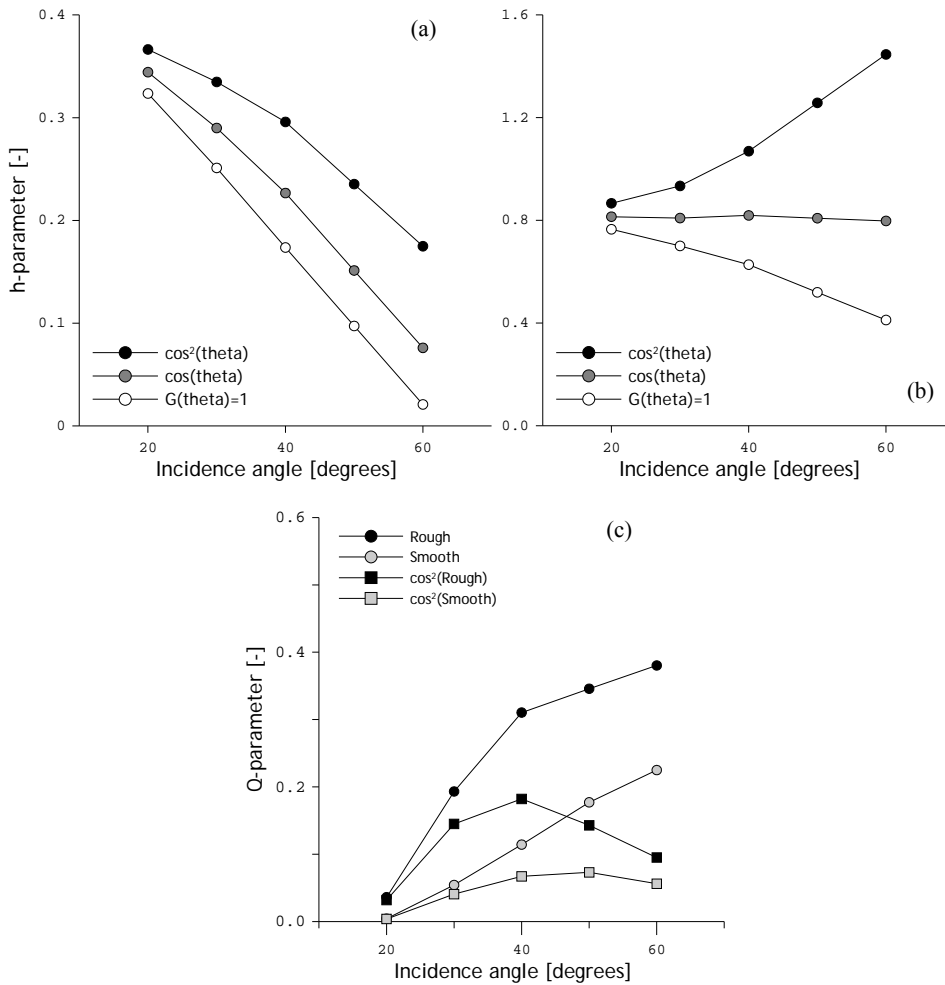


Figure 3-7: h-parameter as a function of incidence angle calculated from dual-polarized L-band T_B 's measured over (a) smooth bare soil surface and (b) rough bare soil surface. (c) Q-parameters as a function of the incidence angle for same smooth and rough surfaces.

Figures 3-7a and 3-7b show a different angular behavior of the emission measured over the rough and the smooth surface. For the rough surface, it is observed that the function $G(\theta) = \cos \theta$ results in angular independent h parameter. However, $G(\theta)$ functions are not able to suppress the angular dependence of the h parameter from the smooth surface, while $G(\theta) = \cos^2 \theta$ provides the best approximation. An angular dependency of Q

parameter is noted in Figure 3-7c for both the rough and smooth surface. As shown in Figure 3-7c, the response of Q to incidence angle is, however, reasonably well approximated by

$$Q = Q(\theta) \cos^2(\theta) \quad (3.15)$$

During the OPE³ campaign an average *rms* height of 1.62 cm was measured. As such, the roughness conditions can be considered as rougher than smooth surface, and as smoother than the rough surface of the Wang et al. (1983) data set. Given that V-polarized component of surface reflectivity cannot be included in the h parameter retrieval from the present data set, the obtained function $G(\theta) = \cos \theta$ is assumed to be in agreement with the results obtained from the data set collected at OPE³ in 2002. In addition, Q value of 0.1, being the average value of the Q derived for the rough and smooth surface, is utilized in combination with Eq. (3.15) to quantify depolarizing effects surface roughness. Then, using these extrapolated parameterizations, the h parameter is inverted from the H-polarized T_B measurements on May 22.

The resulting h parameters are given in Table 3-2, which range from 0.165 to 0.171 and display, thus, no angular dependency. This illustrates that incorporation of V-polarized reflectivity (and $Q \neq 0.0$) is required for the h parameters to be valid over all incidence angles, which will be particularly important for retrieving soil moisture from the multi-angular data as is acquired by SMOS and will be the case for Aquarius. These values for the h parameter are used for the analysis of the H-polarized transmissivity.

Table 3-2: Surface parameters obtained through inversion of H-polarized T_B observations acquired over bare soil conditions with implementation of the Q parameter extrapolated from the Wang et al. [23] data set

	<i>View angle</i>		
	<i>35 degrees</i>	<i>45 degrees</i>	<i>60 degrees</i>
<i>h</i>	0.165	0.171	0.165

Estimation of the H-polarized transmissivity

When soil moisture and surface temperature are known, H-polarized transmissivity (γ_h) can be retrieved by assuming that temporal changes in the roughness parameterization are small and the single scattering albedo can be neglected. The γ_h is estimated for days, for which soil moisture, soil temperature measurements and radiometer observations are available. For this determination, the measured soil moisture is converted into the dielectric constant using the soil textural properties given in section 3.1 and the dielectric mixing model by Dobson et al. (1985). The measured soil temperature observed at a depth of 3-cm is used to correct the T_B observations for the changes in temperature of the soil-vegetation medium. Using this parameterization, the γ_h is computed using Eq. (3.1) for incidence angles of 35, 45 and 60 degrees.

Table 3-3: H-polarized transmissivities and b parameters estimated over the 2002 corn growth cycle using multi angular brightness temperatures.

Date	W <i>kg m⁻²</i>	transmissivity			b parameter		
		35°	45°	65°	35°	45°	65°
May 29, 2002	0.1	0.919	0.936	0.958	0.675	0.455	0.211
June 5, 2002	0.3	0.813	0.840	0.868	0.554	0.401	0.230
June 19, 2002	1.9	0.803	0.844	0.800	0.095	0.063	0.059
June 26, 2002	3.1	0.782	0.788	0.741	0.063	0.053	0.047
July 3, 2002	3.7	0.807	0.803	0.743	0.039	0.037	0.037
July 9, 2002	4.2	0.763	0.739	0.711	0.055	0.053	0.041
July 12, 2002	4.3	0.793	0.757	0.726	0.045	0.046	0.037
August 21, 2002	2.6	0.840	0.812	0.763	0.055	0.056	0.051
August 30, 2002	2.0	0.838	0.835	0.795	0.073	0.069	0.058

The resulting γ_h are given for each day and for each of the three viewing angles in Table 3-3 and are plotted in Figure 3-8a against the W along with expected γ_h based on reported b parameter of $0.125 \text{ m}^2 \text{ kg}^{-1}$. In addition, the LRAD b parameters are plotted against W in Figure 8b. Most b parameter values have been derived for dense corn canopies near peak biomass. Therefore, the comparison of b parameters derived for May 29 and June 5 ($W = 0.1$ and 0.3 kg m^{-2}) is not optimal. Since previous studies [e.g Jackson and Schmugge (1991)] have reported comparable b parameter for W range $1.2 - 6.0 \text{ kg m}^{-2}$, the field conditions observed on June 19 to August 30 ($W = 1.9 - 4.3 \text{ kg m}^{-2}$) are comparable to corn canopies referred to in these previous investigations.

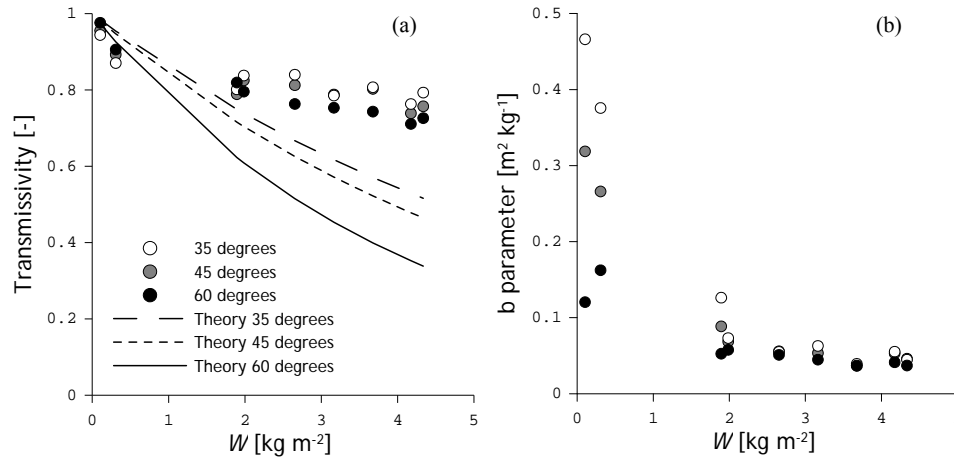


Figure 3-8: H-polarized corn transmissivities (a) and b parameters (b) inverted from LRAD T_B measured at incidence angle of 35, 45 and 60 degrees.

Figure 3-8a and 3-8b show that the LRAD γ_h follows a different pattern than is expected based on the literature reported b parameters. In the beginning of the corn growing season the γ_h is lower than expected, while closer to peak biomass the γ_h is larger. In terms of the b parameter, the results are much higher after the corn crops have just emerged and somewhat lower values at high W ($> 1.9 \text{ kg m}^{-2}$). However, because at the beginning of the growing season the corn crops were small, the uncertainties in the W measurement can result in rather large deviations between the LRAD retrievals and literature reports. In addition, the contribution of the vegetation emission to the measured T_B is also small and, therefore, uncertainties in the T_B measurements (for example, stability of the instrument) can also be a cause for the obtained differences with the literature.

Table 3-4: H-polarized transmissivities and b parameters inverted from LRAD T_B measured on May 29, 2002 perturbed by ± 1.0 K.

Date	transmissivity			b parameter		
	35°	45°	65°	35°	45°	65°
$T_B - 1.0$ K	0.936	0.948	0.970	0.537	0.371	0.147
T_B	0.944	0.955	0.976	0.466	0.319	0.120
$T_B + 1.0$ K	0.952	0.963	0.980	0.396	0.266	0.102

To illustrate the impact of the T_B uncertainties on the derived b parameter under low biomass conditions, the γ_h on May 29 has also been computed by perturbing the LRAD T_B with ± 1.0 K. The obtained γ_h and b parameters are given in Table 3-4, which show that under low biomass conditions the sensitivity of the b parameter to uncertainties T_B is very high. When 1.0 K is added or subtracted from the LRAD T_B observations, the computed γ_h changes only about 0.007, while this changes the computed b parameter by 0.071 to 0.027 $\text{m}^2 \text{kg}^{-1}$ depending on the incidence angle.

The high γ_h obtained from the T_B measured over more dense vegetation are most likely caused by scattering effects within the canopy, which has not been accounted for, since the $\omega = 0.0$ has initially been assumed. At low frequencies and when the canopy attenuation is small, the ω value adopted within the radiative transfer approach is negligible (Jackson and O'Neill, 1990) because the vegetation emission is small, which would justify using $\omega = 0.0$. As the biomass increases, however, the scattering within the canopy can have a significant impact on the measured T_B . In literature [Van de Griend and Wigneron (2004)], reported ω values for corn canopies range from 0.04 to 0.13 for L band.

By assuming that the b parameter for corn vegetation at the OPE³ site should be between 0.10 and 0.15 m² kg⁻¹, the ω 's are computed for the LRAD measurements made on June 26. These ω computations have been made assuming b parameters of 0.10, 0.11, 0.12, 0.13, 0.14 and 0.15 m² kg⁻¹. The resulting ω 's are given in Table 3-5, in which the numerical correlation between the b parameter and ω is demonstrated; for small b parameters, also ω is also small. Further, an angular dependency is noted among the inverted ω values. The derived values differ on average 0.025 between 35 and 45 degrees and 0.023 between 45 and 60 degrees. The angular dependence of ω is caused by the scattering within the complex canopy architecture (orientation of stems and leaves, as dielectric components of vegetation) [e.g. Lang and Sidhu (1983), Chauhan (1997)]. Despite these observations, the LRAD inverted ω 's in agreement with the parameter range documented in Van de Griend and Wigneron (2004).

Table 3-5: Single scattering albedo (ω) inverted from LRAD T_B measured on June 26, 2002 ($W = 3.1 \text{ kg m}^{-2}$) assuming a range b parameters from 0.10 to 0.15 $\text{m}^2 \text{ kg}^{-1}$.

b parameter $\text{m}^2 \text{ kg}^{-1}$	Single scattering albedo		
	35°	45°	65°
0.10	0.044	0.071	0.093
0.11	0.053	0.078	0.101
0.12	0.059	0.085	0.108
0.13	0.065	0.089	0.112
0.14	0.069	0.093	0.116
0.15	0.073	0.096	0.119

3.5 Concluding remarks

In this investigation, the H-polarized T_B 's measured by a tower mounted L-band (1.4 GHz) radiometer are used to analyze the vegetation effects on surface emission throughout the 2002 corn growth cycle. Concurrent with the radiometer measurements an extensive land surface characterization took place about once a week including soil moisture, soil temperature and vegetation biomass measurements. Over the period from May 22 to August 30, ten days with a complete record of ground and radiometer measurements are available for the present analysis that cover a vegetation water content (W) range of 0.0 to 4.3 kg m^{-2} .

The roughness parameter h , needed to correct for the effects of surface roughness, is inverted from H-polarized T_B measured early in the corn growing season over essentially an bare soil surface using the Choudhury et al. [30] surface emission algorithm assuming ($Q = 0.0$) and $G(\theta)$ equals 1.0. The h parameters inverted using this formulation displays an unusual angular dependence. Analysis of a dual-polarized L-band radiometer data set from 1981 [Wang et al. (1983)] demonstrates that the angular dependence of the h parameter in the present data set is partly caused by taking Q equal to 0.0. An alternative

set of the h parameters was computed using the Wang and Choudhury (1981) surface emission algorithm ($Q \neq 0.0$) with Q parameter estimated from the 1981 data set as input.

Based on the derived Wang and Choudhury (1981) surface roughness formulation, the H-polarized corn transmissivities (γ_h) have been retrieved using the radiative transfer equation and assuming the single scattering albedo (ω_h) to be zero. The derived γ_h 's are converted into b parameter values using the measured W . For sparse vegetation, the inverted γ_h 's and b parameters were found to be larger than expected based on literature. It is, however, shown that under low biomass conditions when the emission by vegetation is small, uncertainties in T_B and W measurements result in a particularly large b parameter uncertainty. For dense vegetation, the inverted b parameters are somewhat smaller than expected, which is attributed to scattering within the canopy that is not accounted for since ω is initially assumed to be zero. Assuming the b parameter for corn varies between 0.10 and 0.15 [$\text{m}^2 \text{kg}^{-1}$], the ω_h has been computed from LRAD T_B measurements. For this range of b parameters, a range of ω_h values is found that is in agreement with literature reports, but displays a strong angular dependence.

This study shows that the roughness parameters, h and Q , interact with each other as is also the case for the vegetation parameters, γ_h and ω_h . These interactions, together with any existing uncertainty in T_B need to be considered for estimating soil moisture. Moreover, the temporal variation observed among the computed γ_h 's suggests that the empirical parameter b could also depend on the growth stage. Analysis of additional radiometer data sets and simulations by advanced vegetation scattering models is

recommended to further improve the understanding of the behavior of the b parameters during the growth cycle.

Acknowledgements

The authors would like to acknowledge that the field campaign was financially supported through NASA and we would like to thank various students for participating in the field campaign.

4 H polarized L-band microwave emission during the corn growth cycle.

This chapter is based on:

Joseph, A.T., van der Velde, R., O'Neill, P.E., Lang, R.H., Gish, T. "Soil moisture retrieval during a corn growth cycle using L-band (1.6 GHz) radar observations", *Remote Sensing of Environment*, (in review).

4.1 Introduction

L-band radiometry is recognized as a technique with a significant potential for providing spatial and temporal soil moisture variations (e.g. Jackson 1993, Wigneron et al. 2003). As a result, satellite missions dedicated to global soil moisture monitoring have been proposed. A 2D-interferometric L-band radiometer has recently been launched onboard the European SMOS (Soil moisture and Ocean Salinity) satellite, Kerr et al. 2001, and the NASA is in preparation of a similar suite of microwave instruments as a part of the Aquarius and SMAP (Soil Moisture Active/Passive, Entekhabi et al. 2004) missions, which have anticipated launch dates in 2011 and 2014, respectively.

The reliability of soil moisture products derived from these microwave observations will depend, at least in part, on the effectiveness of accounting for vegetation and surface roughness impacts. Most retrieval algorithms utilize the radiative transfer model proposed by Mo et al. (1982), referred to as the τ - ω model, to account for the effects of vegetation and consider the surface roughness through the Wang and Choudhury (1981) model. Results from past field campaigns (e.g. Wang et al. 1990, Jackson et al. 1993, Jackson et al. 1999) have demonstrated the feasibility of obtaining reliable soil moisture maps using this modeling framework. At the same time, analysis of radiometer data sets collected at field scale assisted in further understanding the sources of microwave

emission and developing parameterizations for various land surfaces (e.g. O'Neill et al. 1984, Jackson and Schmugge 1991, Wigneron et al. 1995, Wigneron et al. 2001).

In recent years, however, the prospect of satellites with a L-band radiometer led to an increased number of initiatives focused on improving emission models and soil moisture retrieval algorithms, specifically for conditions that had not been intensively monitored in the past. For example, Grant et al. (2007), Guglielmetti et al. (2007) and Kurum et al. (2009) reported recently on radiometer measurements collected over forest stands and several others studies (e.g. Hornbuckle et al. 2003, Vall-llossera et al. 2005, De Rosnay et al. 2006, Cano et al. 2010) described long term field campaigns conducted in agricultural and natural vegetated settings.

Several of these new data sets were collected using automated radiometers allowing brightness temperatures (T_B) to be measured at preset time intervals. This permits a more detailed analysis of the effects of highly time-variable land surface states on microwave emission. Saleh et al. (2006) and Hornbuckle et al. (2006) found that water intercepted by vegetation could possibly influence the microwave emission also at L-band. Escorihuela et al. (2007), Saleh et al. (2007) and Panciera et al. (2009a) reported on increasing roughness effects proportional to a soil moisture decrease previously discussed by Mo and Schmugge (1987) and Wigneron et al. (2001). Hornbuckle et al. (2003) showed that the emission from vegetated surfaces may also be sensitive to the orientation of crop rows relative to the azimuth angle. While the above effects on microwave emission are detected at field scale, their impacts at the coarse resolution of satellites require further

investigation. Not accounting for these effects may add to the increase of uncertainty in satellite-based soil moisture products. Only an improved understanding of microwave emission will make it possible to reduce such uncertainties.

This chapter contributes to the improved understanding of microwave emission from the soil-vegetation system by analyzing diurnal cycles of horizontally (H) polarized L-band emission from a corn field measured as a part of a combined active/passive microwave remote sensing campaign. The NASA/ George Washington University (GWU) truck mounted scatterometer was deployed for measuring backscatter (e.g. Joseph et al. 2008) and a new L-band radiometer, called LRAD, provided T_B 's. For the field campaign, LRAD operations were automated and programmed to collect data every hour at five incidence (25° , 35° , 45° , 55° , and 60°) and three azimuth angles. In support of these remote sensing observations an intensive ground sampling of biomass, soil moisture and temperatures took place once a week around the footprints. In addition, land surface states (e.g. temperature and soil moisture) and surface heat fluxes were measured within the same field at fixed time intervals by a micro-meteorological station and a network of soil moisture stations.

In this investigation, the τ - ω model with *in-situ* measurements as input is applied to reproduce the LRAD observed diurnal T_B cycles by optimizing its vegetation and soil surface roughness parameterizations. Three specific corn growth stages are included in this analysis, namely the periods 1) just after emergence, 2) before reaching peak biomass and 3) at senescence. The vegetation water content (W) measured during these three

periods was 0.3, 0.9-4.2 and 1.4-2.7 kg m⁻², respectively and a soil moisture range from 0.016 to 0.324 m³ m⁻³ was observed. This diversity in land surface conditions were used to study several of the effects on microwave emission discussed above under a changing vegetation cover. For example, the T_B 's measured at different azimuths was utilized to investigate the impact of canopy's azimuthal anisotropy on microwave emission. Further, the data sets from different parts of the growth cycle was studied to identify the dependence on morphological changes in the canopy and the varying soil conditions was used to analyze changes in soil surface roughness as a function of soil moisture.

4.2 From incidental to continuous measurements

The ground measurements available for analysis of the passive microwave data were collected either incidentally at fixed positions around the periphery of the footprints, or continuously at some distance. This study focuses on the investigation of diurnal L-band T_B 's cycles requiring continuous soil moisture and temperature data sets. However, the measurements collected by the automated instruments may not represent the land surface conditions at the footprint of the radiometer. On the other hand, Joseph et al. (2010a, b) and the results of Chapter 3 have shown that the spatial mean of the measurements taken around the footprint is representative. Therefore, the soil moisture and temperatures measured by the automated instruments are matched to the mean of the measurements taken around the footprint. As such, the measurements collected at fixed time intervals are corrected to represent the conditions observed at the radiometer footprints.

Soil moisture

In the case of soil moisture, each watershed is equipped with twelve stations that record data every 10 minutes using capacitance probes. The data collected in the most northern watershed can be expected to represent the conditions at the footprint. The resemblance between the soil moisture dynamics measured at the footprint and at the twelve stations is analyzed by plotting the capacitance probe data against the spatial mean of the twenty-one measurements. This analysis is supported by coefficients of linear functions fitted through the data points along with the RMSD, bias, coefficient of determination (R^2) and the number of data points listed in Table 4-1.

H polarized L-band emission during the corn growth cycle

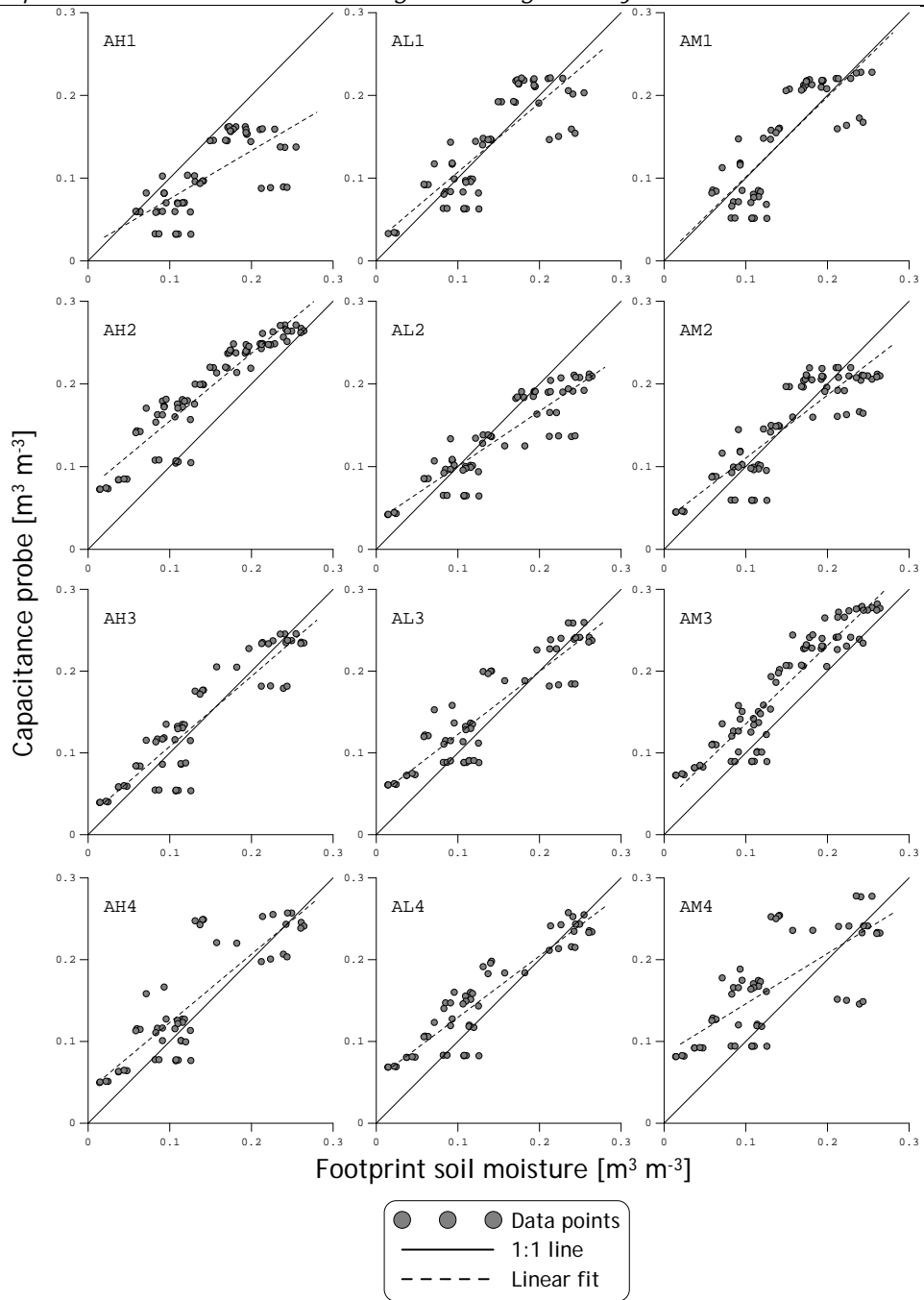


Figure 4-1: Capacitance probe soil moisture measured in the most northern watershed against the mean of twenty-one soil moisture measurements taken around the footprint (Footprint soil moisture). The station ID is given in the top left corner of each plot.

The plots of Figure 4-1 indicate positive and linear relationships between the two soil moisture data sources. The main differences consist of higher capacitance probe readings in the dry and mid soil moisture range. Such discrepancy is expected because around the footprint the moisture content of the top 0.06 m is sampled, while the capacitance probes are installed at 0.1 m depths and measure the moisture content within a 0.1 m radius. The top soil is in direct contact with the atmosphere and, thus, is subjected to a higher evaporative demand resulting in drier conditions than at a 0.1 m soil depth. In some cases, however, the capacitance probes also provided lower values than the measured around the footprint. This can be associated with the periods just after small rain events that wet the top soil, but do not include sufficient water to raise the moisture content in the deeper layers.

Table 4-1: Coefficients of linear function fitted through the soil moisture data presented in Figure 4-1 and RMSD, Bias and R² and number of data points (No).

Station ID	a -	b $m^3 m^{-3}$	RMSD $m^3 m^{-3}$	bias $m^3 m^{-3}$	R² -	No #
<i>AH1</i>	0.580	0.017	0.058	0.043	0.509	57
<i>AH2</i>	0.788	0.079	0.053	-0.054	0.850	74
<i>AH3</i>	0.857	0.022	0.031	0.017	0.831	58
<i>AH4</i>	0.926	0.032	0.047	0.022	0.741	55
<i>AL1</i>	0.836	0.024	0.035	0.005	0.687	60
<i>AL2</i>	0.664	0.034	0.036	0.011	0.794	66
<i>AL3</i>	0.769	0.046	0.036	-0.016	0.810	58
<i>AL4</i>	0.752	0.054	0.037	0.003	0.849	55
<i>AM1</i>	0.968	0.005	0.037	-0.000	0.665	57
<i>AM2</i>	0.761	0.034	0.032	-0.051	0.754	74
<i>AM3</i>	0.959	0.039	0.041	-0.033	0.874	74
<i>AM4</i>	0.615	0.084	0.061	-0.016	0.545	55

Despite these inherent differences, fairly high correlations are found between the footprint soil moisture and the measurements from the stations AH2, AH3, AL3, AM3, and AL4. It is noted that the smallest scatter among the data points is obtained using the measurements collected at station AM3 and that the line fitted through these data points is also close to unity. Therefore, the measurements from this station (AM3) were adopted to establish the soil moisture time series representative for the radiometer footprints. A linear function with its coefficients given in Table 4-1 is used to match the soil moisture measured at station AM3 to the dynamics monitored around the footprint resulting in RMSD of $0.025 m^3 m^{-3}$, which is comparable to calibration uncertainty of the Theta probe measurements. The time series of the corrected and original AM3 measurements along with the footprint soil moisture and daily rainfall is shown in Figure 4-2.

Temperature

Soil and infrared temperatures of the surface are available at the micro-meteorological station. The soil temperatures were measured by six pairs of thermocouples buried at depths of 0.02 and 0.06 m wired to a single channel. These temperatures can be considered as an average over these two depths and were used as a proxy for the footprint soil temperature. Similarly, the temperatures measured by infrared radiometers can be used as proxy for the canopy temperature.

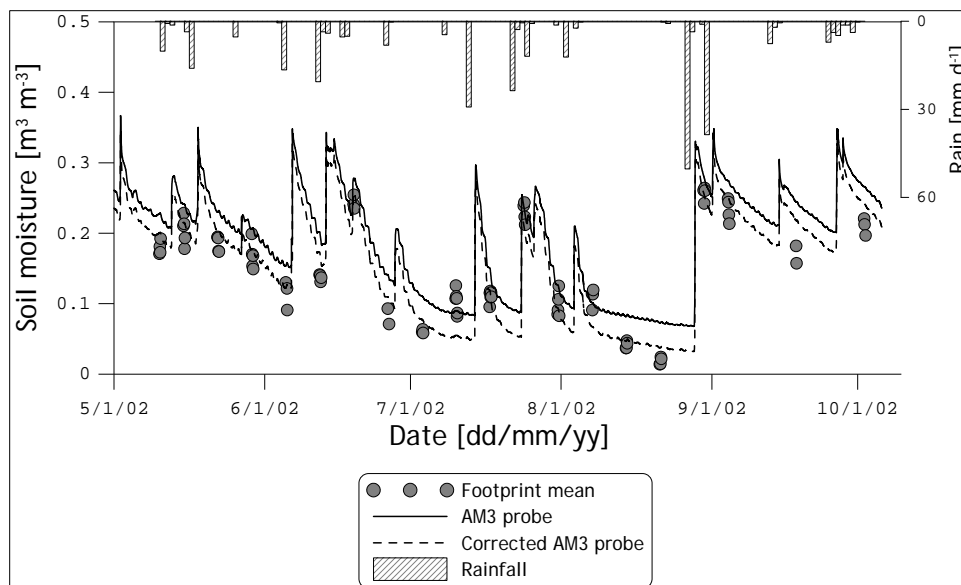


Figure 4-2: Time series of the corrected and the original soil moisture measurements collected at the AM3 station along with the footprint soil moisture and antecedent precipitation.

To identify the relationship between the thermodynamics at the two locations, the data collected by thermocouples and infrared radiometer are plotted against the measurements taken around the LRAD's footprints, as shown in Figure 2-9. The top of Figure 4-3 shows the temperature measured by each pair of two thermocouples plotted against the

footprint average of the mean of the 0.03- and 0.07-m soil temperatures. The bottom of Figure 4-3 presents the two infrared temperatures against the mean of the footprint canopy temperatures. Statistics related to the comparison are given in Table 4-2.

Table 4-2: Same as Table 4-1, except the regression coefficients and statistical variables are presented for the temperature data in Figure 4-3.

Station ID	a -	b K	RMSD K	bias K	R² -	No #
<i>TC-1</i>	0.909	5.033	4.66	-2.68	0.69	92
<i>TC-2</i>	0.960	5.785	6.88	-4.66	0.58	
<i>TC-3</i>	0.991	4.828	6.73	-4.47	0.60	
<i>TC-4</i>	0.929	4.855	4.94	-2.99	0.69	
<i>TC-5</i>	1.009	4.415	6.64	-4.52	0.63	
<i>TC-6</i>	0.981	4.171	5.56	-3.59	0.68	
<i>IR-east</i>	0.919	4.301	4.61	-2.25	0.63	93
<i>IR-west</i>	0.863	5.533	4.41	-1.92	0.63	

Both Figure 4-3 and Table 4-2 indicate that the temperatures measured by the *TC-1* and *IR-west* sensors at the station represent respectively the soil and canopy temperatures at LRAD's footprints best. Hence, the data sets collected by these two instruments are matched to the footprint dynamics using the linear functions define by the coefficients given in Table 4-2 resulting in a RMSD's of 2.14 and 2.58 K, respectively.

In the following, the corrected *TC-1* and *IR-west* temperature are adopted as the soil and canopy temperatures, respectively. However, it is widely recognized that L-band emission can originate from deeper within the soil profile (+/- 0.5-1.0 m, Choudhury et al. 1982), while the *TC-1* data is fitted to averaged of 0.03- and 0.07-m temperature. Unfortunately, temperatures measured at deeper depths are not available at this site. The uncertainty introduced by this assumption is expected to not exceed the other error sources.

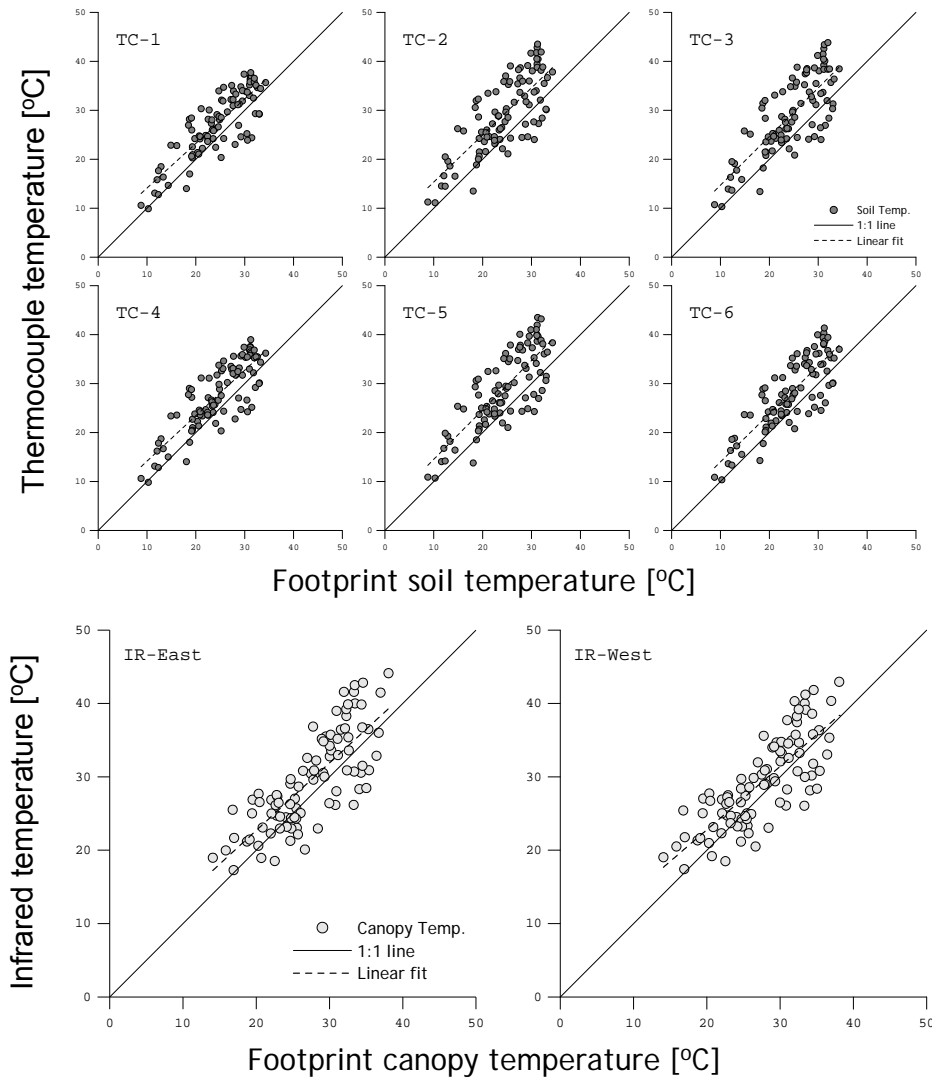


Figure 4-3: (Top panel) thermocouple temperature plotted against the footprint average of the mean of the 0.03 and 0.07 m soil temperature, (bottom panel) thermal infrared temperature at the micro-meteorological station against the mean canopy temperature measured around LRAD's footprint.

4.3 τ - ω model application and parameter estimations

τ - ω model application

The semi-empirical τ - ω model developed by Mo et al. (1982), and also described in Chapters 2 and 3, has been applied to reproduce the H polarized L-band emission measured from the corn field. Assuming that the contribution from the atmosphere is negligible, the τ - ω model defines H polarized T_B as,

$$T_B^H = (1 - R_s^H) \gamma_H T_s + (1 + R_s^H \gamma_H) (1 - \gamma_H) (1 - \omega_H) T_c \quad (4.1)$$

where, R_s is the soil surface reflectivity (= 1- soil surface emissivity, e_s) computed using the model by Wang and Choudhury (1981), γ is the transmissivity, ω is the single scattering albedo, T_s and T_c are respectively the soil and canopy temperatures (K), and sub- and superscript H indicates that the variable is representative for the H polarization.

The vegetation effects within the τ - ω model are accounted for by the γ and ω . The first quantifies the amount of soil emission passing through the canopy and the emission by the canopy itself. The latter parameterizes the fraction of emission scattered within the canopy. As shown in Chapter 2, the γ is calculated as a function of the optical depth (τ) following,

$$\gamma = \exp(-\tau/\cos \theta) \quad (4.3)$$

whereby the τ is often specified as linear function of an empirical parameter, b , and vegetation water content (W) as follows,

$$\tau = b \cdot W \quad (4.6)$$

Wigneron et al. (1995) among others have shown that the τ at a field scale may also depend on the incidence angle, specifically for vertically structured canopies such as wheat and corn. Therefore, in several cases, such as the L-MEB model (Wigneron et al. 2007) for the SMOS soil moisture retrievals, the τ is defined through a simple formulation based on the τ at nadir (τ_{NAD}) and a fitting parameter,

$$\tau_H(\theta) = \tau_{\text{NAD}} (\sin^2(\theta) \cdot tt_H + \cos^2(\theta)) \quad (4.4)$$

$$\tau_V(\theta) = \tau_{\text{NAD}} (\sin^2(\theta) \cdot tt_V + \cos^2(\theta)) \quad (4.5)$$

where, tt_H and tt_V are empirical parameters quantifying angular dependence of τ at the H and V polarization, respectively.

Application of the τ - ω model for simulating T_B 's requires temperatures of the canopy (T_c) and emitting soil layer (T_s) as well as the soil moisture content. The temperatures measured by the infrared thermometer and buried thermocouples, and the soil moisture recorded by the AM3 probe, corrected to represent the footprint dynamics, have been adopted as T_c , T_s and soil moisture data sources, respectively.

Parameter estimation

Next to these land surface states, the T_B simulations depend also on a number of roughness and vegetation parameters, which should ideally be reduced to a minimum for retrieval purposes. For example, the bare soil emission model utilizes the parameters h_r , Q and N_R . A much debated part in this formulation is the angular dependence of the roughness effect. Originally, Wang and Choudhury (1981) took N_R equal to 2.0, while others (e.g. Wang et al. 1983, Wegmüller and Mätzler 1999) suggested that lower values are more appropriate. Recently, Escorihuela et al. (2007) found that N_R attains also different values for the H and V polarization. Hence, the N_R is considered as a polarization dependent parameter. Recognizing that both the H and V polarized R_0 vary with the incidence and that polarization mixing is limited at L-band (e.g. Mo and Schmugge 1987, Wigneron et al. 2001), Q is assumed zero as its effect on surface emission can be compensated by N_{RH} .

Also, the impact of the parameters τ (or b) and ω is not independent within T_B simulations performed using the τ - ω model (e.g. Burke et al. 1999, Joseph et al. 2010b). The ω is, therefore, taken equal to zero, which is justified based on previous research (e.g. Wigneron et al. 2004) showing that the effect of scattering within the canopy is at L-band negligible for most vegetation covers. Nevertheless, the values of ω derived from inversion of selected measurement days are given.

These simplifications reduce the unknowns to h_r and N_{RH} for the soil surface roughness, and to b and tt_H for the vegetation. The roughness parameters are estimated by

minimizing the RMSD between T_B 's simulated and measured at the beginning of the campaign under nearly bare soil conditions ($W < 0.1 \text{ kg m}^{-2}$) using a least squares optimization algorithm. The obtained h_r and N_{RH} are respectively 0.579 and 0.214 with a RMSD of 2.67 K computed using the T_B 's measured at all azimuth and incidence angles for the three *bare soil* periods. This parameterization is assumed to be temporally stable, which is justified based on the investigation by Joseph et al. (2010a). They found that the roughness estimated at the start of this campaign is representative for the entire observation period.

With roughness parameterized and assumed constant, the τ_{NAD} , computed as the product of the W and the empirical b parameter, remains the only variable throughout the growing season, whereby measurements are used for W . Although the b parameter is intended to be a constant defined for a specific land cover type, results from a discrete medium scattering model have shown that attenuation by canopies depend also on the vegetation morphology (Le Vine and Karam, 1996). As the architecture of corn plants changes during the growing season, the empirical constant may vary as well. Moreover, Wigneron et al. (1995) and Pardé et al. (2003, 2004) found an angular dependence for the b parameter and Hornbuckle et al. (2003) demonstrated that microwave emission is also affected by the crop row orientation.

Given the setup of our field campaign, the b parameters needed to reproduce the measured T_B cycles may, thus, depend on the growth stage, incidence and azimuth angle. In this context, the μ_H parameter could be useful in correcting for the angular

dependence. Therefore, to match the T_B simulations with hourly measurements of each episode separately, the b value is estimated assuming $tt_H = 1$ (no angular dependence), and the values of b and tt_H are estimated simultaneously. The optimum b and tt_H values are obtained by minimizing two cost functions using least squares optimization algorithm: 1) RMSD computed for the T_B 's at all azimuth and incidence angles, 2) RMSD computed for T_B 's at a specific azimuth angle. Additionally, a single b value is estimated for each azimuth and incidence angle separately, which provides the best approximation of the angular dependence.

In addition, the episodes with LRAD measurements over vegetation cover include a certain soil moisture range. As several authors (e.g. Saleh et al. 2007, Escorihuela et al. 2007, Panciera et al. 2009a) provided evidence for a linear dependence of the h_r parameter to soil moisture, a change in wetness during a measurement periods could affect the results. In analogy to these studies, the impact of changing soil moisture conditions on the effective roughness is investigated by fitting the following linear function,

$$h_r = h_1 \cdot sm + h_0 \quad (4.7)$$

where, sm is the soil moisture ($m^3 m^{-3}$).

The coefficients, h_1 and h_0 , are obtained by minimizing the RMSD computed using all T_B 's measured during sequence after the b value has been optimized for each azimuth and incidence angle, separately.

Table 4-3 lists the summary of the optimizations (six types in total) described above. The inverted b parameters are expected to quantify its dependence on the growth stage, azimuth angle (or crop row orientation) and incidence angle. Further, the estimation of the coefficients h_1 and h_0 can provide additional experimental evidence for the dependence of h_r on soil moisture. Moreover, via the RMSD's computed between the simulated and measured T_B , the relative contribution of each uncertainty source is quantified.

Table 4-3: List of calibrations used for reproducing the T_B 's measurements

	$tt_H = 1$	$tt_H \neq 1$
1	Fit a single b for all azimuth and incidence angles	Fit a single b and tt_H for all azimuth and incidence angles
2	Fit a single b for each azimuth angles	Fit a single b and tt_H for each azimuth angles
3	Fit for each incidence and azimuth angle a single b value	
4	Fit the function $h_r = h_1 sm + h_0$	

4.4 Results

The results from the six optimizations are presented for each measurement cycle in a single table, Tables 4-4 through 4-8. In these tables, the inverted b and, if applicable, tt_H parameters are given as well as the RMSD's computed between the measured and simulated T_B 's. The total RMSD is provided along with the RMSD averaged for a specific azimuth. The RMSD's following from the optimization of the h_1 and h_0 parameters are given in Table 4-9.

The match between the T_B measurements and various simulations are plotted as a time series in Figure 4-4 for June 8 (early growth stage), Figure 4-5 for July 2 (near peak biomass) and Figure 4-6 for August 29 (senescence). To limit the number of plots in

H polarized L-band emission during the corn growth cycle

these figures, the results from three incidence angles are presented, which are 25°, 45°, and 60° except for June 8. On this day, data from 25° (and 55°) was not collected and the measurements from 35° are shown instead. Also for clarity, the T_B simulations from four, instead of six, optimizations are shown, which are obtained by:

- 1) a single fitted b while assuming $tt_H = 1$;
- 2) a b and tt_H fitted for each azimuth angle;
- 3) a b fitted for each incidence and azimuth angle;
- 4) using b values from (3) with fitted h_1 and h_0 parameters;

Vegetation effects throughout the growth cycle

The plots in Figures 4-4 through 4-6 show, as expected, that discrepancies between the measured and simulated T_B 's are largest when a single b parameter is fitted for all incidence and azimuth angles. The magnitude of these deviations varies, however, among the different growth stages. This suggests not only that the b parameter depends on the incidence and azimuth angle, but also that these angular dependencies change during the growing season. Somewhat unexpected is, however, that at peak biomass T_B simulated by a single b parameter matches the measurements taken from the various incidence and azimuth angles best. This is further elaborated below. Indeed, the values presented in Tables 4-4 through 4-8 confirm the changing angular dependencies of the empirical b throughout the growing cycle. The magnitude of b also displays a seasonal trend. A b of $0.334 \text{ m}^2 \text{ kg}^{-1}$ is found at the early development of crops ($W = 0.3 \text{ kg m}^{-2}$), while near

peak biomass ($W = 4.2 \text{ kg m}^{-2}$) and senescence ($W = 2.1 \text{ kg m}^{-2}$) the b reduces to 0.053 and $0.047 \text{ m}^2 \text{ kg}^{-1}$, respectively. Considering most studies on L-band radiometry over corn reported on b parameters ranging from 0.10 to $0.15 \text{ m}^2 \text{ kg}^{-1}$ (e.g. Van de Griend and Wigneron 2004a), the values obtained at the early growth stage are much larger, and the ones near peak biomass and senescence are somewhat smaller than expected. Many of the investigations summarized by Van de Griend and Wigneron (2004a), however, analysed T_B 's measured in only a part of the growth cycle. In fact, the observed trend over the growth cycle is quite consistent with results previously reported by Wigneron et al. (2004). They also found that at the early growth stage the b attains much larger values than during the rest of the season.

Table 4-4: The b parameter and tt_H calibrated to reproduce the T_B 's measured at various combinations of incidence and azimuth angles in the period June 8th to June 10th and the RMSD's computed between the simulated and measured T_B 's.

Azimuth degrees	Incidence degrees	$tt_H = 1$		$tt_H = \text{optimized}$				Incidence b kg m ⁻²
		single b kg m ⁻²	azimuth b kg m ⁻²	single b kg m ⁻²	tt_H -	azimuth b kg m ⁻²	tt_H -	
40	25	0.334	0.376	0.569	0.308	0.474	0.671	0.431
	35							
	45							
	55							
	60							
RMSD (K)		6.77	6.39	7.18		6.26		6.18
60	25	0.334	0.319	0.569	0.308	0.562	0.326	0.412
	35							
	45							
	55							
	60							
RMSD (K)		6.89	6.86	5.99		5.94		5.94
80	25	0.334	0.264	0.569	0.308	0.648	0.095	0.450
	35							
	45							
	55							
	60							
RMSD (K)		8.23	7.71	6.43		5.55		5.55
Total RMSD (K)		7.30	6.99	6.54		5.93		5.89

Table 4-5: Same as Table 4-4, only results for the period June 24th to June 27th are presented.

<i>Azimuth</i> degrees	<i>Incidence</i> degrees	<i>tt_H = 1</i>		<i>tt_H = optimized</i>				<i>Incidence</i> <i>b</i> kg m ⁻²
		<i>single</i>	<i>azimuth</i>	<i>single</i>	<i>tt_H</i>	<i>single</i>	<i>azimuth</i>	
		<i>b</i> kg m ⁻²	<i>b</i> kg m ⁻²	<i>b</i> kg m ⁻²	<i>tt_H</i> -	<i>b</i> kg m ⁻²	<i>tt_H</i> -	
40	25							0.264
	35							0.363
	45	0.269	0.291	0.405	0.426	0.328	0.818	0.286
	55							0.304
	60							0.272
RMSD (K)		4.57	4.29	5.33		4.24		3.88
60	25							0.337
	35							0.327
	45	0.269	0.253	0.405	0.426	0.401	0.417	0.297
	55							0.236
	60							0.226
RMSD (K)		5.28	5.18	4.19		4.17		4.12
80	25							0.363
	35							0.368
	45	0.269	0.235	0.405	0.426	0.476	0.196	0.290
	55							0.220
	60							0.186
RMSD (K)		6.86	6.56	5.09		4.27		4.20
Total RMSD (K)		5.57	5.35	4.87		4.23		4.06

The lower values found here near peak biomass and at senescence are mostly explained by neglecting the effect of scattering within canopy ($\omega = 0$) for the b parameter inversion. Accounting for these scattering losses requires typically a larger b value as compensation (e.g. Burke et al. 1999, Joseph et al. 2010b). Moreover, using roughness parameters estimated at the start of the campaign poses also a larger, though unknown, uncertainty on the results obtained from the LRAD data sets collected at the end of the campaign.

Table 4-6: Same as Table 4-4, only results for the period July 2nd to July 4th are presented.

<i>Azimuth degrees</i>	<i>Incidence degrees</i>	<i>tt_H = 1</i>		<i>tt_H = optimized</i>				<i>Incidence b kg m⁻²</i>
		<i>single</i>	<i>azimuth</i>	<i>single</i>	<i>azimuth</i>	<i>single</i>	<i>azimuth</i>	
		<i>b</i> kg m ⁻²	<i>b</i> kg m ⁻²	<i>b</i> kg m ⁻²	<i>tt_H</i> -	<i>b</i> kg m ⁻²	<i>tt_H</i> -	
40	25							0.023
	35							0.047
	45	0.053	0.053	0.049	1.02	0.030	1.981	0.045
	55							0.057
	60							0.056
RMSD (K)		3.96	3.95	3.70		3.41		3.21
60	25							0.034
	35							0.049
	45	0.053	0.054	0.049	1.02	0.047	1.110	0.061
	55							0.054
	60							0.054
RMSD (K)		3.37	3.34	3.29		3.27		3.01
80	25							0.044
	35							0.066
	45	0.053	0.049	0.049	1.02	0.078	0.368	0.063
	55							0.050
	60							0.043
RMSD (K)		4.21	4.10	4.43		3.78		3.37
Total RMSD (K)		3.85	3.80	3.81		3.49		3.20

Table 4-7: Same as Table 4-4, only results for the period August 20th to August 23rd are presented.

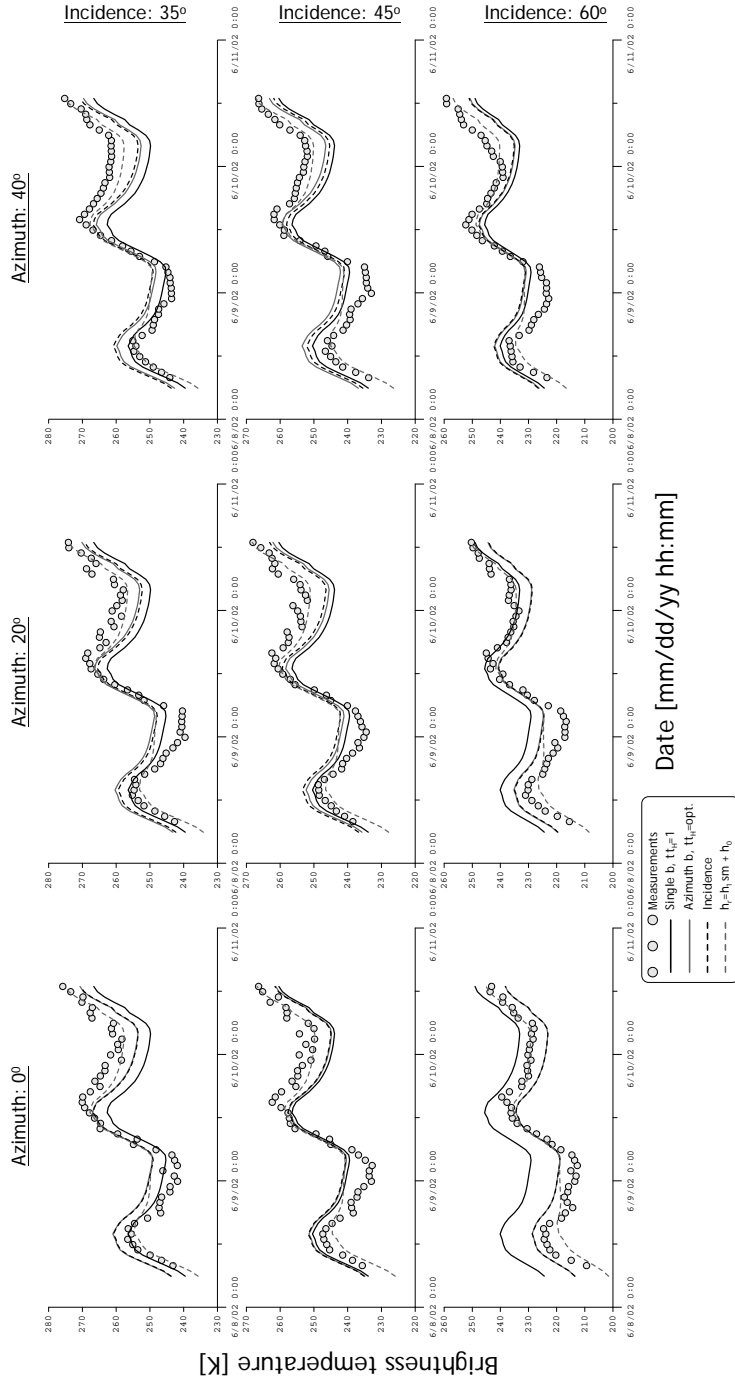
<i>Azimuth</i> degrees	<i>Incidence</i> degrees	<i>tt_H = 1</i>		<i>tt_H = optimized</i>				<i>Incidence</i> <i>b</i> kg m ⁻²
		<i>single</i> <i>b</i> kg m ⁻²	<i>azimuth</i> <i>b</i> kg m ⁻²	<i>single</i> <i>b</i> kg m ⁻²	<i>tt_H</i> -	<i>single</i> <i>b</i> kg m ⁻²	<i>azimuth</i> <i>tt_H</i> -	
40	25							-0.016
	35							0.026
	45	0.056	0.053	0.011	7.09	0.000	159.9	0.047
	55							0.055
	60							0.056
RMSD (K)		4.12	4.05	3.56		3.37		3.09
60	25							0.002
	35							0.034
	45	0.053	0.058	0.011	7.09	0.013	6.224	0.059
	55							0.062
	60							0.059
RMSD (K)		3.73	3.72	3.38		3.38		3.09
80	25							0.008
	35							0.056
	45	0.053	0.063	0.011	7.09	0.035	2.238	0.065
	55							0.068
	60							0.063
RMSD (K)		4.01	3.80	3.90		3.68		3.35
Total RMSD (K)		3.95	3.86	3.61		3.48		3.18

Table 4-8: Same as Table 4-4, only results for the period August 29th to September 1st are presented.

<i>Azimuth degrees</i>	<i>Incidence degrees</i>	<i>tt_H = 1</i>		<i>tt_H = optimized</i>				<i>Incidence b kg m⁻²</i>
		<i>single</i>	<i>azimuth</i>	<i>single</i>	<i>azimuth</i>	<i>azimuth</i>	<i>azimuth</i>	
		<i>b</i> kg m ⁻²	<i>b</i> kg m ⁻²	<i>b</i> kg m ⁻²	<i>tt_H</i> -	<i>b</i> kg m ⁻²	<i>tt_H</i> -	
40	25							0.014
	35							0.018
	45	0.047	0.036	0.008	8.030	0.001	96.38	0.026
	55							0.038
	60							0.045
RMSD (K)		6.48	5.10	4.54		2.91		2.79
60	25							0.011
	35							0.014
	45	0.047	0.051	0.008	8.030	0.000	388.0	0.046
	55							0.058
	60							0.055
RMSD (K)		6.59	6.46	4.26		3.79		3.01
80	25							0.041
	35							0.048
	45	0.047	0.053	0.008	8.030	0.043	1.375	0.054
	55							0.059
	60							0.051
RMSD (K)		3.64	3.05	5.14		2.90		2.54
Total RMSD (K)		5.57	4.87	4.65		3.20		2.78

H polarized L-band emission during the corn growth cycle

Figure 4-4: T_B simulations and measurements plotted over time for the period 8 June 8:00 to 10 June 13:00.



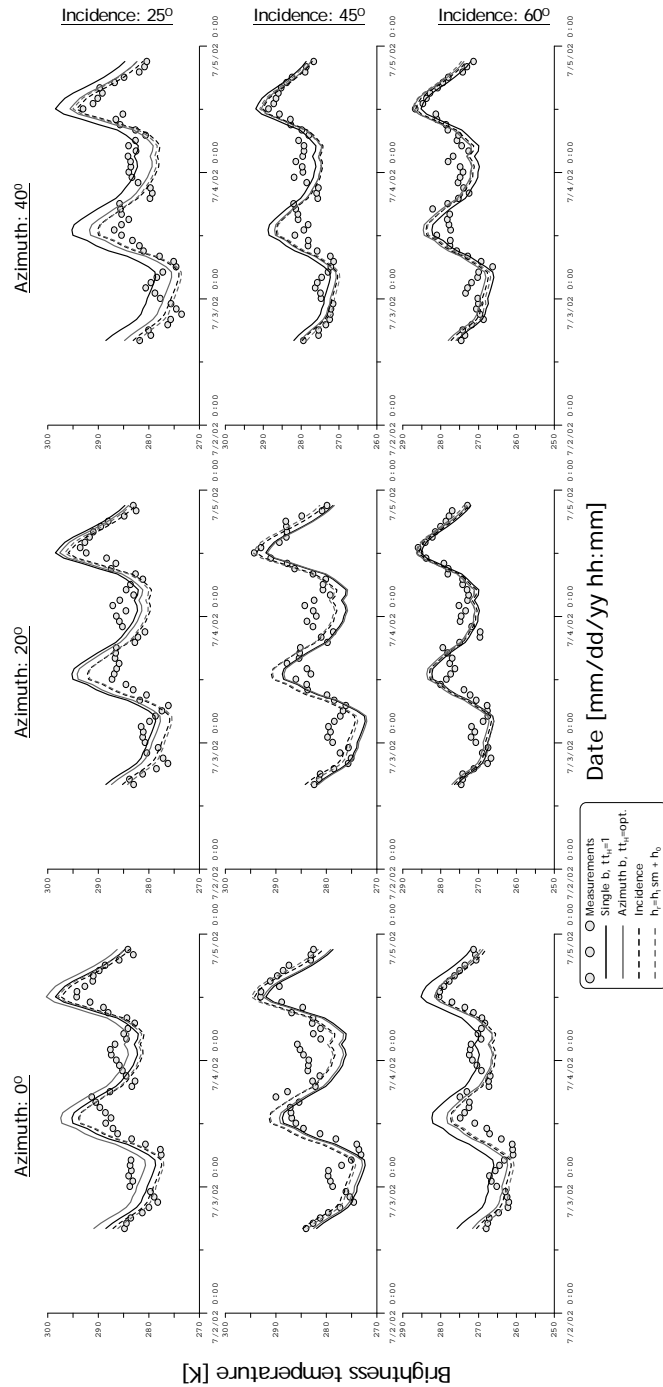


Figure 4-5: T_B simulations and measurements plotted over time for the period 2 July 16:00 to 4 June 21:00.

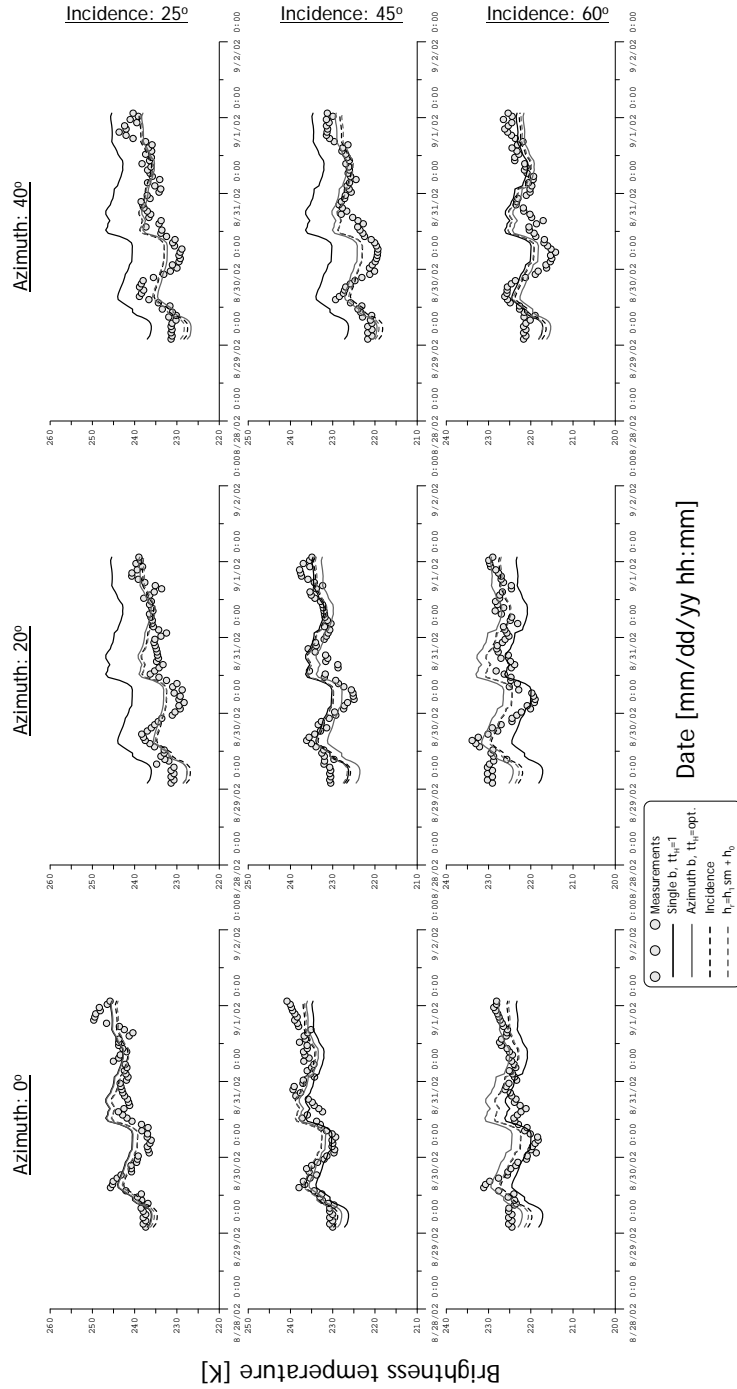


Figure 4-6: T_B simulations and measurements plotted over time for the period 29 August 0:00 to 1 September 14:00.

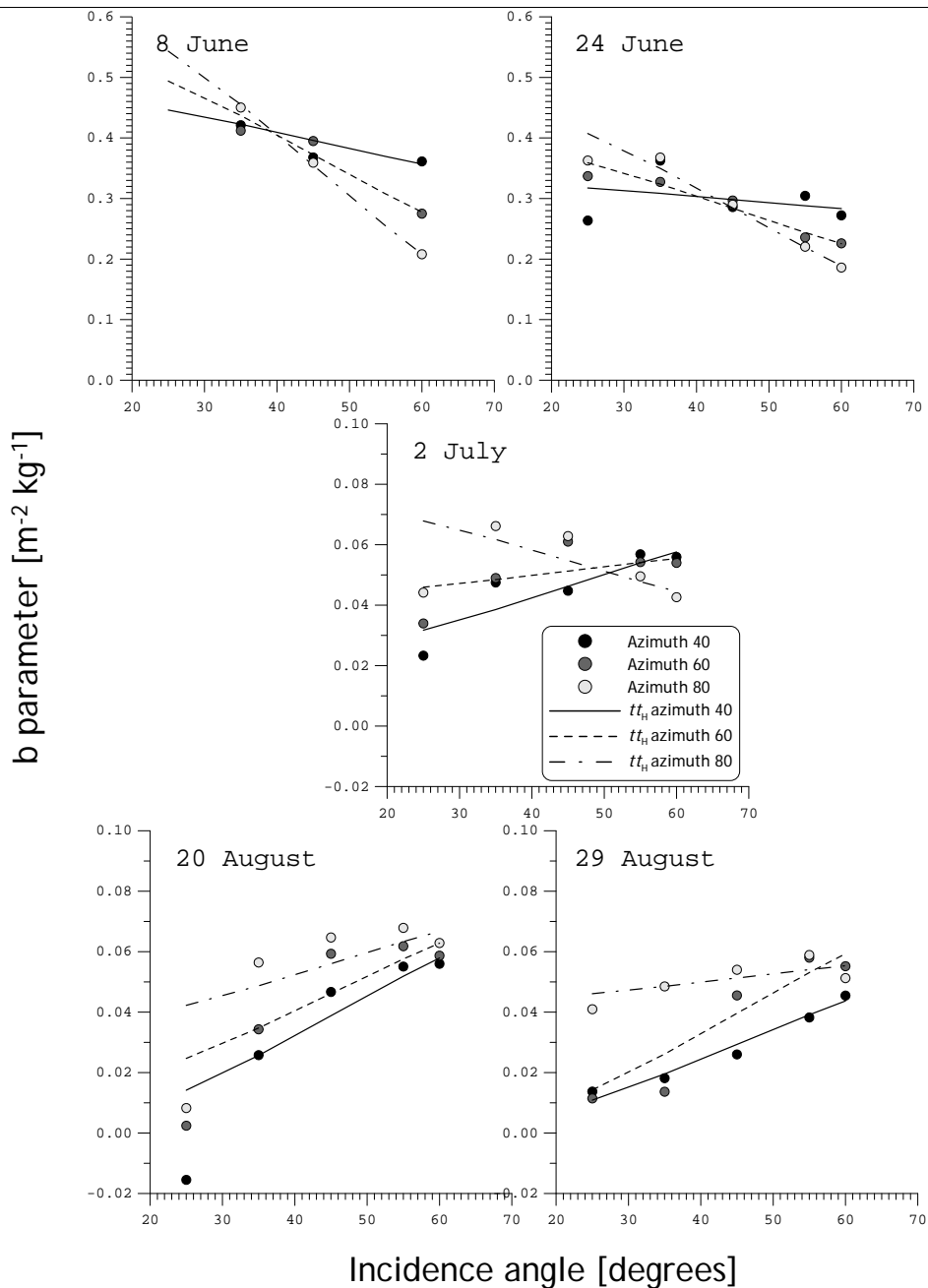


Figure 4-7: Separately fitted b values for the five measurements episodes plotted against the incidence for the three azimuth positions.

Along with the change in magnitude of the b parameter, also its angular dependence varies over the growth cycle. A more detailed analysis is provided in Figure 4-7, in which

the b values fitted for each incidence and azimuth angle separately are plotted against the incidence angle. In addition, the values produced by the b and tt_H fitted for a specific azimuth are plotted.

Figure 4-7 shows, in general, a decreasing b as a function of the incidence angle at the beginning of the season (June 8 and 24), while an increase is observed near senescence (August 20 and 29). The decrease in the early corn development is most noticeable for the view direction along the rows and less apparent when viewing further across. Near senescence, however, the opposite trend is noted. At this growth stage, the angular dependence of b is almost absent for the parallel view direction, especially if results from 25° is disregarded. Conversely, viewing only somewhat across the corn rows causes already a significant increase in the b with the incidence. On the other hand, closer to peak biomass (July 2) the angular dependence of the b for either of the azimuth positions is much weaker. This explains also why for this particular episode a good match between the measured and simulated T_B 's is obtained using a single b .

The decrease of the b parameter with the incidence angle at the beginning of the growth cycle is not quite surprising as neither model nor experimental investigations have yet provided evidence for such angular dependency. Nevertheless, the decrease of the b is consistently observed for the periods starting on both June 8th and June 24. On these dates, the canopy height was 0.6 m and 1.4 m respectively, and the corn plants consisted primarily of leaves shooting nearly vertical from the stems. Thus, the density of the vertically oriented leaves is rather high at the position of the crops, which could possibly

explain the larger b (or τ) at lower angles. O'Neill et al. (1984) showed that for L-band the contribution from leaves of a fully grown corn canopy is less important than the contribution from the stems. Thus, even a smaller effect of leaves can be expected at the early growth stage. Clustered together, however, they may exert a significant effect on the measured T_B . Since the vertically oriented crops appear denser as the path through the canopy is shorter, the value of b decreases with the incidence angle and a weaker angular dependency is observed when viewing across the rows.

The strength of this angular dependency declined as the canopy grows towards its peak biomass. A reduction in the decrease of b with the incidence angle is already noted on June 24. During this growing stage, the leaves increase in number and develop primarily in the horizontal direction forming a closed canopy. This leaf coverage has an attenuating effect on the angular dependent contributions from strong emitters, such as the stems. Hence, the dependence of the b on the incidence angle found near peak biomass (July 2) is negligible at all azimuths. Hornbuckle et al. (2003) drew similar conclusions. They found that as long as leaves contain significant amounts of water, the emission from corn is isotropic in the azimuth. During senescence, however, the foliage loses its moisture and the leaves no longer mask the contribution from the stems. For this growth stage, Hornbuckle et al. (2003) concluded that the T_B measurements are sensitive to the view direction relative to the crops rows because of the effect of the exposed stems.

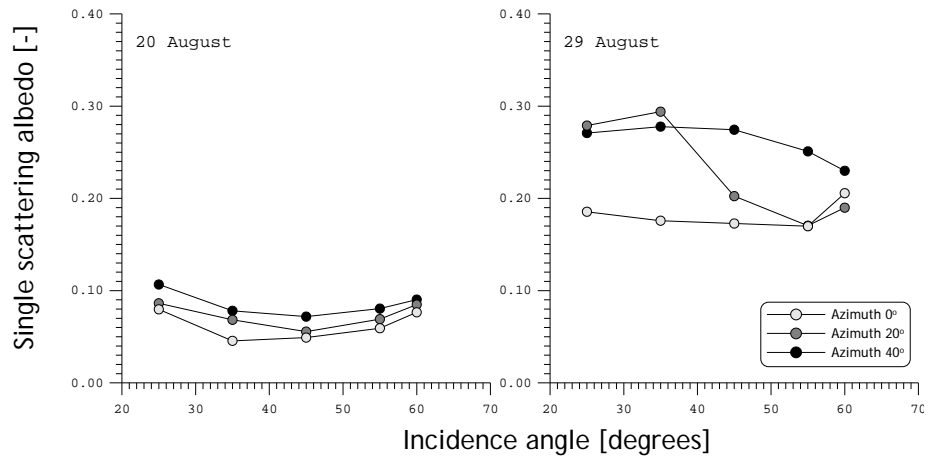


Figure 4-8: Single scattering albedos (ω 's) inverted for the measurements collected at senescence (August 20th and August 29th) assuming a b parameter of $0.115 \text{ m}^2 \text{ kg}^{-1}$.

A similar dependence of the T_B on the crop row orientation was found here. On August 20 and August 29, an increase in the b with the incidence angle is observed when viewing across the rows, while for the along row direction this dependency is negligible. During these two episodes, most of the water in the canopy resided in the stems. As such, the H polarized radiation emitted by either the vegetation or the soil surface may have scattered within the canopy composed of primarily the vertically oriented stems. These scattering effects are larger in the across row direction as the stems' scattering cross section will be larger.

For inversion of the b parameters, however, scattering within the canopy were not considered since the ω is assumed to be zero. To evaluate the effect of this assumption, the ω 's were inverted for August 20 and August 29 assuming an angular independent b of $0.115 \text{ m}^2 \text{ kg}^{-1}$ adopted from Jackson and O'Neill (1990). Figure 4-8 shows the obtained ω 's plotted against the incidence angle for the three azimuth angle. Indeed, the plots show that the ω estimates were considerably above zero for both periods. On average

values of 0.073 and 0.223 are found for August 20 and 29, respectively. This large difference between the two dates was explained by the strong decrease in leaf moisture. On August 21, a leaf water content of 0.8 kg m^{-2} was measured, which reduces to 0.3 kg m^{-2} on August 31 and became almost negligible (0.05 kg m^{-2}) on September 4. Over this period, thus, the effect of the stems gradually increased as the attenuation by the leaves further decreased. Another important observation from Figure 4-8 is that the ω estimated for both periods is larger in the across than in the along row direction, which supports the above hypothesis. Yet, the ω is fairly independent of the incidence angle.

Many studies assume for L-band the ω equal to zero as scattering within the canopy is generally negligible for the longer wavelengths and its effect on T_B simulations by the τ - ω model is highly correlated with the τ . Our results show, however, that as the leaves lose their water at senescence scattering within a corn canopy becomes important particularly when viewing across rows. Under those conditions, adopting $\omega = 0.0$ requires an angular dependent b parameter for reproducing the measured T_B 's. Interestingly, however, the formulation proposed by Wigneron et al. (1995) is able to replicate this angular dependency evolving from assuming $\omega = 0.0$ reasonably well. In some cases, however, the obtained tt_H parameters are beyond the ranges reported previously (e.g. Pardé et al. 2003, Wigneron et al. 2007), especially for the across row view geometry. A consequence of a large tt_H is that the inverted b attains an unrealistically low value.

Table 4-9: Regression coefficients of the function $h_r = h_1 sm + h_0$ fitted for five periods with LRAD measurements.

<i>Period</i>	<i>SM range</i> $m^3 m^{-3}$	$h_r = h_1 sm + h_0$		<i>RMSD (K)</i>	
		h_1	h_0	$h_r \sim sm$	<i>Incid.</i>
<i>8 -10 June</i>	0.22-0.18	-9.68	1.67	3.64	5.89
<i>24-27 June</i>	0.14-0.11	-16.45	1.71	3.58	4.06
<i>2-4 July</i>	0.09-0.06	-9.60	1.03	3.13	3.20
<i>20-23 August</i>	0.02-0.01	-7.58	0.46	3.18	3.18
<i>29 Aug. – 3 Sept.</i>	0.28-0.23	0.39	0.52	2.76	2.78

h_r Dependence on soil moisture

Next to optimizing parameterization defining the τ , the regression coefficients h_1 and h_0 were calibrated to evaluate the dependence of h_r on soil moisture during each of the five measurement periods. Table 4-9 gives the obtained parameters and the RMSD's computed between the simulated and measured T_B . In addition, the RMSD's obtained by fitting the b for each incidence and azimuth angle are given for reference. These b values have also been used while optimizing h_1 and h_0 . As such, resulting parameters only corrected for the soil moisture dependence of h_r and not for potential changes in the physical roughness as those effects are implicitly included in the calibrated b values.

The RMSD's presented in Table 4-9 indicate that by defining the h_r as a function of soil moisture improvements are obtained for the periods starting on June 8 and 24. The effect on the simulated T_B is clearly visible in Figure 4-4 for June 8. For the two episodes, the error levels reduce from 5.89 to 3.64 K and 4.06 to 3.58 K, respectively. Effectively, the improved T_B simulation is achieved by increasing h_r as the soil dries, which is consistent with various recent studies (e.g. Saleh et al. 2007, Escorihuela et al. 2007, and Panciera et al. 2009a).

Wigneron et al. (2001) associated the higher h_r values with an increase in the spatial heterogeneity of the dielectric properties. During dry-downs, typically, the micro-scale soil moisture variability increases, causing a strong dielectric contrast within the soil volume. This enhances the surface emission and is considered as a ‘dielectric roughness’. Since the spatial soil moisture variability is often large in the mid range (e.g. Ryu and Famiglietti 2005, Van der Velde et al. 2008), the dielectric roughness effect is expected to be largest under those conditions. This explains the large RMSD reduction for June 8th (2.26 K), while for June 24th the RMSD decreases merely 0.48 K and the effect is almost negligible for the other periods. Similarly, both Saleh et al. (2007) and Escorihuela et al. (2007) found that the dielectric roughness came only into effect below certain moisture contents. As an addition to these two investigations, Panciera et al. (2009b) concluded also that as the soil moisture content approaches residual conditions the soil moisture dependency of h_r reduces.

Compared to these studies, the values for the slope (h_1) presented in Table 4-9 are on the same order of magnitude, though somewhat larger. This difference is most likely explained by the employed procedure. Here the coefficients are fitted for individual time series with a fairly small dynamic range, whereas the studies cited above fitted complete data sets. The h_1 values in Table 4-9 are, thus, only representative for the specific soil moisture conditions, while slope reported by the studies cited above are valid for a wider soil moisture range.

4.5 Discussion

The analysis of L-band H polarized T_B 's measured during several growth stages shows that the b parameter (for canopy opacity) and its dependence on incidence and azimuth angles change throughout the season. Moreover, the h_r is found to increase as the soil moisture content decreases during a specific part of the dry-down cycle. The relative importance of these uncertainties on T_B simulations is discussed here. The fraction of the optimum performance (F) is defined as,

$$F = 1 - \frac{(RMSD_i - RMSD_{\min})}{RMSD_{\min}} \times 100\% \quad (4.8)$$

where $RMSD_i$ is RMSD computed between the measured and simulated T_B for a specific calibration (K) and $RMSD_{\min}$ is the minimum $RMSD$ achieved for a continuous period of LRAD measurements (K).

The F 's have been calculated for all six calibrations and are presented in Figure 4-9 for each episode in a separate plot. The plots show that the largest variations in performance occur on June 8th and August 29th. The definition of the h_r as a function of soil moisture reduces for June 8th the RMSD by 38%, while for August 29th the calibration of the b and t_H for each azimuth angle separately is responsible for a 27% RMSD reduction. Also, noteworthy is the more than 10% error reduction on June 24th using either an azimuth angle dependent vegetation or soil moisture dependent roughness parameterization. The improvement in the T_B simulation for the other two periods is, however, in total less than 20% and does not exceed 8% for individual sources of uncertainty. Averaged over all

five episodes, the calibration of the b and tt_H for each azimuth angle separately results in improvements (11.5%) twice as large as for the other optimizations.

These results demonstrate that uncertainties in T_B simulations are largest at the start and end of the corn growing season. At an early growth stage, the T_B simulations mainly are uncertain due to a combination of the soil moisture dependence of h_r and the effect of the crop row orientation relative to view direction. At senescence, the crop row orientation primarily affects the reliability T_B simulations. Of course, at the satellite scale (>10 km) these effects may not be directly observable, especially the crop row effects. However, uncertainties like these affect the overall accuracy of soil moisture products from satellite missions, such as SMOS and SMAP. Moreover, via simulation of T_B 's at a high spatial resolution using a process model, as demonstrated by Crow et al. (2005), it could be possible to take these field scale effects into consideration.

H polarized L-band emission during the corn growth cycle

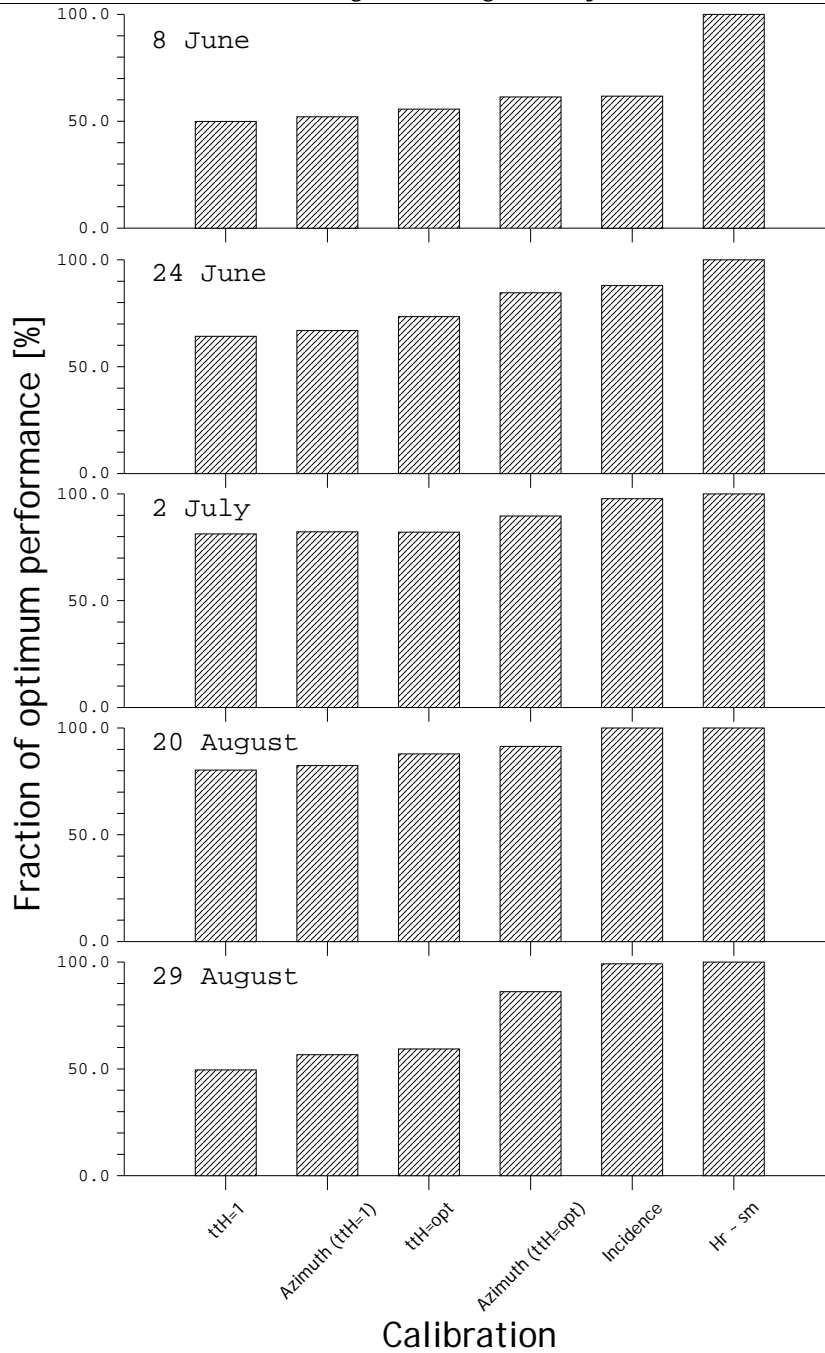


Figure 4-9: The fraction of the optimum performance calculated for all six calibrations plotted for each of the five measurement episodes.

4.6 Conclusions

From a combined active/passive microwave remote sensing campaign conducted in 2002, hourly L-band H polarized T_B measurements are available for five episodes distributed over the corn growth cycle. These measurements were collected at five incidence angles and three azimuth angles relative to crop row orientation. A labor intensive ground characterization took place on a weekly basis in the direct proximity of the footprints and, at some distance (<100 m), a suite of automated instruments were available to support the microwave data sets. In this investigation, the soil moisture and temperatures measured at preset time intervals have been utilized as input for the τ - ω model to reproduce the measured T_B cycles. Via calibration of the model's vegetation and roughness parameterizations, the impact of the changing canopy structure throughout the season and soil moisture dependence of the h_r are evaluated.

This study shows that the b parameter, defining the τ , and its dependence towards the incidence and azimuth angles change both during the growth cycle. The b found for the early growth stage is about three times larger than expected based on the literature, while near peak biomass and at senescence its value is about half. The latter is mainly caused by assuming the scattering within canopy to be negligible by setting the ω equal to zero. The larger b at the beginning of the growth cycle is, however, consistent with a previous report by Wigneron et al. (2004).

More surprising is the changing angular dependence of the b during the growing season. In general, the b parameter decreases with the incidence angle in the early growth

phase, which might be attributed to the predominant vertical structure of the corn plants at this stage. Closer to peak biomass the leaves develop in the horizontal direction and form a closed canopy, which is associated with the observed weakening of the angular dependencies as the leaf coverage attenuates angular dependent contributions. These attenuating effects of the leaves disappear at senescence as the foliage loses its water and, thus, the influence exerted by the stems increase. For this growth stage, an increase of the b with the incidence is observed when the ω is taken equal to zero, which is most notable when viewing across the rows. However, it is found that when assuming a single b value for all incidence angles, the optimized ω 's are well above zero and fairly independent of the incidence angle. Larger ω 's are, however, obtained for the across row than for along row view direction. These results suggest that scattering within a corn canopy is primarily induced by stems, which becomes particularly important at senescence. The change in the scattering cross sections of the vertically oriented corn stems with azimuth explains the dependence of the ω on the crop row orientation. The assumption $\omega = 0.0$ requires, thus, an angular dependent b parameter for reproducing the T_B measurements at senescence. This study also shows that the parameterization proposed by Wigneron et al. (1995), included in L-MEB is able to replicate the angular dependence of b observed for different azimuthal angles during various growth stages.

In addition, calibration of the regression coefficients defining the relationship between soil moisture and h_r indicate that the effective roughness increases as the soil dries. This dependence of h_r is found to be responsible for significant uncertainties particularly near

field capacity, which typically is representative of loamy sand the $0.1 - 0.2 \text{ m}^3 \text{ m}^{-3}$ soil moisture range. Previously, similar h_r increments in response to a soil moisture decrease were associated with a spatial heterogeneity of the dielectric properties (e.g. Wigneron et al. 2001, Escorihuela et al. 2007). The typically large spatial variability near field capacity explains the larger uncertainty imposed by the soil moisture dependence of h_r under those conditions, which is supported by the findings of Panciera et al. (2009b).

In summary, this investigation of L-band H polarized demonstrates that the b parameter (or τ) and its angular dependence change throughout the corn growth cycle. It is shown that near field capacity, the h_r increases as the soil moisture content decreases. Discussion of the relative importance of these two sources of uncertainty suggests that at the start of the crop development ($W < 1.0 \text{ kg m}^{-2}$) an imperfect parameterization of the angular dependence of b can account for about a 10 % error in T_B simulations, while this source of uncertainty causes errors up to 27 % at senescence. On the other hand, the soil moisture dependence of h_r accounts for an error of about 38 % at beginning of the growth cycle. Encouraging, is that near peak biomass neither the angular dependence of the b nor the soil moisture dependence of h_r was found to significantly degrade the reliability of T_B simulations. This means that the commonly adopted assumptions (e.g. $tt_H = 1$ and $\omega = 0.0$) are reasonable for peak biomass. Therefore, it may be hypothesized that the uncertainties discussed above affect mostly the soil moisture retrievals at the start and end of the growth cycle. Including a soil moisture dependent h_r parameterization and

H polarized L-band emission during the corn growth cycle

accounting for the changing angular dependencies of the empirical b parameter can assist

in developing more robust soil moisture products.

5 Modeling L-band emission during a corn growing season

This chapter is based on:

Joseph, A.T., van der Velde, R., Ferrazzoli, P., O'Neill, P.E., Lang, R.H., Gish, T., “Modeling L-band emission during the corn growth cycle using a discrete medium scattering model”, *to be submitted to IEEE Transaction on Geoscience and Remote Sensing*.

5.1 Introduction

In the previous chapter, diurnal cycles of H polarized L-band T_B measurements were analyzed by fitting the vegetation parameters of the semi-empirical τ - ω model. One of the main findings from this analysis is that the empirical parameter, b , appearing in the formulation of the canopy opacity changes throughout the corn growth cycle. At the early growth stage, the b value is, for example, three times larger than expected, while close to peak biomass and senescence its value reduces to half. Although the unusually small b values at large biomass may have been induced by other settings within the τ - ω model, the large b values at the early growth stage are consistent with results by Wigneron et al. (2004).

Unfortunately, the L-band radiometer data set collected during the 2002 OPE³ campaign is restricted to a limited number of episodes that leave various parts of the growth cycle uncovered. Therefore, the conclusions drawn with respect to the seasonal dependency of the empirical b should also be confirmed using other data sources. Other ground based L-band radiometer data sets collected during the complete corn growth cycle are, however, rare.

On the other hand, as a part of the 2002 OPE³ campaign a comprehensive set of vegetation morphological variables were measured once a week. These vegetation variables are input for physically discrete medium scattering models. As described in

section 2.4, discrete medium scattering models are used to compute the bistatic scattering coefficient. Integrating this bistatic scattering over the hemisphere yields the total reflection, which can be converted into the emissivity. Essentially, this is the concept of Peake's Law.

In this Chapter, the vegetation morphological measurements are used as input for the Tor Vergata model for simulating the L-band emissivity (or brightness temperature) throughout the complete corn growth cycle. An additional advantage of employing the discrete medium approach for simulating the emissivity is that the effects from the soil surface and vegetation can be quantified in a detailed and a physical manner. The specific reason for selecting the Tor Vergata model is that it adopts the matrix doubling algorithm, which allows taking multiple scattering between the different constituents of the soil-vegetation system (e.g. leaves, stems, soil surface) into consideration. Further, in recent years the Tor Vergata model has been used fairly successfully in several investigations for simulating both the backscattering and emission from soil-vegetation systems.

For example, Della Vecchia et al. (2006a, 2008) employed the Tor Vergata model for simulating the C-band backscattering from a wheat and a corn field. Moreover, the passive microwave version of the Tor Vergata model has been applied by Della Vecchia et al. (2006b, 2010) for simulating the L-band emission of forest stands. The Tor Vergata model, however, has not yet been applied for simulating the microwave emission over agricultural fields during growth cycles (e.g., corn). Such analysis is interesting because it

may provide insight into the effect that morphological changes have on the microwave emission, which is directly relevant for the retrieval algorithm of future satellite remote sensing soil moisture missions, (e.g., SMAP).

In the studies cited above several improvements were introduced to the geometric representation of vegetation morphology. Along with these developments, concerns have also been raised with the dielectric representation of scatterers. The most interesting results were recently presented in Mironov et al. (2009). They presented a comprehensive validation and showed that the soil dielectric mixing model developed by Dobson et al. (1985) overestimates the soil dielectric constant by more than 30%. Currently, the Dobson et al. (1985) model is the most widely used approach for obtaining dielectric constants of wet soils in both retrieval algorithm and discrete scattering models. Yet, the impact of such difference in soil dielectric constant is unknown, specifically over vegetated areas.

In this Chapter two issues will be investigated using emissivity simulations performed by the Tor Vergata model. The main objective of this research is to study the impact that changes in corn morphology have on the emissivity and analyze the soil moisture sensitivity during the corn growth cycle. In addition the influence of the applied dielectric mixing model on these results is investigated.

5.2 Parameterization of the Tor Vergata model

The concepts and some mathematical details of the Tor Vergata model are given in Chapter 2. From this description, it is evident that application of the Tor Vergata model

Modeling L-band emission during a corn growing season

requires an extensive characterization of the orientation, geometry and dielectric properties of scatterers within the soil-vegetation matrix. The specific settings and measured variables adopted for the Tor Vergata simulations presented here are briefly described below.

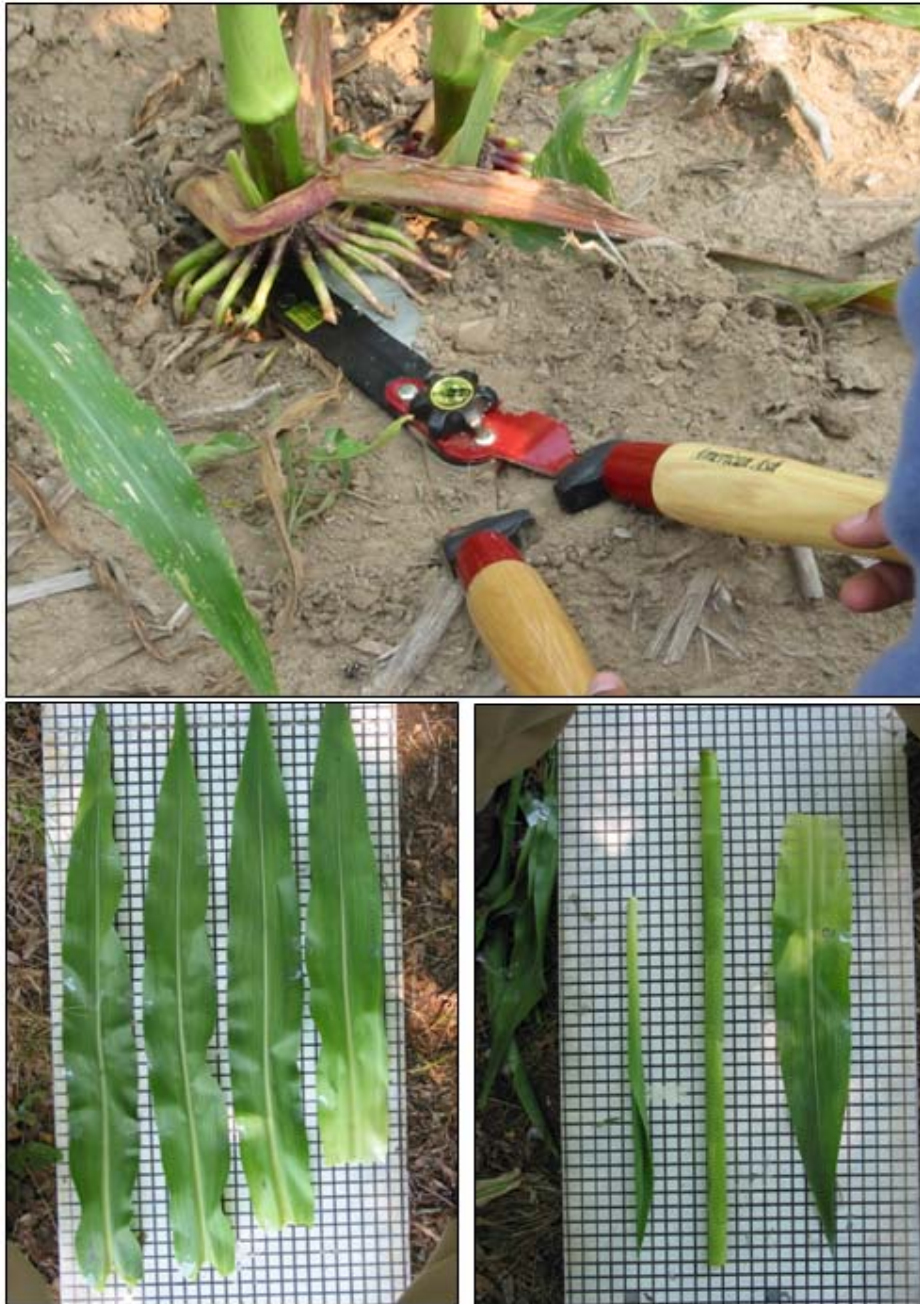


Figure 5-1: Photographs of the measurements carried out to characterize the vegetation morphology (e.g. leaf and stem dimensions) during the 2002 OPE³ campaign.

The Tor Vergata model has adopted the Integral Equation Method (IEM) (Fung et al. 1992) approach for quantifying the soil surface scattering (emission) contribution; hence, the soil parameters needed for the Tor Vergata model are the same as the ones required for the IEM. This parameterization includes, apart from the soil dielectric properties, the root mean square height (s), correlation length (l) and autocorrelation length function (ACF). The surface geometry parameters are obtained from the digitized surface height profiles collected in the along tillage row direction. This parameterization includes s and l values of 0.89 cm and 5.13 cm respectively, and an exponential ACF. Further, the soil textural information, including 60.3% sand and 16.1% clay, is utilized to compute the soil dielectric constant through application of Dobson's and Mironov's dielectric mixing models. Detailed information about these two dielectric models is given in the following section.

Table 5-1: Soil surface and vegetation input variables for the Tor Vergata scattering model.

<i>Variable</i>	<i>Data source/ value</i>	
<i>Soil surface</i>		
rms height, s	measured	0.89 cm
Correlation length, l	measured	5.13 cm
Autocorrelation, ACF	estimated	exponential
Dielectric constant	Dobson/Mironov model	
<i>Vegetation</i>		
Dielectric constant	Mätzler model	
Leaf width (disc radius)	estimated	3.5 cm
Leaf Area Index (LAI)	measured	<i>variable</i>
Leaf thickness	estimated	0.021 cm
Leaf angles	estimated	5° - 85°
Stem radius	measured	<i>variable</i>
Stem length	measured	<i>variable</i>
Leaf angles	estimated	2° - 5°

Using models that adopt the discrete medium approach, the vegetation layer is represented as individual scatterers with a predefined shape. Two types of scatterers are utilized within the Tor Vergata model to represent corn canopies. Circular disks are used for leaves and cylinders define the stems within canopies. The electromagnetic properties of both disks and cylinders are derived from their orientation, dimensions and dielectric properties.

The *dielectric properties of vegetated materials* can be calculated using mixing models developed by Ulaby and El-Rayes (1987) and Mätzler (1994). These vegetation mixing models require the fresh and dry biomass weights as input, which have been measured for the individual crop elements (e.g. leaves, stems) for 12 plants about once a week during the 2002 OPE³ campaign. For the research presented in this Chapter Mätzler's mixing model has been applied to derive the dielectric constants for the stems and leaves. Details about this mixing model can be found in Mätzler (1994).

As for the *vegetation morphology*, the dimensions of the leaves and stems have been recorded for one representative out of twelve plants. An illustration of these measurements is shown in Figure 5-1.

In the Tor Vergata model the leaf coverage is modeled as an ensemble of circular disks. The radius of each disk is set at 3.5 cm, which is on average about half of the measured leaf width. Then, the measured Leaf Area Index (LAI) is used to determine the number of disks needed to represent the foliage. Further, the leaf thickness makes the description of the leaf dimensions complete, which is fixed at 0.021 cm based on measurements and

previous experience. The angles of the leaves (disks) with the normal are varied from 5° to 85° with an interval 5° .

The dimensions of the cylinders, representing the stems, are characterized by a radius and length. Both were measured during the 2002 OPE³ field campaign and these measurements are used as input for the model. The angle of the stems with the normal is estimated to vary from 2° to 5° with an interval of 1° . Further the stems density is set at 12 stems per m^2 .

A summary of the soil-vegetation information needed for Tor Vergata model simulations is presented in Table 5-1.

5.3 Dielectric mixing models

The importance of the soil and vegetation dielectric constant (or *permittivity*) in both semi-empirical and physically based emission models was described in Chapter 2. The dielectric constant of the non-polar (typically solid) materials within soil medium and canopy layer can be considered frequency independent. Due to its dipole, water is a polar material and its content within the soil and vegetation volume has an effect that changes with the frequency of the emitted wave (Rees 2001).

For free water, the real and imaginary part of the dielectric constant can be computed as a function of the frequency through application of the well-known Debye formulas (Debye 1929),

$$\varepsilon' = \varepsilon_{\infty} + \frac{\varepsilon_0 - \varepsilon_{\infty}}{1 + (2\pi f\tau)^2} \quad (5.1)$$

$$\varepsilon'' = \frac{\varepsilon_0 - \varepsilon_{\infty}}{1 + (2\pi f\tau)^2} 2\pi f\tau + \frac{\sigma}{2\pi\varepsilon_r f} \quad (5.2)$$

where ε' and ε'' are the real and imaginary part of the dielectric constant related to each other as $\varepsilon = \varepsilon' - i\varepsilon''$, ε_{∞} is the dielectric constant in the high frequency limit (= 4.9), ε_0 is the static dielectric constant, f is the frequency of the wave (Hz), τ is the relaxation time (s) related to the relaxation frequency as $f_0 = (2\pi\tau)^{-1}$ and σ is the effective conductivity (Siemens m⁻¹), ε_r is the dielectric constant for free space (= 8.854 10⁻¹² F m⁻¹).

When present within a medium, the bonds between water and the molecules of the solid material also affect the magnitude of the real and imaginary part of the dielectric constant. As such, methods for integrating the effects of water, air and solid materials have been developed for both soils and vegetation. These so-called dielectric mixing models all evolved from the refractive dielectric mixing model originally proposed by Birchak et al. (1974),

$$\varepsilon^{\alpha} = \sum_{i=1}^n W_i \varepsilon_i^{\alpha} \quad (5.3)$$

Essentially, equation 5.3 states that the ε of a medium is the sum of contributions from individual components (e.g. solid material, air, free (and bound) water), which is

taken proportional to the volume fraction (W). Initially, Birchak et al. (1974) found that $\alpha = 0.5$ applies for an isotropic two phase medium, while others adopted other values.

For this Chapter, the Tor Vergata model was used to simulate the emssivity using two soil dielectric mixing models. The applied dielectric mixing models are the ones reported by Dobson et al. (1985) and Mironov et al. (2009). In the text below follows a brief description of these dielectric models.

Soils

Over the past decades, the most widely used soil dielectric model within soil moisture retrieval algorithms has been the one developed by Dobson et al. (1985). The derivation of this model started from rewriting Eq. (7.3) as the sum of the dielectric contributions of the individual constituents of the soil medium (e.g. solid material, air, free and bound water). By combining the effect of free and bound water, Dobson et al. arrived at the following semi-empirical expressions for respectively the real and imaginary part of the soil dielectric constant,

$$\varepsilon' = \left[1 + \frac{\rho_b}{\rho_s} (\varepsilon_s'^{\alpha} - 1) + m_v^{\beta'} \varepsilon_{fw}^{\alpha} - m_v \right]^{1/\alpha} \quad (5.4)$$

$$\varepsilon'' = \left[m_v^{\beta''} \varepsilon_{fw}^{\alpha} \right]^{1/\alpha} \quad (5.5)$$

with

$$\varepsilon_s' = (1.01 + 0.44 \rho_s)^2 - 0.062 \quad (5.6)$$

where m_v is the volumetric moisture content ($\text{m}^3 \text{ m}^{-3}$), ρ_b is the dry bulk density (g m^{-3}), ρ_s is the specific density of solid materials ($\sim 2.66 \text{ g cm}^{-3}$), α is empirically set to 0.65 and empirical relationships are used to describe β' and β'' as a function of soil textural information, according to,

$$\beta' = 1.2748 - 0.519S - 0.152C \quad (5.7)$$

$$\beta'' = 1.33797 - 0.603S - 0.166C \quad (5.8)$$

where S and C are the volume fractions for sand and clay.

Further, the Debye equations are applied to calculate the dielectric properties for free water. Debye's original formulation is used to compute the ϵ_{fw}' , whereas a slightly modified form is adopted for the calculation of ϵ_{fw}'' . These expressions read,

$$\epsilon_{fw}' = \epsilon_{w\infty} + \frac{\epsilon_{w0} - \epsilon_{w\infty}}{1 + (2\pi f \tau_w)^2} \quad (5.9)$$

$$\epsilon_{fw}'' = \frac{\epsilon_{w0} - \epsilon_{w\infty}}{1 + (2\pi f \tau_w)^2} 2\pi f \tau_w + \frac{\sigma}{2\pi \epsilon_r f} \frac{(\rho_s - \rho_b)}{\rho_s m_v} \quad (5.10)$$

where τ_w is the relaxation time of free water, ϵ_{w0} and $\epsilon_{w\infty}$ are the low and high frequency limits of free water. Typically, $\epsilon_{w\infty}$ is fixed at 4.9, and formulations for τ_w and ϵ_{w0} as a function of both temperature and salinity are given in handbooks, such as Ulaby et al (1986). As an indication, the $2\pi\tau_w = 0.58 \cdot 10^{-10} \text{ s}$ and $\epsilon_{w0} = 80.1$ at a temperature of 20 °C for a salt free medium.

The unknown remaining is the effective conductivity, which is given as function of soil texture by,

$$\sigma = -1.645 + 1.939\rho_b - 2.25622S + 1.594C \quad (5.11)$$

for 1.4 – 4.0 GHz

$$\sigma = 0.0467 + 0.2204\rho_b - 0.4111S + 0.6614C \quad (5.12)$$

for 0.3 – 1.4 GHz

A limitation of this approach is that only the dielectric constant of free water is included in the dielectric constant calculations, while both bound and free water are present in the soil-air-water mixture.

Mironov et al. (2004) considered both free and bound soil water in their dielectric mixing model, which also starts from defining the complex refractive index as $n^* = \sqrt{\epsilon}$. This allows rewriting the real and imaginary part of the dielectric constant as,

$$\epsilon' = n^2 - \kappa^2 \quad (5.13a)$$

$$\epsilon'' = 2n\kappa \quad (5.13b)$$

where n is the refractive index, κ is the normalized attenuation coefficient.

Following Birchak refractive dielectric mixing model the complex refractive index can be computed for soils with and without free water as,

$$\begin{aligned}\sqrt{\varepsilon} &= \sqrt{\varepsilon_s} + (\sqrt{\varepsilon_{bw}} - 1)m_v && \text{for } m_v \leq W_t \\ \sqrt{\varepsilon} &= \sqrt{\varepsilon_s} + (\sqrt{\varepsilon_{bw}} - 1)W_t + (\sqrt{\varepsilon_{fw}} - 1)(m_v - W_t) && \text{for } m_v \geq W_t\end{aligned}\quad (5.14)$$

where ε_{bw} is the complex dielectric constant of bound water and W_t is the maximum bound water fraction.

Mironov et al. adopt the same analogy for calculating the refractive index, n , and the normalized attenuation coefficient, κ , which are computed as,

$$\begin{aligned}n &= n_s + (n_{bw} - 1)m_v && \text{for } m_v \leq W_t \\ n &= n_s + (n_{bw} - 1)W_t + (n_{fw} - 1)(m_v - W_t) && \text{for } m_v \geq W_t\end{aligned}\quad (5.15)$$

$$\begin{aligned}\kappa &= \kappa_s + \kappa_{bw}m_v && \text{for } m_v \leq W_t \\ \kappa &= \kappa_s + \kappa_{bw}W_t + \kappa_{fw}(m_v - W_t) && \text{for } m_v \geq W_t\end{aligned}\quad (5.16)$$

where subscripts s , bw and fw represent the electromagnetic properties of solid material, bound and free water.

Once all variables in Eqs. (5.15) and (5.16) are known the resulting refractive index and normalized attenuation coefficient can be utilized to compute the real and imaginary part of the soil dielectric constant using Eq. (5.13). Mironov et al. accomplished this by developing empirical relationships based on an extensive database of measured soil dielectric properties.

The fraction maximum bound water, W_t , is for example defined as,

$$W_t = 0.02863 + 0.30673C \quad (5.17)$$

Further, for the solid materials, the obtained relationships between the electromagnetic properties, n and κ , and soil texture are given by,

$$n_s = 1.634 - 0.539C + 0.2748C^2 \quad (5.18)$$

$$\kappa_s = 0.03952 - 0.04038C \quad (5.19)$$

For obtaining the n and κ of bound and free water, the inverse transformation of Eq. 5.13 is used, which is given by,

$$n\sqrt{2} = \sqrt{\sqrt{(\varepsilon')^2 + (\varepsilon'')^2} + \varepsilon'} \quad (5.20)$$

$$\kappa\sqrt{2} = \sqrt{\sqrt{(\varepsilon')^2 + (\varepsilon'')^2} - \varepsilon'} \quad (5.21)$$

These two equations (Eq. 5.20 and 5.21) allow computing the n and κ of bound and free water using ε' and ε'' . For quantifying both ε' and ε'' Mironov et al. employed the Debye equations and defined empirical relationships for the ε_0 , σ and τ_w as function of soil texture for both bound and free water. The relationships for bound water are given by,

$$\varepsilon_{0bw} = 79.8 - 85.4C + 32.7C^2 \quad (5.22)$$

$$\tau_{bw} = 1.062 \cdot 10^{-11} + 3.450 \cdot 10^{-12} C \quad (5.23)$$

$$\sigma_b = 0.3112 + 0.467C \quad (5.24)$$

and for free water by,

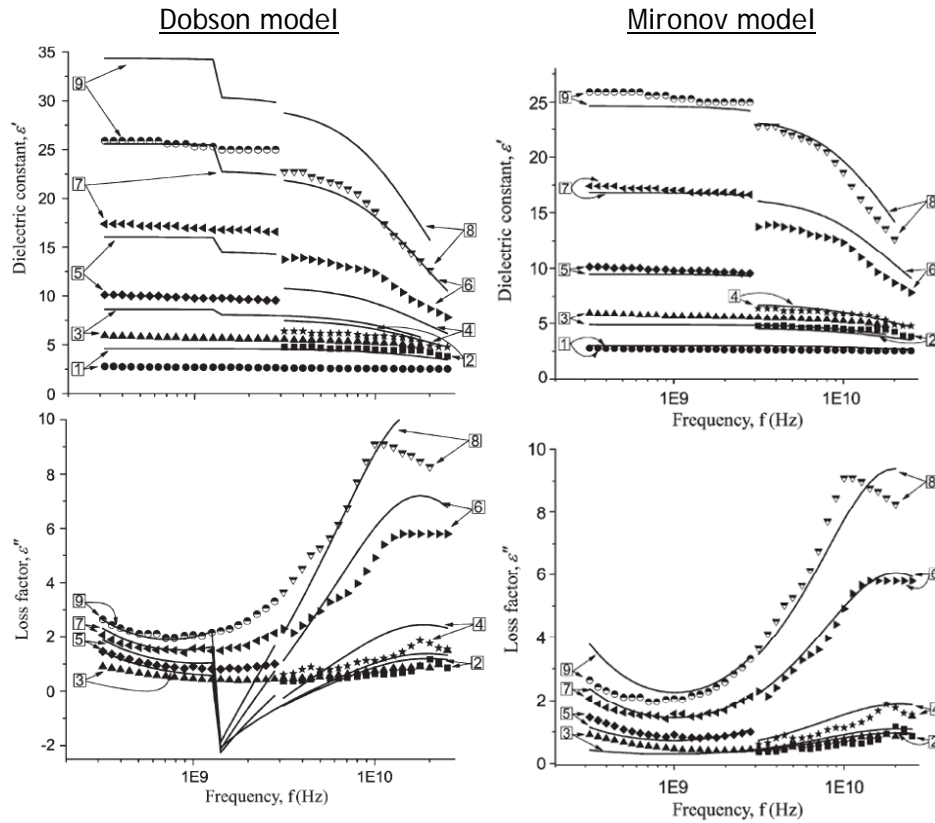
$$\varepsilon_{0fw} = 100 \quad (5.25)$$

$$\tau_{fw} = 8.5 \cdot 10^{-12} \quad (5.26)$$

$$\sigma_u = 0.3631 + 1.217C \quad (5.27)$$

In Mironov et al. (2009) an extensive validation is presented for both mixing models. Figure 5-2 presents their findings by plotting the real and imaginary parts of the predicted and measured dielectric constant as a function of the frequency for a silty sand soil. The plots show that the dielectric constants predicted by the mixing model clearly overestimate the measurements, whereas the predictions using Mironov model are much closer agreement with the measurements.

Figure 5-2: Real and imaginary parts of the predicted (lines) with Dobson's (left



panels) and Mironov's (right panels) mixing model for a silty sand soil with 77% sand, 9% Silt and 14% clay. The different lines indicate soil moisture contents ($\text{m}^3 \text{m}^{-3}$) labelled as [1] 0.032, [2] 0.080, [3] 0.088, [4] 0.132, [5] 0.184, [6] 0.291, [7] 0.297, [8] 0.382 and [9] $0.394 \text{ m}^3 \text{m}^{-3}$ (adopted from Mironov et al. (2009)).

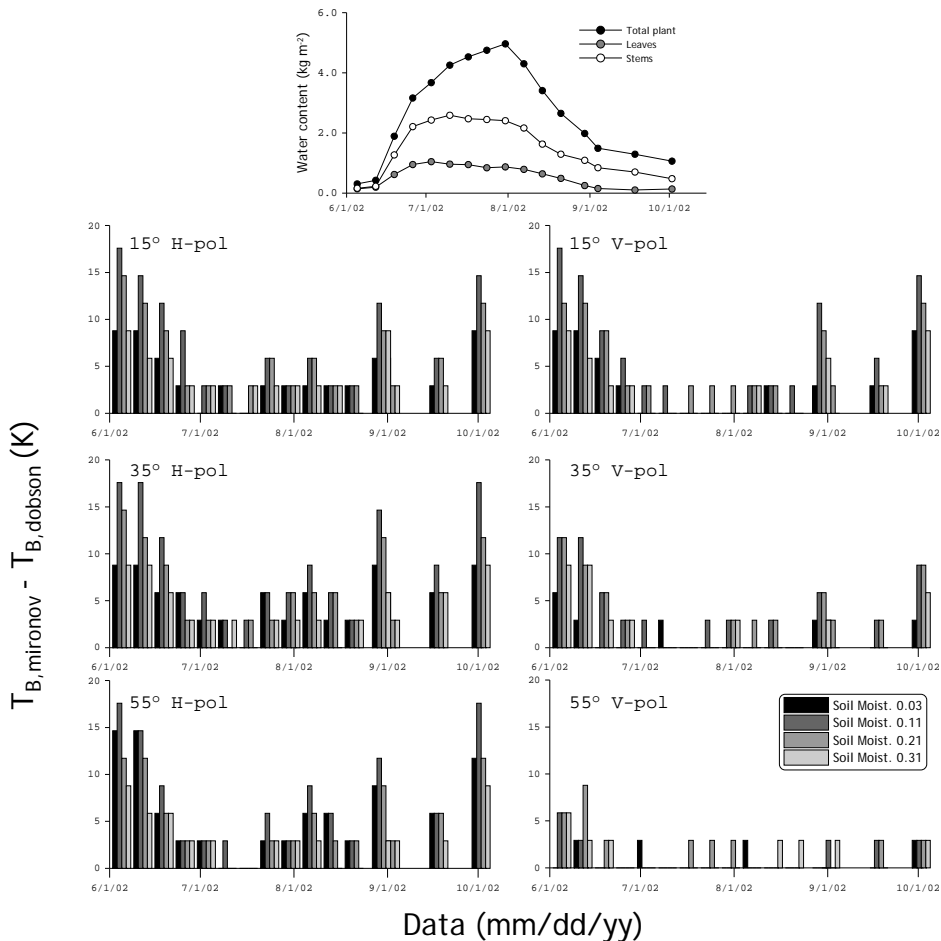


Figure 5-3: Differences in the emissivity simulated by the Tor Vergata model with the Dobson's and Mironov's dielectric for soil moisture contents of 0.03, 0.11, 0.21 and 0.31 m³ m⁻³. Assuming a 293.15 K (or 20 °C) temperature of the emitting layer the emissivity has been converted into brightness temperature.

5.4 Impact of mixing model

The overestimations by Dobson's mixing model, as demonstrated in Figure 5-2, are quite substantial and have had a significant impact on previously obtained results. For example, Escorihuela et al. (2010) found recently over a grass covered surface that the dependency of the roughness parameter, h_r , is less severe when using Mironov's instead

of Dobson's mixing model. As such, the significance of the soil moisture dependence of h_r found in Chapter 6 can be questioned. The brightness temperatures measured during the 2002 OPE³ campaign were, however, collected under different (more densely vegetated) conditions. The impact of the employed soil dielectric model on the simulated emissivity under such circumstances is uncertain and requires further investigation.

To this aim, Tor Vergata model simulations were performed with the soil dielectric model of Dobson and Mironov. Emissivities were simulated for incidence angles of 15°, 35° and 55° using the measured vegetation morphology (given in Table 5-1) and soil moisture contents of 0.03, 0.11, 0.21 and 0.31 m³ m⁻³. Then, the differences between the emissivities simulated with Dobson's and Mironov's dielectric model were compared for each soil moisture level. In Figure 5-3 these differences are plotted in the form of temperatures for an assumed temperature of the emitting layer of 293.15 K (or 20 °C). On top of these difference plots the total plant, leaf and stem water content are shown for reference.

The plots of Figure 5-3 demonstrate that the largest differences between the simulated emissivities occur where the vegetation water content is lowest. This is somewhat expected because the soil contribution is a less dominant from densely than sparsely vegetated surfaces. The magnitude of the difference in simulated brightness obtained using Dobson's and Mironov's mixing model is surprising; these may reach values larger than 15.0 K depending on the polarization, view angle and soil moisture level.

Typically, in the mid-soil moisture range (0.11 and $0.21 \text{ m}^3 \text{ m}^{-3}$) and H polarization differences are largest. Especially at the large view angles, the V polarized emissivity is insensitive to the employed dielectric model. On the other hand, differences between Dobson and Mironov for the H polarization are on the same order of magnitude for each angle. This can be explained by the fact that at large angles the H polarized brightness is reasonably sensitive to changes in the surface conditions, whereas the V polarized signal is often dominated by vegetation.

The emissivities simulated by the Tor Vergata model with Dobson and Mironov result in quite large temperature differences. Specifically, considering that error levels for brightness temperatures measured from space should be better than 2.0 K , the above analysis shows that the dielectric model should be selected with care. As the Mironov et al. (2009) have stated that the performance of their mixing model is superior to the model developed by Dobson et al. (1985); this dielectric model is used for the simulations presented in the following section.

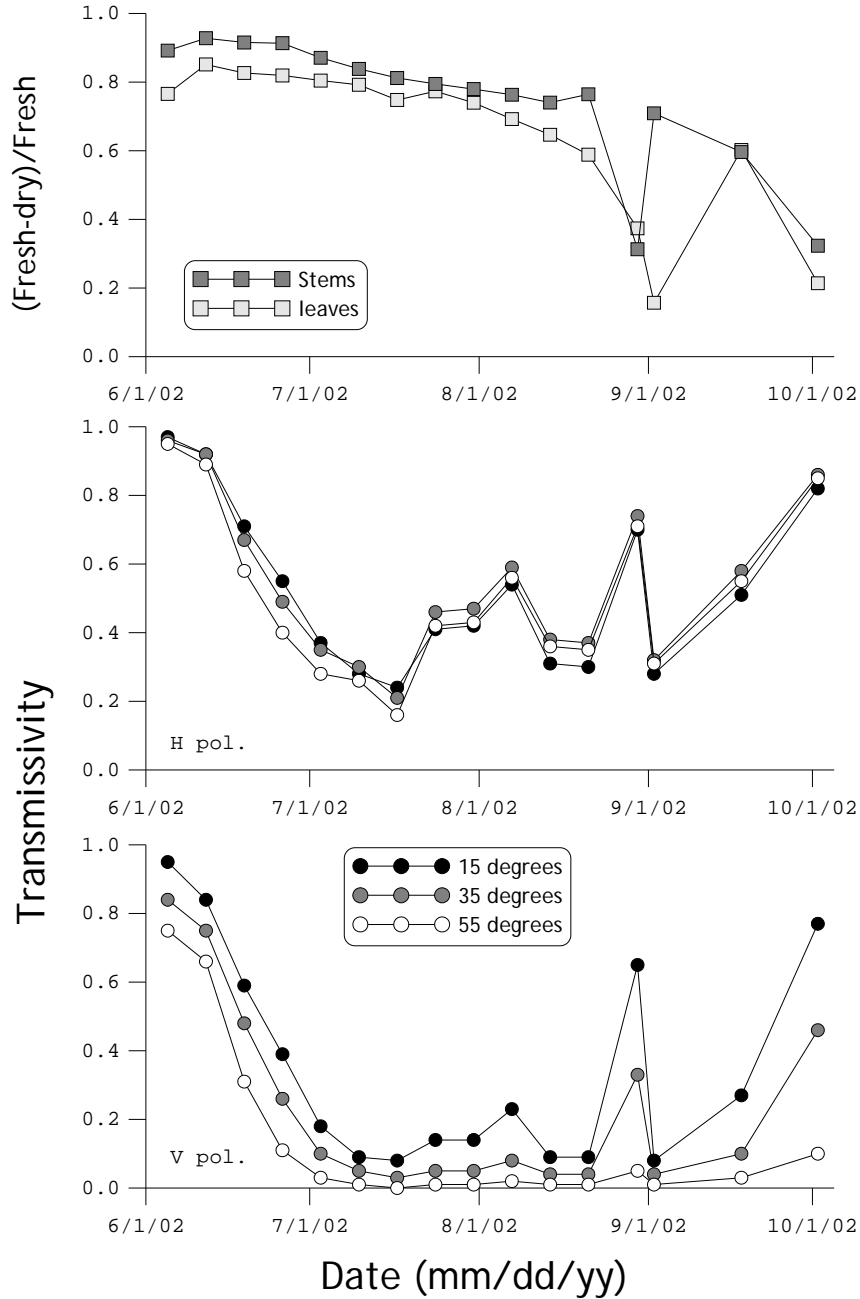


Figure 5-4: H and V polarized attenuation simulated by the Tor Vergata model for view angle of 15°, 35° and 55°. The top panel shows the (Fresh – Dry biomass)/ Fresh biomass used to compute the crop ϵ' .

5.5 Impact of corn on L-band emission

For analyzing the impact of corn on L-band emission, the simulated transmissivity and the sensitivity of the emissivity to soil moisture were evaluated. These simulations were performed using the Tor Vergata model with the Mironov soil dielectric model and same vegetation morphology that were used to generate the results of the previous section. Figure 5-4 shows the simulated H and V polarized attenuation against time for view angle of 15°, 35° and 55°.

The plots demonstrate, as expected, that both the simulated H and V polarization transmissivity are close to one at the early growth, decrease towards peak biomass and increase again as the crops become senescent. This evolution is in line with the development of the vegetation water content throughout the growth cycle as shown in Figure 5-4. Further, it was noticeable that the simulated V polarized attenuation is larger than the H polarization. This can be explained by the vertical structure of corn canopies, which typically has a stronger attenuating effect on the V than on the H polarization (e.g. Mattia et al. 2003, Joseph et al. 2010).

An anomaly in the time series of both H and V polarization is noted on August 30. On this day a strong increase in the H and V polarized transmissivity is observed. This is associated with an abrupt decrease in the ratio (fresh – dry)/fresh of the stem biomass, which is the variable used for the calculation of the dielectric constant of vegetation by Mätzler's model. The following measurement day the ratio (fresh – dry)/fresh of the stem biomass recovered and a dip was observed in the ratio of the leaf biomass. Yet, the

transmissivity simulated for this day is hardly affected. This supports one of the hypotheses posed in the previous Chapter that at senescence the foliage does not have a strong effect on the measured brightness temperature.

In order to make these results also relevant for the radiative transfer, $\tau-\omega$, model frequently adopted for soil moisture retrieval, the simulated transmissivities are converted to the empirical b parameter. Figure 7-5 shows the b values for the H and V polarization and view angle of 15°, 35° and 55° degrees. These plots show that from the beginning of the growth towards senescence the b value for both H and V polarization increase, which shows that it is contradictory with the results from Chapter 4.

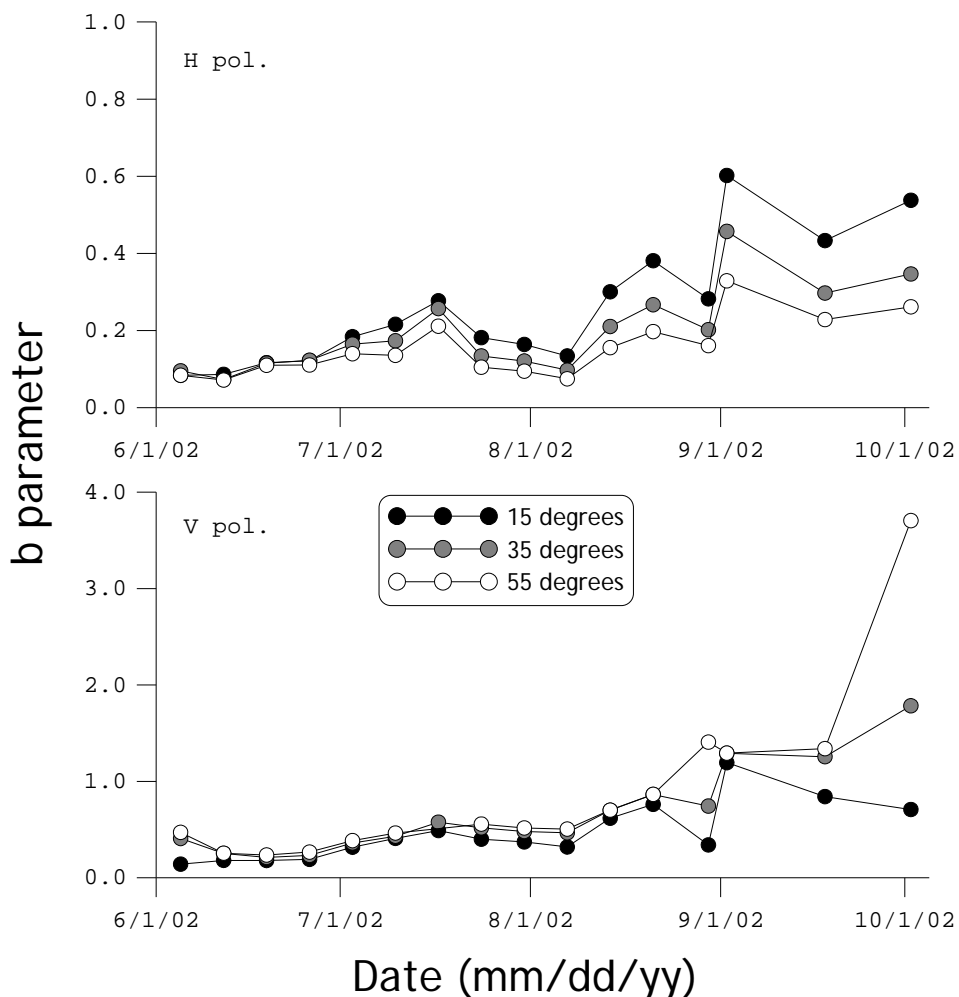


Figure 5-5: Empirical b parameters derived from the Tor Vergata model output for the H and V polarization and view angle of 15° , 35° and 55° .

In Chapter 4, b values derived from measurements showed a decreasing trend. It is also recognized that with the application of the semi-empirical radiative transfer approach several assumptions are made. The large b values at the early growth stage could, for example, be caused by uncertainties in the ground measurements. On the other hand, the low b values near biomass and at senescence were partly induced by assuming the single scattering albedo to be negligible. It should, thus, be appreciated that although both

models and measurements are uncertain, both data sources provide evidence for a seasonally dependent b parameter. Ideally, additional resources are needed in collecting the data sets required to validate physically scattering models.

Further, it is noted that the empirical b parameters simulated for the H polarization are quite different from the ones produced for the V polarization. The H polarized b values vary from 0.08 up to about 0.25 till August 14th, which are on the same order of magnitude as found in the literature. After this date, however, the biomass decrease associated with senescence sets in and the simulated b value increases. Typically, plants lose a considerable amount of water during senescence, while the crop dimensions remain about the same. It can be concluded that the simulated transmissivity does not depend as much on the vegetation water content as is expected. It should also be noted that even the “state-of-the-art” dielectric models for vegetation include uncertainties. If the vegetation dielectric constant as a function of water content is not properly quantified, the Tor Vergata model will not be able to simulate the transmissivity reliably.

A similar seasonal trend in the empirical b parameter is noted for the V polarization. The magnitude, starting with values of about 0.20 up to values well over 1.0, is much larger than for the H polarization and that is expected based on the scientific literature. These results implicate that soil moisture retrieval algorithm should not be developed assuming the H and V polarized transmissivity each to other. From this perspective, the ancillary data approach with only the H polarized brightness temperature as input appears

to be the most physically sound solution. In this context, it would probably be better to utilize the V polarization for the derivation of variables such as temperature.

To further evaluate the sensitivity of L-band emission for soil moisture during the corn growth cycle, the emissivity has been simulated with the Tor Vergata model using the vegetation morphological parameter described in section 5.2 and two extreme soil moisture levels, which are 0.03 and 0.49 m³ m⁻³. The difference between the emissivities simulated with the two moisture contents is multiplied by 293.15 K (or 20 °C) and plotted in Figure 5-6 for the three view angles and two polarizations.

As such, the plots of this figure demonstrate the theoretical potential of retrieving soil moisture reliably during a corn growth cycle. This potential is smaller for the V than for the H polarization because the change in H polarized brightness temperature is larger. At the H polarization, for example, a 4.0 Vol.-% change in soil moisture (equivalent to the accuracy requirements of the SMAP product) the brightness temperature changes 2.51 K, while for the V polarization this change is merely 0.88 K. This sensitivity of the brightness temperature to soil moisture should be evaluated against the sources of uncertainty involving the retrieval process in order to appreciate the above values. Considering the prospected 1.0 K measurement accuracy of the SMAP radiometer there will be, in case of the mature corn vegetation, little room for uncertainties within the radiative transfer aspect of soil moisture retrieval problem.

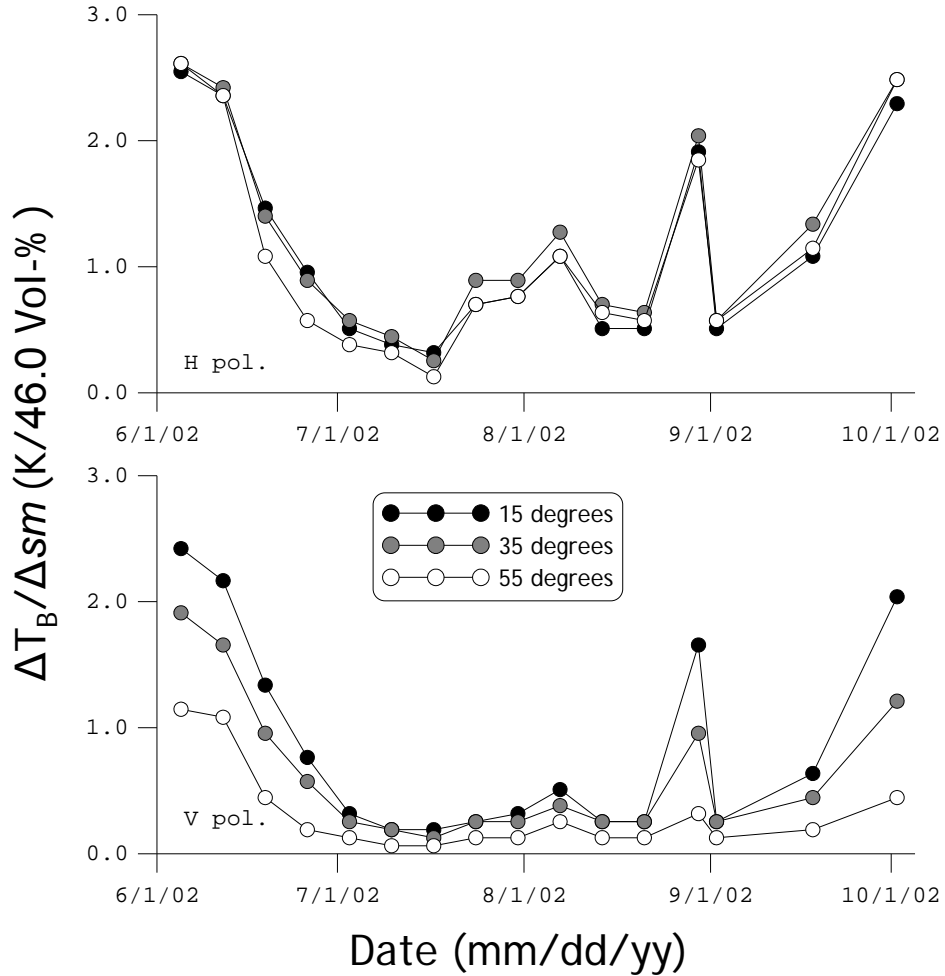


Figure 5-6: The difference in brightness temperature between simulations with soil moisture contents of 0.03 and $0.49 \text{ m}^3 \text{ m}^{-3}$ ($46.0 \text{ Vol-\%} = 0.49 - 0.03 \text{ m}^3 \text{ m}^{-3} \times 100\%$) assuming a temperature of 293.15 K (or $20 \text{ }^\circ\text{C}$).

5.6 Summary and conclusions

In this Chapter, the L-band emission simulated by the Tor Vergata discrete medium scattering model was discussed for a corn growing season. For these simulations the vegetation morphology measured during the 2002 OPE³ campaign were used. Two

aspects are investigated; the first is the impact of the applied soil dielectric model on the emissivity calculations and the latter is the effects of vegetation during the growth cycle.

Recently, the soil dielectric model developed by Dobson et al. (1985) was shown to overestimate the soil dielectric constant by more than 30%. Yet, Dobson's model has been the most widely used approach within soil moisture retrieval algorithms for many years. An alternative has been proposed by Mironov et al. (2004), which has been demonstrated to perform better.

In this Chapter, the simulations with the Tor Vergata model were performed using both Dobson's and Mironov's dielectric mixing model. It is shown that differences in the simulated emissivity are particularly large under sparsely (early growth stage) to moderately (senescence) vegetated conditions and may lead to temperature differences up to 15 K. Based on such large differences, a reappraisal of the soil dielectric model of choice would be recommended. Specifically, considering the poor performance of Dobson's mixing model presented by Mironov et al. (2009).

The second part of this chapter involves the analysis of transmissivity simulated by the Tor Vergata model and an evaluation of the sensitivity of the simulated emissivity to soil moisture. As expected, the simulated transmissivities decrease from values close to one at the early stage to values below 0.5 at peak biomass, and increase again near senescence.

Once the transmissivity are converted into the empirical b parameter, the results are less obvious. An increasing trend during the season is obtained for the simulated b values. It is found that the simulated transmissivities are not as much dependent on the vegetation water content as is expected from the ancillary data approach. This could be the case. However, it should also be noted that even the “state-of-the-art” dielectric model for vegetation include uncertainties, which may affect the simulated relationship between the transmissivity and vegetation water content. Ideally additional resources need to be invested in collecting the data sets needed for the validation of discrete medium scattering models.

6 Summary and conclusions

The goal of this dissertation research was to improve the quantification of the γ for soil moisture retrieval from satellite microwave radiometers on global scales. In order to achieve this goal, the objective of this research was to quantify uncertainties in the empirical constants induced by temporal variations in the vegetation cover. The methodology used to address this objective consisted of two parts:

- Using ground based radiometer data sets, the variability in the empirical constants over specific agricultural vegetation covers (e.g. corn) has been quantified using the semi-empirical, ancillary data approach;
- A physically-based scattering model (e.g. Tor Vergata model) has been employed to simulate the γ using the measured vegetation morphology as input. From the simulated transmissivities the empirical constants has been derived.

6.1 Research questions and outline

In carrying out this research, the following questions were addressed:

- What is the variability of the empirical constant derived from radiometer observations using the semi-empirical ancillary data approach?
- What is the variability of the empirical constant obtained through simulations with a physically based model using vegetation morphology parameterizations collected over the corn growth cycle?

- What is the influence of these uncertainties in the empirical constant on the retrieval of the soil moisture?
- Is it possible to develop a methodology to account for possible seasonal variations in the empirical constant?

This dissertation contributes to that improved understanding of microwave emission from the soil-vegetation system at a plot scale. In Chapter 3 and 4, for example, analyses are presented of the soil and vegetation component with the semi-empirical radiative model using the L-band microwave measurements collected during the 2002 OPE³ field campaign. Further, Chapter 5 presents L-band emissivity simulations over a corn growing season performed with the Tor Vergata discrete scattering model with measured vegetation morphology as input. These parts are briefly summarized in the text below.

6.2 Angular dependence of the soil roughness effects on microwave emission

In Chapter 3 different approaches for modelling the roughness effect on surface emission are discussed. This study is based on H polarized brightness temperatures measured by the automated L-band radiometer deployed during the 2002 OPE³ field campaign and dual-polarized L-band radiometer data set from the 1981 BARC experiments. A sufficiently detailed ground truth was collected during both field campaigns for deriving all variables needed for modelling the microwave surface emission from in-situ measurements.

From the H polarized data collected during the 2002 OPE³ campaign, the roughness parameters, h_r , were inverted using settings that ignore the possibility of polarization mixing, which are typical for the Choudhury et al. (1979) model. These inverted h_r parameters display, however, an unusual angular dependence. It is recognized that this could also have been caused by assuming the polarization mixing to be negligible. Both the H and V polarized smooth reflectivities are a function of the incidence angle. As such, excluding one of the two polarization components may induce a specific angular dependence of the h_r parameter.

This hypothesis was validated using the bare soil data sets collected during the 1981 BARC, which led to the conclusion that polarization mixing should be considered to avoid the necessity of angular dependent h_r parameters. This finding will be particularly important for retrieving soil moisture from the multi-angular data, such as SMOS and Aquarius.

6.3 Horizontal polarized L-band microwave emission

In Chapter 4, the ability of a semi-empirical radiative transfer model for reproducing the hourly H polarized brightness temperatures is evaluated for the five measurement episodes (> 2.5 days) distributed over the corn growth cycle. Specifically the effects of the changing canopy structure throughout the season and soil moisture dependence of the h_r are evaluated. This analysis provides experimental evidence that the empirical b parameter (or canopy opacity) and its angular dependence change over the season.

Moreover, it is shown that for a considerable part of the dry-down cycle, the h_r increases as the soil moisture content decreases.

Discussion of the relative importance of these two sources of uncertainty suggests that at the start of the crop development ($W < 1.0 \text{ kg m}^{-2}$) an imperfect parameterization of the angular dependence of b can account for about a 10 % error in T_B simulations, while this source of uncertainty causes errors up to 27 % at senescence. On the other hand, the soil moisture dependence of h_r accounts for an error of about 38 % at beginning of the growth cycle. Near peak biomass, however, neither the angular dependence of the b nor the soil moisture dependence of h_r is found to degrade the reliability TB simulations, significantly. This means that the commonly adopted assumptions (e.g. $t_H = 1$ and $\omega = 0.0$) are reasonable for peak biomass. Therefore, it may be hypothesized that the uncertainties discussed above affect mostly the soil moisture retrievals at the start and end of the growth cycle.

6.4 Model investigation of morphological effects on L-band emission

The preceding two Chapters involve detailed investigations of brightness temperature measurements collected during intensive field campaigns. Chapter 5 discusses the L-band emissivity simulated by the Tor Vergata discrete medium scattering model using the corn morphology measured during the 2002 OPE³ field campaign. The Tor Vergata model has been used to investigate two aspects: 1) the impact of the applied soil dielectric model and 2) the effects of vegetation throughout a growing season.

Summary and conclusions

The emissivity simulations by the Tor Vergata model have performed using the soil dielectric model by Dobson et al. (1985) and Mironov et al. (2004). It is shown that differences in the simulated emissivity are particularly large under sparsely (early growth stage) to moderately (senescence) vegetated conditions and may lead up to differences of 15 K (for a reference surface with a temperature of 293.15 K). Considering the poor performance of Dobson's mixing model presented by Mironov et al. (2009), a reappraisal of the soil dielectric model of choice is needed for future soil moisture retrieval processors.

Further the Tor Vergata model has also been used to simulate the transmissivity using a vegetation morphology measured during the growing season. As expected, the simulated transmissivities drop below values of 0.5 below peak biomass and increase towards senescence. Somewhat surprising, however, empirical b parameters derived from the simulated transmissivity increase particularly at senescence. It can be concluded that the simulated transmissivities are not as much dependent on the vegetation water content as is expected based on the ancillary data approach. This could also be the case in reality. It should, however, be also noted that the dielectric model for vegetation includes uncertainties, which may alter the vegetation dielectric constant and, as such, the simulated transmissivity.

6.5 Future work

The research presented in this dissertation shows through the analysis of experimental data sets as well as theoretical simulations that both the soil surface and canopy geometry

have important effects on the L-band microwave emission. Specifically, changes in the corn plant architecture contribute to large uncertainties at senescence. On the other hand, uncertainties in the soil surface geometry are important at the early growth stages of the corn canopy. Both sources of uncertainty mostly affect the angular dependence of the parameters used for vegetation and surface roughness corrections, and to a lesser extent absolute magnitude.

Consideration of these findings may prove particularly useful for improving the soil moisture retrieval from multi-angular data sets, such as the ones currently collected by SMOS. Of course, at the coarse resolution of SMOS pixels (>10 km) the effects observed at plot scale may not be directly noticeable. The SMAP mission will not measure multi-angular T_B 's and, thus, SMAP soil moisture retrievals can be expected to be less affected. Nevertheless, uncertainties like these have the potential to affect the overall accuracy of soil moisture products, particularly at the early growth stage and senescence.

However, measurements and models also include uncertainties, which require further investigation of the vegetation and surface roughness effects on microwave emission. Ideally, additional resources are needed in the collection of data sets at plot scale. It would be a great asset to the future improvement of physically based scattering models if future field campaigns also focus on collecting the data sets needed for validating discrete medium scattering models. This requires incorporating a comprehensive measurement strategy for the vegetation morphology including geometric and dielectric properties. Such data sets will help to improve the reliability of discrete medium scattering models

Summary and conclusions

through which our understanding of physically based microwave emission models will be further enhanced. This understanding can be used to develop more reliable parameterizations for the semi-empirical radiative transfer model used within soil moisture retrieval algorithms.

It is my goal to continue to improve the Tor Vergata model simulations to produce more realistic vegetation morphological parameters and verify reliability of the radar and radiometer calibration.

Due to recent changes within the SMOS algorithms, I would like to continue to research the differences and benefits of using the Mironov dielectric mixing model over the widely used Dobson model.

References

- Bindlish, R., Jackson, T.J., Wood, E., Gao, H., Starks, P., Bosch, D., & Lakshmi, V. (2003). Soil moisture estimates from TRMM Microwave Imager observations over the Southern United States. *Remote Sensing of Environment*, 47, 132-141.
- Bindlish, R.; Jackson, T.J.; Gasiewski, A.; Stankov, B.; Klein, M.; Cosh, M.H.; Mladenova, I.; Watts, C.; Vivoni, E.; Lakshmi, V.; Bolten, J.; Keefer, T. (2008). Aircraft based soil moisture retrievals under mixed vegetation and topographic conditions. *Remote Sensing of Environment*, 112, 375-390.
- Birchak, J.R., Gardner, C.G., Hipp, J.E., & Victor, J.M., (1974). High dielectric constant microwave probes for sensing soil moisture. In *Proc. IEEE*, Jan. 1974, 62, 92-98.
- Bosilovich, M.G., & Sun, W.-Y. (1999). Numerical simulation of the 1993 Midwestern flood: land-atmosphere interactions. *Journal of Climate*, 12, 1490-1504.
- Bracaglia, M., Ferrazzoli, P., & Guerriero, L. (1995). A fully polarimetric multiple scattering model for crops. *Remote Sensing of Environment*, 54, 170-179.
- Burke, E.J., Wigneron, J.P., & Gurney, R.J. (1999). The comparison of two models that determine the effects of a vegetation canopy on passive microwave emission. *Hydrology and Earth System Sciences*, 3, 439-444.
- Cano, A., & Co-authors (2010). The SMOS Mediterranean Ecosystem L-Band characterisation EXperiment (MELBEX-I) over natural shrubs. *Remote Sensing of Environment*, 114, 884-853.
- Cashion, J.; Lakshmi, V.; Bosch, D.; Jackson, T.J. (2005). Microwave remote sensing of soil moisture: evaluation of the TRMM microwave imager (TMI) satellite for the Little River Watershed Tifton, Georgia. *Journal of Hydrology*, 307, 242-253.
- Cosh, M.H.; Jackson, T.J.; Bindlish, R.; Famiglietti, J.S.; Ryu, D. (2005). Calibration of an impedance probe for estimation of surface soil water content over large regions. *Journal of Hydrology*, 311, 49-58.
- Crow, W.T., Kustas, W.P., & Prueger, J.H. (2008). Monitoring root-zone soil moisture through the assimilation of a thermal remote sensing-based soil moisture proxy into a water balance model. *Remote Sensing of Environment*, 112, 1268-1281.
- Crow, W.T., & Co-authors (2005). An observing system simulation experiment for Hydros radiometer-only soil moisture products. *IEEE Transactions on Geoscience and Remote Sensing*, 43, 1289-1303.
- Chauhan, N., Lang, & R.H., Ranson, K.J. (1991). Radar modeling of a boreal forest. *IEEE Transactions on Geoscience and Remote Sensing*, 29, 627-638.
- Chauhan, N.S., Le Vine, D.M., & Lang, R.H. (1994). Discrete scatter model for microwave radar and radiometer to corn: comparison of the theory and data. *IEEE Transactions on Geoscience Remote Sensing*, 32, 416-426.
- Chauhan, N.S. (1997). Soil moisture estimation under a vegetation cover: combined active passive microwave remote sensing approach. *International Journal of Remote Sensing*, 18, 1079-1097.
- Choudhury, B. J.; Schmugge, T. J.; Newton, R. W.; Chang, A. T. C. (1979). Effect of surface roughness on microwave emission of soils. *Journal of Geophysical Research*, 84, 5699-5706.

References

- Choudhury, B.J., Schmugge, T.J., & Mo, T. (1982). A parameterization of effective soil temperature for microwave emission. *Journal of Geophysical Research*, *87*, 1301-1314.
- Davidson, M.W.J., Le Toan, T., Mattia, F., Satalino, G., Manninen, T. & Borgeaud, M. (2000). On the characterization of agricultural soil roughness for radar remote sensing studies. *IEEE Transactions on Geoscience and Remote Sensing*, *38*, 630-639.
- Debye, P. 1929. Polar molecules. Dover, Mineola, New York.
- De Lannoy, G.J.M., Verhoest, N.E.C., Houser, P.R., Gish, T.J., & Van Meirvenne, M., (2006). Spatial and temporal characteristics of soil moisture in an intensively monitored agricultural field (OPE³). *Journal of Hydrology*, *331*, 719-730.
- Della Vecchia, A., Saleh, K., Ferrazzoli, P., Guerriero, L., & Wigneron, J.-P. (2006a). Simulating L-band emission of coniferous forests using a discrete model and a detailed geometrical representation. *IEEE Geoscience and Remote Sensing Letter*, *3*, 364 -368.
- Della Vecchia, A., Ferrazzoli, P., Guerriero, L., Blaes, X., Defourny, P., Dente, L., Mattia, F., Satalino, G., Strozzi, T., Wegmuller, U., 2006, "Influence of geometrical factors on crop backscattering at C-band", *IEEE Transactions on Geoscience and Remote Sensing*, pp. 778-790.
- Della Vecchia, A., Ferrazzoli, P., Guerriero, L., Ninivaggi, L., Strozzi, T., Wegmuller, U., 2008, "Observing and modelling multifrequency scattering of maize during the whole growth cycle", *IEEE Transactions on Geoscience and Remote Sensing*, *46*, pp. 3709-3718.
- Della Vecchia, A., Ferrazzoli, P., Guerriero, L., Rahmoune, R., Paloscia, S., Pettinato, S., Santi, E. (2010). *IEEE Transactions on Geoscience and Remote Sensing*, *48*, 260-272.
- De Rosnay, P., & Co-authors (2006). SMOSREX: A long term field campaign experiment for soil moisture and land surface processes remote sensing. *Remote Sensing of Environment*, *102*, 377-389.
- Dobson, M.C., Ulaby, F.T., Hallikainen, M.T., & El-Rayes, M.A. (1985). Microwave Dielectric Behavior of Wet Soil .2. Dielectric Mixing Models. *IEEE Transactions on Geoscience and Remote Sensing*, *23*, 35-46.
- Drusch, M.; Wood, E.F.; Gao, H.; Thiele, A. (2004). Soil moisture retrieval during the Southern Great Plains Hydrology Experiment 1999: A comparison between experiment remote sensing data and operational products. *Water Resources Research*, *40*, W2504.
- Entekhabi, D., & Co-authors (2004). The hydrosphere state (Hydros) satellite mission: An earth system pathfinder for global mapping of soil moisture and land freeze/thaw. *IEEE Transactions on Geoscience and Remote Sensing*, *42*, 2184-2195.
- Eom, H.J., & Fung, A.K., (1984). A scatter model for vegetation up to Ku-band. *Remote Sensing of Environment*, *15*, 185-200.
- Escorihuela, M.J., Kerr, Y.H., De Rosnay, P., Wigneron, J.P., Calvet, J.C., & Lemaitre, F. (2007). Simple model of the bare soil microwave emission at L-band. *IEEE Transactions on Geoscience and Remote Sensing*, *45*, 1978-1987.
- Escorihuela, M.J., Chanzy, A., Wigneron, J.-P., & Kerr, Y. (2010). Effective soil moisture sampling depth of L-band radiometry: a case study. *Remote Sensing of Environment*, *114*, 995-1001.

- Ferranti, L., & Viterbo, P. (2006). The European summer of 2003: Sensitivity to soil water initial conditions. *Journal of Climate*, *19*, 3659-3680.
- Ferrazzoli, P., & Guerriero, L. (1996). Passive microwave remote sensing of forests: a model investigation. *IEEE Transactions on Geoscience Remote Sensing*, *34*, 433-443.
- Fung, A.K., Li, Z., & Chen, K.S. (1992). Backscattering from a randomly rough dielectric surface. *IEEE Transactions on Geoscience and Remote Sensing*, *30*, 356-369.
- Gish, T.J., Walthall, C.L., Daughtry, C.S.T., Dulaney, W.P., & McCarty, G.W. (2003). Watershed-Scale Sensing of Subsurface Flow Pathways at Ope3 Site. In: Proceedings of the First Interagency Conference on Research in the Watersheds, October 27-30, 2003, Benson.
- Grant, J.P., Wigneron, J.P., Van de Griend, A.A., Kruszewski, A., Sobjaerg, S.S., & Skou, N. (2007). A field experiment on microwave forest radiometry: L-band signal behaviour for varying conditions of surface wetness. *Remote Sensing of Environment*, *109*, 10-19.
- Guglielmetti, M., Schwank, M., Matzler, C., Oberdorster, C., Vanderborght, J., & Fluhler, H. (2007). Measured microwave radiative transfer properties of a deciduous forest canopy. *Remote Sensing of Environment*, *109*, 523-532.
- Hornbuckle, B.K., England, A.W., De Roo, R.D., Fischman, M.A., & Boprie, D.L. (2003). Vegetation canopy anisotropy at 1.4 GHz. *IEEE Transactions on Geoscience and Remote Sensing*, *41*, 2211-2223.
- Hornbuckle, B.K., England, A.W., Anderson, M.C., & Viner, B.J. (2006). The effect of free water in a maize canopy on microwave emission at 1.4 GHz. *Agricultural and Forest Meteorology*, doi:10.1016/j.agrformet.2006.05.003.
- Jackson, T.J., Schmugge, T.J., & Wang, J.R. (1982). Passive microwave sensing of soil moisture under vegetation canopies. *Water Resources Research*, *18*, 1137-1142.
- Jackson, T.J., & O'Neill, P.E. (1990). Attenuation of Soil Microwave Emission by Corn and Soybeans at 1.4 Ghz and 5 Ghz. *IEEE Transactions on Geoscience and Remote Sensing*. *28*, 978-980.
- Jackson, T.J., & Schmugge, T.J. (1991). Vegetation effects on the microwave emission of soils. *IEEE Transactions on Geoscience and Remote Sensing*, *36*, 203-212.
- Jackson, T.J. (1993). Measuring surface soil moisture using passive microwave remote sensing. *Hydrological Processes*, *7*, 139-152.
- Jackson, T.J., Le Vine, D.M., Griffis, A.J., Goodrich, D.C., Schmugge, T.J., Swift, C.T. & O'Neill, P.E. (1993). Soil moisture and rainfall estimation over a semi-arid environment with the ESTAR microwave radiometer. *IEEE Transactions on Geoscience and Remote Sensing*, *31*, 836-841.
- Jackson, T.J., & Co-authors (1999). Soil moisture mapping at regional scales using microwave radiometry: The Southern Great Plains Hydrology Experiment. *IEEE Transactions on Geoscience and Remote Sensing*, *37*, 2138-2151.
- Jackson, T.J.; Chen, D.; Cosh, M.; Li, F.; Anderson, M.; Walthall, C.; Doriaswamy, P.; Hunt, E.R. (2004). Vegetation water content mapping using Landsat data derived normalized difference water index for corn and soybeans. *Remote Sensing of Environment*, *92*, 475-482.

References

- Joseph, A.T., Van der Velde, R., O'Neill, P.E., Lang, R.H., & Gish, T. (2008). Soil moisture retrieval during a corn growth cycle using L-band (1.6 GHz) radar observations. *IEEE Transactions on Geoscience and Remote Sensing*, *46*, 2365-2374.
- Joseph, A.T., Van der Velde, R., O'Neill, P.E., Lang, R.H., & Gish, T. (2010). Effects of a corn canopy on C- and L-band radar backscatter: a correction method for soil moisture retrieval. *Remote Sensing of Environment*, *114*, 2417-2430.
- Joseph, A. T., Van der Velde, R., O'Neill, P.E., Choudhury, B.J., Lang, R.H., Kim, E.J., & Gish, T. (2010b). L Band brightness temperature observations over a corn canopy during the entire growth cycle. *Sensors*, *10*, 6980-7001.
- Karam, M.A., Fung, A.K., Lang, R.H., & Chauhan, N.S. (1992). A microwave scattering model for layered vegetation. *IEEE Transactions on Geoscience Remote Sensing*, *30*, 767-784.
- Karam, M.A. (1997). A physical model for microwave radiometry of vegetation. *IEEE Transactions on Geoscience and Remote Sensing*, *35*, 1045-1058.
- Kerr, Y.H., Waldteufel, P., Wigneron, J.P., Martinuzzi, J.M., Font, J., & Berger, M. (2001). Soil moisture retrieval from space: The Soil Moisture and Ocean Salinity (SMOS) mission. *IEEE Transactions on Geoscience and Remote Sensing*, *39*, 1729-1735.
- Kerr, Y. H.; Waldteufel, P.; Richaume, P.; Davenport, I.; Ferrazzoli, P.; Wigneron, J.P. (2006). SMOS level 2 processor Soil moisture Algorithm theoretical Basis Document (ATBD). SM-ESL (CBSA), CESBIO, Toulouse, SO-TN-ESL-SM-GS-0001, V5.a, 15/03/2006.
- Kirdyashev, K.P., Chukhlantsev, A.A., & Shutko, A.M. (1979). Microwave radiation of ground with vegetative cover. *Radiotekh Elektron+*, *24*, 256-264.
- Kurum, M., Lang, R.H., O'Neill, P.E., Joseph, A.T., Jackson, T.J., & Cosh, M.H. (2009). L-Band Radar Estimation of Forest Attenuation for Active/Passive Soil Moisture Inversion. *IEEE Transactions on Geoscience and Remote Sensing*, *47*, 3026-3040.
- Lang, R.H.; Sidhu, J.S. (1983). Electromagnetic backscattering from a layer of vegetation: a discrete approach. *IEEE Transactions on Geoscience and Remote Sensing*, *21*, 62-71.
- LeVine, D.M., Meneghini, R., Lang, R.H., & Seker, S.S., (1983). Scattering from arbitrarily oriented dielectric disks in the physical optics regime. *Journal of the Optical Society of America*, *73*, 1255-1262.
- Le Vine, D.M., & Karam, M.A. (1996). Dependence of attenuation in a vegetation canopy on frequency and plant water content. *IEEE Transactions on Geoscience and Remote Sensing*, *34*. 1090-1096.
- Mattia, F., Le Toan, T., Picard, G., Posa, F.I., D'Alessio, A., Notarnicola, C., Gatti, A.M., Rinaldi, M., Satalino, G. & Pasquariello, G. (2003). Multitemporal C-band radar measurements on wheat fields. *IEEE Transactions on Geoscience and Remote Sensing*, *41*, 1551-1560.
- Mätzler, C. (1994). Microwave (1-100 GHz) dielectric model of leaves. *IEEE Transactions on Geoscience and Remote Sensing*, *32*, 947-949.
- Miller, J.D.; Gaskin, G.D. (1996). Theta probe ML2x – principle of operation and applications, 2nd ed. Macaulay Land Use Research Institute (MLURI). Crairiebuckler, Aberdeen, AB158 QH.

- Mironov, V.L., Dobson, M.C., Kaupp, V.H., Komarov, S.A., & Kleshchenko, V.N. (2004). Generalized refractive mixing dielectric model for moist soils. *IEEE Transactions on Geoscience and Remote Sensing*, 42, 773-785.
- Mironov, V.L., Kosolapova, L.G., & Fomin, S.V. (2009). Physically and Mineralogically based spectroscopic dielectric model for moist soils. *IEEE Transactions on Geoscience and Remote Sensing*, 47, 2059-2070.
- Mo, T.; Choudhury, B.J.; Schmugge, T.J.; Wang, J.R.; Jackson, T.J. (1982). A model for microwave emission from vegetation-covered fields. *Journal of Geophysical Research*, 87, 11229-11237.
- Mo, T., & Schmugge, T.J. (1987). A Parameterization of the Effect of Surface-Roughness on Microwave Emission. *IEEE Transactions on Geoscience and Remote Sensing*, 25, 481-486.
- Mo, T, Choudhury, B.J., Schmugge, T.J., Wang, J.R., & Jackson, T.J., (1982). A model for microwave emission from vegetation covered field. *Journal of Geophysical Research*, 87, 1229-1237.
- Njoku, E.G. (1999). AMSR land surface parameters: surface soil moisture, land surface temperature, vegetation water content; Algorithm Theoretical Basis Documen. Jet Propulsion Laboratory: California Institute of Technology, Pasadena, CA.
- O'Neill, P.E., Jackson, T.J., Blanchard, B.J., Wang, J.R., & Gould, W.I., (1984). Effects of corn stalk orientation and water content on passive microwave sensing of soil moisture. *Remote Sensing of Environment*, 16, 55-67.
- Owe, M.; De Jeu, R.A.M.; Walker, J.P. (2001). A methodology for surface soil moisture and vegetation optical depth retrieval using the microwave polarization difference index. *IEEE Transactions on Geoscience and Remote Sensing*, 39, 1643-1654.
- Owe, M.; De Jeu, R.A.M.; Holmes, T.R.H. (2008). Multi-Sensor Historical Climatology of Satellite-Derived Global Land Surface Moisture. *Journal of Geophysical Research*, 113, F01002, doi:10.29/2007JF000769.
- Panciera, R., Walker, J.P., & Merlin, O., (2009a). Improved understanding of soil surface roughness parameterization for L-band passive microwave soil moisture retrieval. *IEEE Geoscience Remote Sensing Letters*, 6, 625-629.
- Panciera, R., Walker, J.P., Kalma, J.D., Kim, E.J., Saleh, K., & Wigneron, J.P. (2009b). Evaluation of the SMOS L-MEB passive microwave soil moisture retrieval algorithm. *Remote Sensing of Environment*, 113, 435-444.
- Parde, M., Wigneron, J.P., Chanzy, A., Waldteufel, P., Kerr, Y., & Huet, S. (2003). Retrieving surface soil moisture over a wheat field: Comparison of different methods. *Remote Sensing of Environment*, 87, 334-344.
- Parde, M., Wigneron, J.P., Waldteufel, P., Kerr, Y.H., Chanzy, A., Sobjaerg, S.S., & Skou, N. (2004). N-parameter retrievals from L-band microwave observations acquired over a variety of crop fields. *IEEE Transactions on Geoscience and Remote Sensing*, 42, 1168-1178.
- Rees, W.G., 2001, *Physical Principle of Remote Sensing: Second Edition*, Cambridge University Press, Cambridge, United Kingdom, pp.335.
- Ryu, D., & Famiglietti, J.S. (2005). Characterization of footprint-scale surface soil moisture variability using Gaussian and beta distribution functions during the Southern Great Plains 1997 (SGP97) hydrology experiment. *Water Resources Research*, 41, W12433.

References

- Saatchi, S.S., Le Vine, D.M., Lang, R.H., (1994), Microwave backscattering and emission model for grass canopies. *IEEE Transactions on Geoscience and Remote Sensing*, 32, 177-186.
- Saleh, K., Wigneron, J.P., De Rosnay, P., Calvet, J.C., Escorihuela, M.J., Kerr, Y., & Waldteufel, P. (2006). Impact of rain interception by vegetation and mulch on the L-band emission of natural grass. *Remote Sensing of Environment*, 101, 127-139.
- Saleh, K., Wigneron, J.P., Waldteufel, P., De Rosnay, P., Schwank, M., Calvet, J.C., & Kerr, Y.H. (2007). Estimates of surface soil moisture under grass covers using L-band radiometry. *Remote Sensing of Environment*, 109, 42-53.
- Saleh, K.; Kerr, Y.H.; Richaume, P.; Escorihuela, M.J.; Panciera, R.; Delwart, S.; Boulet, G.; Maisongrande, P.; Walker, J.P.; Wursteisen, P.; Wigneron, J.P. (2009). Soil moisture retrievals at L-band using a two-step inversion approach. *Remote Sensing of Environment*, 113, 1304-1312.
- Seker, S.S., & Schneider, A. (1988). Electromagnetic scattering from a dielectric cylinder of finite length. *IEEE Antennas and Propagation*, 36, 303-307.
- Schmugge, T.J.; Jackson, T.J. (1992). A dielectric model of the vegetation effects on the microwave emission from soils. *IEEE Transactions on Geoscience and Remote Sensing*, 30, 757-760.
- Ulaby, F.T. & El-Rayes, M.A. (1987). Microwave Dielectric Spectrum of Vegetation Part II: Dual-Dispersion Model. *IEEE Transactions on Geoscience and Remote Sensing*, GE-25, 550-557.
- Ulaby, F.T., Sarabandi, K., McDonald, K., Whitt, M., & Dobson, M.C. (1990). Michigan microwave canopy scattering model. *International Journal of Remote Sensing*, 11, 1223-1253.
- Ulaby, F.T., Moore, R.K., & Fung, A.K. (1992). Microwave remote sensing: active and passive. Vol. III From theory to application. Norwood, MA: Artech House.
- Vall-Ilossera, M., & Co-authors (2005). SMOS REFLEX 2003: L-band emissivity characterization of vineyards. *IEEE Transactions on Geoscience and Remote Sensing*, 43, 973-982.
- Van de Griend, A.A., & Wigneron, J.P. (2004a). The b-factor as a function of frequency and canopy type at H-polarization. *IEEE Transactions on Geoscience and Remote Sensing*, 42, 786-794.
- Van de Griend, A.A., & Wigneron, J.P. (2004b). On the measurement of microwave vegetation properties: Some guidelines for a protocol. *IEEE Transactions on Geoscience and Remote Sensing*, 42, 2277-2289.
- Van der Velde, R., Su, Z., & Ma, Y.M. (2008). Impact of soil moisture dynamics on ASAR sigma degree signatures and its spatial variability observed over the Tibetan plateau. *Sensors*, 8, 5479-5491.
- Vinnikov, K.Y., Robock, A., Speranskaya, N.A., & Schlosser, C.A. (1996). Scales of temporal and spatial variability of midlatitude soil moisture. *Journal of Geophysical Research*, 101, 7163-7174.
- Wang, J.R., & Choudhury, B.J. (1981). Remote sensing of soil moisture content over bare field at 1.4 GHz frequency. *Journal of Geophysical Research*, 86, 5277-5282.
- Wang, J.R., O'Neill, P.E., Jackson, T.J., & Engman, E.T. (1983). Multi-frequency measurements of the effects of soil moisture, soil texture, and surface roughness. *IEEE Transactions on Geoscience and Remote Sensing*, 21, 44-51.

- Wang, J.R., Shiue, J.C., Schmugge, T.J., & Engman, E.T. (1990). The L-band PBMR measurements of surface soil moisture in FIFE. *IEEE Transactions on Geoscience and Remote Sensing*, 28, 906-914.
- Wegmuller, U., & Matzler, C. (1999). Rough bare soil reflectivity model. *IEEE Transactions on Geoscience and Remote Sensing*, 37, 1391-1395.
- Wen, J., Su, Z., & Ma, Y.M. (2003). Determination of land surface temperature and soil moisture from Tropical Rainfall Measuring Mission/Microwave Imager remote sensing data. *Journal of Geophysical Research*, 108, DOI: 10.1029/2002JD002176.
- Wigneron, J.P., Laguerre, L., & Kerr, Y.H. (2001). A simple parameterization of the L-band microwave emission from rough agricultural soils. *IEEE Transactions on Geoscience and Remote Sensing*, 39, 1697-1707.
- Wigneron, J.P., Chanzy, A., Calvet, J.C., & Bruguier, W. (1995). A simple algorithm to retrieve soil moisture and vegetation biomass using passive microwave measurements over crop fields. *Remote Sensing of Environment*, 51, 331-341.
- Wigneron, J.P., Calvet, J.C., Pellarin, T., Van de Griend, A.A., Berger, M., & Ferrazzoli, P. (2003). Retrieving near-surface soil moisture from microwave radiometric observations: current status and future plans. *Remote Sensing of Environment*, 85, 489-506.
- Wigneron, J.-P.; Calvet, J.-C.; De Rosnay, P.; Kerr, Y.; Waldteufel, P.; Saleh, K.; Escorihuela, M.J.; Kruszewski, A. Soil moisture retrievals from biangular L-band passive microwave observations. *IEEE Geoscience and Remote Sensing Letters* 2004, 1, 277-281.
- Wigneron, J.P., Parde, M., Waldteufel, Chanzy, A., Kerr, Y., Schmidl, S., & Skou, N. (2004). Characterizing the dependence of vegetation model parameters on crop structure, incidence angle, and polarization at L-band. *IEEE Transactions on Geoscience and Remote Sensing*, 42, 416-425.
- Wigneron, J.P., & Co-authors (2007). L-band Microwave Emission of the Biosphere (L-MEB) model: Description and calibration against experimental data sets over crop fields. *Remote Sensing of Environment*, 107, 639-655.